Surface investigations of steels treated under hydrogen salt cavern boundary conditions

By

Luisa Friederike Ehmcke

Student number: 5267250

in partial fulfilment of the requirements for the degree of

Master of Science

in Materials Science and Engineering

at the Delft University of Technology,
to be defended publicly on Monday September 26, 2022 at 13:30 AM.

<table>
<tr><td>Supervisor:</td><td>Dr. A. Böttger (TU Delft)</td></tr>
<tr><td></td><td>Dr.-Ing. M. Kröner (DLR)</td></tr>
<tr><td></td><td>H. Janßen (DLR)</td></tr>
<tr><td>Thesis committee:</td><td>Dr. A. Böttger</td></tr>
<tr><td></td><td>Dr. V. Popovich</td></tr>
<tr><td></td><td>Prof. J. Sietsma</td></tr>
<tr><td></td><td>Prof. J. Padding</td></tr>
<tr><td></td><td>H. Janßen (DLR)</td></tr>
</table>

TUDelft

DLR **Deutsches Zentrum**
für Luft- und Raumfahrt
German Aerospace Center

Abstract

Large-scale hydrogen storage is a crucial part of the energy transition. The usage of salt caverns has a great potential in this process, but there are open questions regarding the construction's lifetime which need to be investigated prior to their implementation. In this work, potential construction steels were studied. The conditions in a salt cavern were imitated on laboratory scale with an experimental high-pressure setup. Two steels, J55 and H_2-ready X56, were systematically exposed to pressure/temperature cycles, gas (H_2 and N_2), water and brine. Scanning electron microscopy (SEM) and energy dispersive X-ray spectroscopy (EDX) techniques were used for the characterisation of the steels' surface, focussing on corrosion effects and crack formation. For both steels, a significant impact of moisture and salt ions could be shown. However, only for J55, intensification of corrosion and cracking on the surface due to hydrogen gas exposure was found. Pronounced crack formation over the entire surface of J55 was revealed. For X56 significantly less crack formation could be observed. Overall, the results strongly indicate better resistance of X56 than J55 against the conditions in a salt cavern, used for hydrogen storage.

Acknowledgement

Contents

List of abbreviations

AIDE .... *adsorption-induced dislocation emission*
Ar .... *argon*
CF.. *corrosion fatigue*
CH_4 .... *methane*
CO .... *carbon monoxide*
CO_2 .... *carbon dioxide*
EDX .... *energy dispersive X-ray spectroscopy*
EIC .... *environmentally-induced cracking*
EOS .... *equation of state*
Fe_2O_3 .... *hematite*
FeO .... *wüstite*
H_2 .... *hydrogen*
H_2S .... *hydrogen sulphide*
HCHO .... *formaldehyde*
HCOOH .... *formic acid*
He .... *helium*
HE .... *hydrogen embrittlement*
HEDE .... *hydrogen-enhanced decohesion*
HELP.. *hydrogen-enhanced localised plasticity*
HESIV .... *hydrogen-enhanced strain-induced vacancies*
HIC .... *hydrogen-induced cracking*
HV .... *Huron-Vidal*
LCA .... *life cycle assessment*
MIT .... *mechanical integrity test*
M-TT .... *micro tensile test*
N_2 .... *nitrogen*
NaCl .... *sodium chloride*
ND .... *normal direction*
NH_3 .... *ammonia*
O_2 .... *oxygen*
ppm... *parts per million*
PV.. *photovoltaic*
RD .... *rolling direction*
SCC .... *stress corrosion cracking*
SEM .... *scanning electron microscopy*
SIMS ....*secondary ion mass spectrometry*
SOHIC... *stress-oriented hydrogen-induced cracking*
SPT .... *small punch test*
SSC... *sulphide stress cracking*
TDS .... *thermal desorption spectroscopy*
UGS.. *underground gas storage*
UHS.. *underground hydrogen storage*
XRD .... *X-ray diffraction*
ZRP .... *zinc-rich paint*

1. Introduction

In the current times, the energy transition towards renewable energy sources is more urgently required than ever before. Once, to counteract the climate change including rising temperatures and raising sea levels but also to become more independent of other states in crisis situations, like the Ukraine war from 2022. Typical renewable energy sources are photovoltaic (PV) and wind energy. The output in both technologies has a randomness and intermittence, leading to fluctuations on short-time and inter-seasonal scales [1]. Therefore, development of short-term energy storage is necessary to smoothen the output, meaning stabilization of frequency, voltage and power quality of the system. Development of long-term energy storage is important to ensure access to reliable energy services throughout the entire year.

The focus of this work lies on technology for long-term energy storage. A suitable way to store large quantities of energy for a long period of time is chemical storage, therefore often natural gas is used. But in the future, hydrogen (H_2) could replace natural gas is many applications. Multiple promising research fields related to hydrogen exist, like various fuel cell vehicles and green ammonia production [2]. Also, the steel industry offers great potentials for hydrogen usage [3]. As the iron and steel industry cause 4 % of anthropogenic carbon dioxide (CO_2) emission in Europe, decarbonisation of the sector can contribute strongly to the reduction of the greenhouse gases [3]. Since hydrogen can be produced CO_2 neutral, it supports the idea behind the energy transition. However, for a future in which hydrogen plays a key role as secondary energy carrier, the infrastructure for its storage needs to be built. The storage under the ground in large salt caverns has a great potential in this section. Lots of experience with gas storage in salt caverns was gained due to their usage for natural gas, nonetheless there are many open questions, which need to be answered [4]. Particularly questions regarding the lifecycle are of interest. For the salt cavern construction, a variety of materials are required, including concrete, polymers and steel. This work focuses on the steel, which is required in large amounts for the underground piping of salt caverns. Though a suitable steel type is in use for natural gas storage, its suitability needs to be confirmed for hydrogen storage. Other potential steels should also be tested, as the most suitable and ecological steel should be implemented. This work focuses on investigating the suitability of two steels, J55 and X56, by answering the following research questions:

1) Do temperature and pressure cycles impact J55 and H2-ready X56 steel microscopically visible?
2) How is the impact of the permanent brine in a salt cavern on J55 and H2-ready X56?
3) Is hydrogen embrittlement and/or corrosion microscopically visible under the tested conditions?
4) Can trends be observed for different conditions of the salt cavern?
5) Do the results suggest suitability of J55 and/or X56 for salt cavern construction?

For this purpose, surface investigations of J55 and X56 steels, which were treated under varying hydrogen salt cavern conditions, were conducted. The goal of the work was to study the visible impact on the surface, allocate the effects to the conditions and to find trends in the corrosion of the specimen as well as the cracking depending on the exposure conditions. For this, microscopic techniques combined with compositional surface analysis were conducted to visualise crack formation and to study corrosion aspects, respectively. As an understanding of the results depends on the background, in chapter 2 the theory on salt caverns, material stability and cracking methods is provided. Chapter 3 describes the experimental procedure, followed by the presentation of results and their discussion in Chapter 4. A discussion on general aspects is conducted in chapter 5. Chapter 6 concludes the work and chapter 7 provides recommendation on future research, based on the results.

2. Background

For an understanding of the practical work, the background from literature on salt caverns, hydrogen embrittlement, cracking mechanism and the steels has to be enlightened.

2.1 Underground gas storage

Salt caverns belong to the group of underground gas storage (UGS) methods. Hence, a short introduction to the UGS in general is provided. UGS is the storage of gases and oils in geological reservoirs such as depleted gas reservoirs, aquifers or salt caverns. They are an economical option for the inter-seasonal storage of large quantities of chemical energy, such as natural gas, and potentially the most economical option for hydrogen [5]. Currently, there are 689 UGS-facilities around the world with the capacity to store 11 % of the total global gas consumption, mostly used for natural gas [6]. At present, natural gas storage plays a major role in the management of the gas supply chain, which characteristically includes large hourly, daily and annual imbalances between supply and demand [7]. These originate from the daily routine of the customers as well as seasonal differences in customers' needs. To balance these mismatches, the UGS are used as represented in Figure 1.
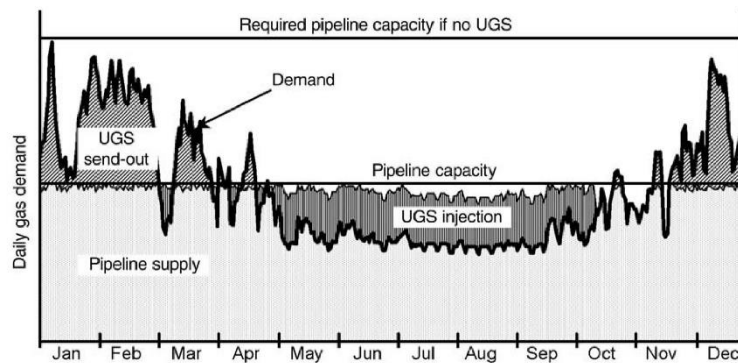
Figure 1: Illustration of UGS usage to manage the gas supply chain, taken from [7].

In the figure are two horizontal lines shown, one representing the pipeline capacity with the use of UGS, and one without. Without the storage systems, more gas would be required constantly, which is neither environmentally friendly nor economical. There are in general different storage purposes which cover multiple time scales. The storages to balance the hourly and seasonal fluctuations are called 'daily storage' and 'seasonal storage', respectively. Additionally, governments use UGS as 'strategic storage' to prevent supply interruptions due to technical issues or political, diplomatic and military events. In general, the storage ensures the energy security in case of supply interruptions of various reasons [6]. Since supply interruptions also impact the gas price, energy companies are interested in the investment of storage sites to make profit out of shortcomings. However, energy security is not only one of the main driving forces for natural gas storage, but also for hydrogen storage, and with the energy transition towards power generation by renewable energies, energy storage further gains in importance. Additional to fluctuations in energy consumption, an increase in daily and seasonal fluctuations of the energy production will arise [8]. These are caused by the randomness and intermittence of PV and wind energy output [1]. Although there are many options for energy storage, which can be (electro-)chemical, mechanical, electromagnetic or thermal, most of the options have limitations in their scalability [9]. An overview of the storage techniques can be found in literature[9, 10]. For large-scale energy storage chemical energy storage is often used. Chemical energy can be stored as natural gas as well as hydrogen, however the production of hydrogen through electrolysis can be conducted environmentally friendly. Since large quantities have to be stored to ensure energy security, geological reservoirs are the most feasible method [8]. They are the most promising option to store sufficient quantities, while claiming relatively small surface areas. Additionally, they guarantee a high safety level due to the absence of contact with oxygen. It has to be noted, that many other hydrogen storage options exist, which are more applicable in smaller scales. An overview can be found in literature [11-13]. Within the storage

in geological reservoirs different options are available, those are characterised by working volume, cushion gas, deliverability, injectability and duration [7]. In general, the working volume or working gas is the maximum volume of gas withdrawn and injected in each cycle. However, after the withdrawal, there is still gas left in the facility, which is called cushion gas or base gas. It is required to keep the minimum pressure for the necessary deliverability. For salt cavern specifically, the minimum pressure is important to sustain the mechanical stability. The cavern wall has convergence, meaning salt creep caused by pressures, which has to be kept to acceptable levels. There is also a maximum pressure, which for salt caverns is limited by the lithostatic pressure over which salt would start to fracture. The inventory is the total gas, working gas and cushion gas together. The rate at which gas can be withdrawn from the storage site, and therefore delivered, is called deliverability. Although it is mostly constant during withdrawal of gas, it may decrease when most of the working gas is already withdrawn due to the pressure drop inside the cavern. The complementary property is the injectability, which describes the rate at which gas can be injected inside the space. Lastly, the duration describes the time required to produce the working volume and is therefore the relationship between working volume and deliverability.

There are two general principles of UGS: 1. storage in porous space of sedimentary rocks in which porous and permeable reservoir rock provides the actual storage volume [14]. 2. storage in manmade cavities, which is sub-categorised in salt cavern, mined rock cavern and conventional abandoned mines [14]. But, mined rock caverns and abandoned mines are likely to play a minor role in hydrogen storage. The focus of this work are salt caverns, which are artificially built in thick salt deposits. In Europe bedded salt deposits are as deep as 2000 m for Permian salt deposits and up to 1000 m for Triassic and tertiary salt deposits [14]. They consist of rock salt, mainly sodium chloride ($NaCl$), but the exact composition varies greatly due to contaminations. The mineral halite ($NaCl$) is generally suitable for storage of natural gas, CO2 and hydrogen. The difference in the gas properties, originating particularly from the molecular size, lead to particularly strict requirements for hydrogen storage [4]. Hydrogen can easily diffuse inside materials leading to leakages. Yet, the salt offer gas tightness and inertness for hydrogen; hence the caverns are of special interest for storage [14].

Since different gases and gas mixtures are stored underground, there is a competition for storage sites among them. In this work, only hydrogen storage will be considered. The choice of the underground storage type depends on the goal and the entire energy cycle. While using the stored hydrogen as town gas or for mixture with natural gas imply less requirements for the storage site, the usage in fuel cells require the hydrogen to be pure, therefore gas reactions within the site should be prohibited [8]. For ultra-pure hydrogen, salt caverns are the most promising option since they are almost perfectly hermetic and are characterised by a high-degree of cleanliness and a low risk of probable gas contamination by impurities. However, the presence of the permanent brine might lead to contamination. Since aspects of hydrogen storage in salt caverns are the focus of this work, those will be explained in more detail in the next subsection. The other UGS/underground hydrogen storage (UHS) options won't be elaborated upon.

2.2 Salt caverns

To provide insight in the salt cavern characteristics, in this subsection different aspects of hydrogen storage in salt caverns, such as the construction, the conditions and impurities, will be elaborated upon. Especially the conditions and impurities within the cavern are of interest, since these need to be considered in the steel analysis tests within this thesis.

Salt caverns are manmade cavities in the subsurface within thick salt deposits [14]. Those salt deposits can be in form of salt domes or bedded salt, in both cases sufficient thickness and a favourable depth need to be given which limits the potential sites [15]. The potential in Europe constitutes 84.8 PWh considering onshore and offshore sites [4]. 42 % of this potential belongs to Germany. In Figure 2 the total cavern potential for European countries is illustrated. Taking Germany as an example, it can be seen, that the storage potential exceeds the final electricity consumption of 535.64 TWh for 2020 [16], which demonstrates the dimensions of the salt cavern potential. Furthermore, Crotogino *et al.* stated the hydrogen demand in Germany by 2050 to be 131.4 TWh per year [17], the potential greatly exceeds these values. To harness this potential for UHS, salt caverns have to be artificially built.
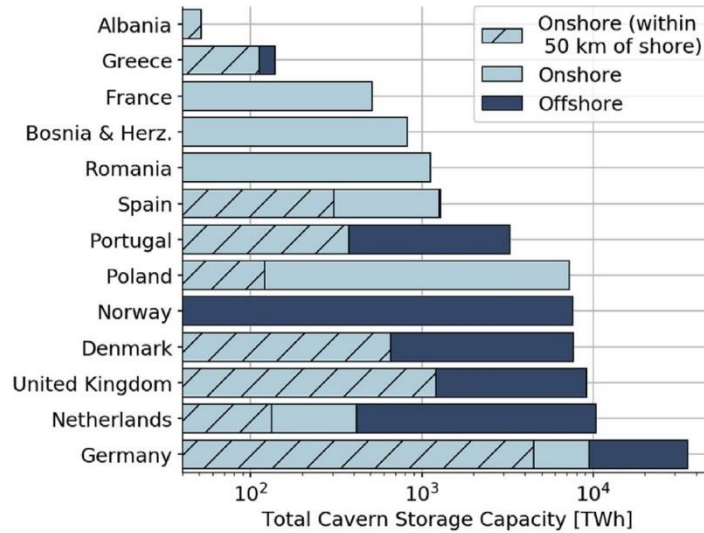
Figure 2: Total cavern potential for European countries, considering onshore, onshore within 50 km of shore and offshore sites. Figure is taken from [15].

2.2.1 Construction

Due to strict requirements for a suitable UHS site, they are geographically limited to a few locations [5]. To determine the potential of a site, extensive exploration surveys are necessary [14]. Geological characterisation methods are used to detect impurities, anomalous zones and geological structures [7]. Details about potential site's surveys can be found elsewhere [14]. The construction process makes use of solution mining technology, which can create a cavern by injection of water and extraction of water/brine through a well [5, 18]. First, the borehole is created by drilling to the demanded depth into a suitable salt formation [5]. Running and cementing of casing is conducted and two annular pipes called 'leaching strings' are placed inside the borehole and lowered to the centre of the cavity [7]. To prevent leaching around and above the casing, diesel or nitrogen is filled between the outer leaching string and the casing itself, building a gas blanket. While the standard procedure uses diesel or nitrogen gas for the gas blanket, diesel or nitrogen residues possibly cause contamination in the hydrogen gas during later operation. Hence for storage of pure hydrogen a new standard procedure potentially needs to be implemented. The outer leaching string is used for the injection of fresh water, the water dissolves salt and saturated brine is removed through the inner leaching string leaving salt free space behind [14]. Simultaneously to the extraction, injection of fresh water takes place until the desired size is reached. Since approximately 7.5 m^3 of fresh water is needed to dissolve 1 m^3 of salt, a nearby water supply is required to cover the demand [5]. Also, suitable disposal options for the brine needs to be available. During the process, shape control is conducted by monitoring the progress with sonar and adjusting the placement of the leaching strings. The leaching is a time-consuming step of the construction process and can take months to years [7].

Once the solution mining process is completed, the cavern has to be prepared for gas storage. First, an initial mechanical integrity test (MIT) is performed to proof gas tightness of the uppermost salt and the well completion. During the MIT, not the entire cavern is filled with hydrogen but only the top space with the inner casing tube, as leakage problems occur mostly in this part, the rest is filled with liquid used for the excavation [14]. When the MIT confirms gas tightness the debrining process can be conducted, using gas pressure to displace the brine [5]. It is important to note, that not all brine can be removed during the debrining process, because of insoluble solids which are too big to be removed by the excavation process [14]. The permanent brine may occupy up to 30 % of the total cavern volume. Hence in the initial period of operation there will be salt saturation in the gas withdrawn from the cavity and there might be a permanent impact on the gas quality during operation. The permanent brine needs to be considered during materials selection for the construction.

2.2.2 Operating conditions

An important aspect for the implementation of UHS in salt caverns are the operation conditions, since these will impact the material studies for the construction design. The operation conditions highly depend on the construction details at a specific site. Although salt caverns have good permeability conditions for hydrogen storage, the permeability can be affected by stresses and pressure conditions, which is why it needs to be carefully designed with regard to the specific salt properties and the desired operating conditions [15]. Important design parameters in view of safety and stability are the depth, in-situ stresses, cavern geometry, pressure level limitations and mechanical properties of the salt as well as the surrounding rock.

Underground structure materials are already exposed to initial stresses before the finalisation of the construction process and operation. Those can be estimated depending on the site specifics, for a flat ground surface the vertical initial stress P_v can be estimated in MPa by Eq. 2.1 [15], with H being the depth in m. In thick salt structures the horizontal stress equals the vertical stress.

$$P_v[\text{MPa}]=0.022\frac{\text{MPa}}{\text{m}}\times H[\text{m}] \qquad (2.1)$$

The corresponding effective temperature T in °C can be approximated by Eq. 2.2 [15].

$$T[°C]=12\ °C+\frac{0.03\ °C}{\text{m}}\times H[\text{m}] \qquad (2.2)$$

It has to be noted, that the equations are only for estimation, but not for exact calculation. Additionally, due to the height of the cavern, there will always be a gradient in temperature and pressure between the top and the bottom of the cavern. Nevertheless, the vertical initial pressure on the rock salt can be used for an estimation of the maximum operating pressure, which is approximately 0.75 - 0.85 P_v [15]. The maximum operating pressure is important, since exceeding it may lead to hydraulic fracturing of salt and/or well casing [15]. The minimum pressure is important to ensure mechanical stability, but is harder to estimate. Conservative approximations state it to 0.3 P_v [15] and its limitation is caused by the salt properties and it's potential for dilatancy which appears by too large differences between the pressure inside the cavern and the stress on the surrounding salt. Dilatancy is caused by microcracks, increasing the materials volume, it's permeability as well as accelerating creep and damage behaviour. The minimum pressure is ensured by the cushion gas, which accounts for 30 % of the total storage capacity. Regarding the temperature it has to be considered that there are temperature gradients within the cavern as well as temperature deviations due to gas injection and withdrawal, shown in Figure 3 [19] in which on the left side the cavern shape is shown. The detailed thermodynamic aspects of cavern storage can be found elsewhere [19].

The described estimations in this section can be used to outline the conditions for a realistic cavern in Europe. For a cavern in 1000 m to 1100 m depth, the vertical initial stress starts around 220 bar (22 MPa), which lead to 176 bar maximum pressure and 66 bar minimum pressure. With the cavern height of 100 m there is a pressure gradient to 193.6 bar and 72.6 bar maximum and minimum pressure, respectively. The estimated temperature is around 42 °C to 45 °C. While the pressure cycles have to stay in the range between maximum and minimum value during gas injection and withdrawal, the temperature range also depends on the deliverability/injectability. The approximations provide a frame for the pressure values, in which the experiments will be conducted.
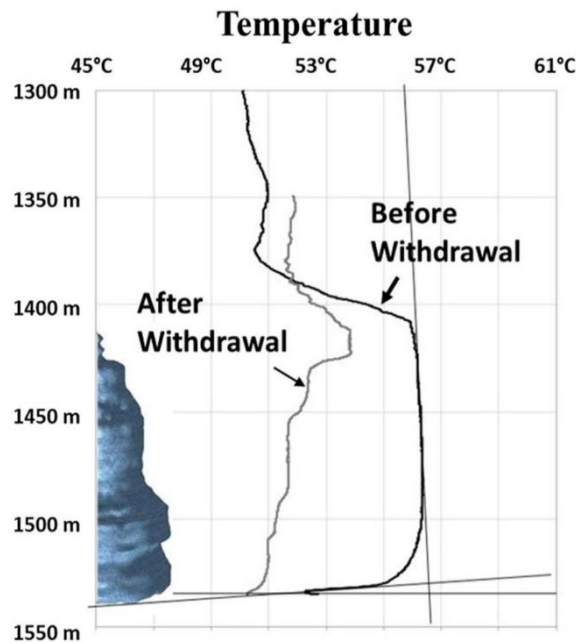
Figure 3: Temperature deviations along an axis of symmetry in an example cavern. On the left side, the cavern shape is shown in blue. Black line: after gas injection; Grey line: after gas withdrawal. The graph was taken from [19].

Besides pressure and temperature, humidity is an important cavern condition which needs to be discussed. First, because it may have an impact on the materials but also because hydrogen gas is supposed to be used for fuel cells which require a high purity [20]. Therefore, it is important to know the concentration of water vapour in the hydrogen gas. The origin of the water vapour lies in the permanent brine inside the cavern. Despite the importance, measurement data are rare. Therefore, two studies modelling the thermodynamics of the hydrogen-water system will be presented as a reference value. Ratnakar *et al.* used a traditional Peng and Robinson (PR) equation of state (EOS) combined with a non-classical Huron-Vidal (HV) mixing rule [21]. The modelled data was compared with experimental data for 50 °C on solubility of hydrogen in water by Wiebe *et al.* [22] and on solubility of water in hydrogen by Maslennikova *et al.* [23]. The results are presented in Figure 4, with mole fractions on the y-axis. While the solubility of hydrogen in water is an indicator for energy losses of the storage method, the solubility of water in hydrogen is important for material studies and the gas quality. It can be seen, that the model has a good correlation with the available measurement data. For 150 bar, a mole fraction of approximately 0.0011 can be read from the graph which equals 1100 ppm. Rahbari *et al.* used force-field-based molecular simulation, more specifically TIP3P-Marx-force fields [24]. For different temperature ranges, different ensembles were used. The contamination value was estimated to 1000 ppm, which is in the same magnitude as the value from the other simulation. Therefore, the approximation of 1000 ppm water vapour in hydrogen gas is a valid assumption for a saturated state. Both simulations were conducted for pure water, to be used for mobility applications and not for salt caverns. In salt caverns there is not pure water present but brine, therefore the solubility is reduced due to ionic forces [25]. The saturating vapour pressure can be estimated as 75 % of the pure water value. It has been suggested, that artificial modifications in the brine composition could further reduce the water vapour pressure. Nevertheless, in a quiescent cavern, the corresponding saturation is reached at some point due to equilibrium conditions. Yet, due to thermodynamic aspects the upper zone of the cavern is separated from the brine by the lower zone and no direct reactions take place [19]. While in the upper zone convection leads to a homogenised composition, in the lower zone there is no convection. Therefore, the water vapour can reach the upper zone by diffusion only, which is a much slower process. Hence, the time frame of injection and withdrawal further impact the concentration.
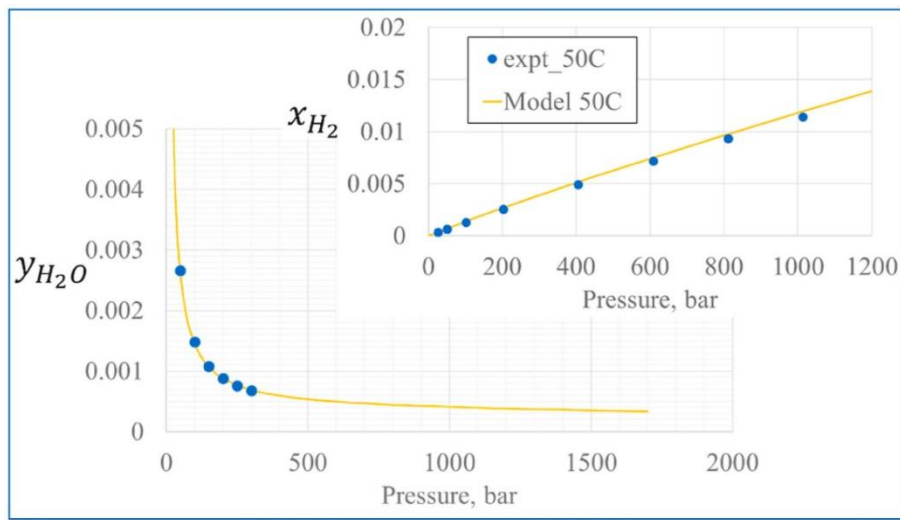
Figure 4: Solubility model for the hydrogen-water system in mole fractions with experimental data for the solubility of hydrogen in water by Wiebe et al. [22] and solubility of water in hydrogen by Maslennikova et al. [23]. The graph is taken from [21] and the sources for the experimental data extracted from the paper.

2.2.3 Impurities

Hydrogen has a high bonding strength, making it chemically inert in the conditions of underground storage [8]. Nevertheless, the purity of the hydrogen can be affected during storage. One impurity was already mentioned above, water from the brine evaporates until thermodynamic equilibrium of the H_2-H_2O system is reached. For the usage of the stored hydrogen in fuel cells the water vapour needs to be removed, since it potentially exceeds the allowed value of 5 ppm by the ISO 14687:2019-11 standard [20].

Another important aspect regarding the brine are the salt ions. In brine a variety of ions like chloride-, sodium-, magnesium-, calcium-, potassium- and sulphur-ion can be found [26]. Since each of the ions might affect the steels' corrosion, the complexity of the impact of the brine is high [27]. A particularly aggressive one is the chloride ion, having the ability to penetrate through the passive film of metals, hence reducing the passivity of steels and increase the probability of localised corrosion [28]. Also, it enables a catalysis reaction resulting in faster iron dissolution. Hence, its presence in the brine might impact the construction steels and its impact should be investigated for the potential steels. In this work, the impact of the individual ions is not investigated, hence the background will not be considered. Nevertheless, it should be noted, that some ions could increase corrosion of steel, while others are beneficial. In this work the overall effect of only one brine composition will be studied.

Since any available water is used for the solution mining, besides water and salt ions more impurities might be introduced into the salt cavern during the construction. As these impurities highly depend on the used water, there is a high level on complexity and the system cannot be generalised in this aspect. These types of impurities will not be studied in this work.

Additionally, impurities can be caused by biochemical transformations involving microorganisms [8]. The microorganisms consume the energy of the triggered reaction while the reaction transforms some of the gas. There are four types of microorganism causing hydrogenotrophic biotic reactions [8], an overview scheme is depicted in Figure 5. Yet two type of microorganism require carbon oxides for the reactions, as carbon oxides are not supposed to be present, the microorganism will be neglected in this work. The first relevant one is the sulphate-reducing bacteria, which causes hydrogen to react with sulphate producing hydrogen sulphide (H_2S) and water [8].

$$5H_2 + SO_4^{2-} \rightarrow H_2S + 4H_2O \tag{2.3}$$
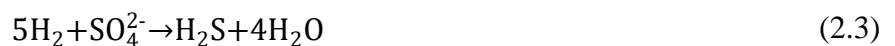
The second, iron-reducing bacteria reduce hematite (Fe_2O_3) with hydrogen to wüstite (FeO) and water [8].

$$H_2 + Fe_2O_3 \rightarrow 2FeO + H_2O \qquad (2.4)$$

It has to be noted, that the influence of high hydrogen concentration on these processes are not sufficiently understood yet [14]. Which reactions take place depend on the specific storage site, the presence of the microorganisms and the reaction educts. Consequently, they need to be considered for purification steps of the hydrogen as well as material choices for the construction. Especially, for the materials' selection it needs to be considered in view of corrosion aspects. Depending on the application of the hydrogen, there are limitation values for the allowed amount of impurities, for fuel cells, they are listed in Table 1.

Table 1: Limitation concentration for impurities in the hydrogen gas for application within PEM-fuel cells. Reproduced from [20].

Component	Property
Hydrogen fuel index	99.97 %
Total non-hydrogen gases	300 ppm
Maximal concentration of individual impurities	
Water (H_2O)	5 ppm
Total hydrocarbons (except methane)	2 ppm
Methane (CH_4)	100 ppm
Oxygen (O_2)	5 ppm
Helium (He)	300 ppm
Nitrogen (N_2)	300 ppm
Argon (Ar)	300 ppm
Carbon dioxide (CO_2)	2 ppm
Carbon monoxide (CO)	0.2 ppm
Total sulphur components (H_2S-basis)	0.004 ppm
Formaldehyde (HCHO)	0.2 ppm
Formic acid (HCOOH)	0.2 ppm
Ammonia (NH_3)	0.1 ppm
Halogenated compounds	0.05 ppm
Maximum particulate concentration	1 mg/kg
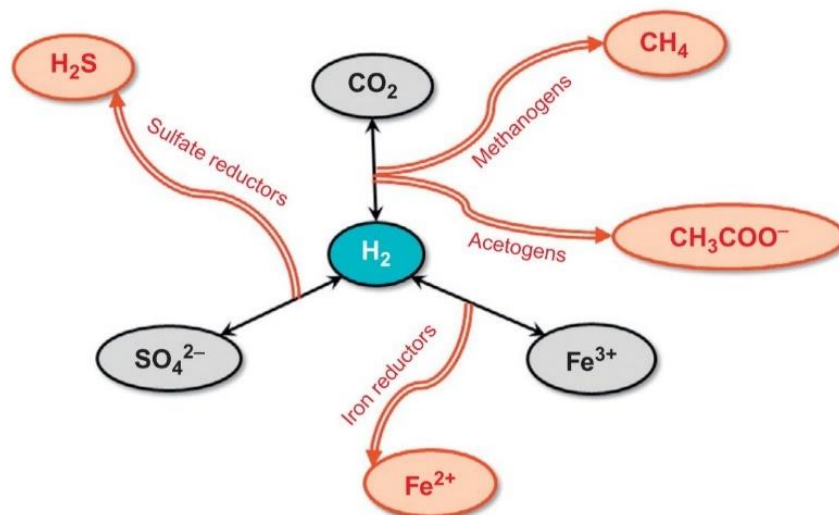
Figure 5: Four types of microorganisms causing hydrogenotrophic biotic reactions in UHS. Taken from [8].

2.2.4 Challenges

While UGS of natural gas provides some experiences, especially the differences of properties between natural gas and hydrogen lead to challenges [4]. The size and the mobility of hydrogen might lead to leakages and safety problems. As smallest molecule, it has a high penetrability and can diffuse inside solids [18]. These properties may reduce the lifetime of the construction materials significantly, especially due to the high concentration of hydrogen and high pressures. While the general impact of hydrogen gas on steel alloys is known (hydrogen blistering, hydrogen-induced cracking and hydrogen embrittlement [29]), the impact on the construction steel in combination with the general salt cavern conditions still require extensive testing. Not only the effect of hydrogen but also corrosion aspects and the combination should be tested for the specific steels and the storage conditions. In the following subsection the basics of hydrogen embrittlement will be presented. Afterwards, two steel categories (Casing and tubing steels; and pipeline steels) will be introduced and the state-of-the-art knowledge of hydrogen and hydrogen sulphide impact onto these presented. Lastly, potentially relevant crack formation mechanism will be introduced.

2.3 Stability of materials under hydrogen exposure

The stability of the construction materials under salt cavern storage conditions, especially the hydrogen exposure but also temperature, pressure, moisture, salts and impurities, is one of the main challenges for the implementation of salt cavern hydrogen storage in the energy supply chain. In this section, general hydrogen embrittlement (HE) will be introduced based on typical features and the most common theories. Afterwards, pipeline steels and casing-and-tubing steels will be presented and the known impact of hydrogen and hydrogen sulphide onto those described.

2.3.1 Hydrogen Embrittlement

Hydrogen exposure is a risk factor for metallic construction materials as it can cause embrittlement and cracking [29]. Mostly the term 'hydrogen embrittlement' is used for general hydrogen-induced material damage. However, it only describes one possible feature, the brittle fracture, but other hydrogen-induced features can occur. Hydrogen can be introduced into the material during the production phase (internal hydrogen) as well as during operation (external hydrogen). External hydrogen gas can be adsorbed on the metal surface, the molecules dissociate and the atoms can be absorbed. Inside the material, interstitial diffusion of hydrogen atoms is possible, of which the diffusion constant greatly varies between different steels. Additionally, trapping of hydrogen on various sites appear, depicted in Figure 6. Since trap-sites have a higher binding-energy than interstitial sites, trapping impacts the kinetics and increase the solubility of hydrogen [29].
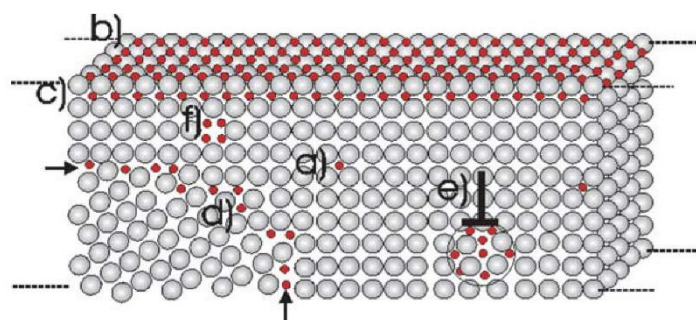

Figure 6: Possible hydrogen (trap-)sites: a) interstitial sites; b) surface sites; c) subsurface sites; d) grain boundaries; e) dislocations; f) vacancies. The figure was taken from [30].

Depending on the origin of the hydrogen and the operating conditions, a variety of features can appear. Hydrogen flakes as well as internal cracks called 'snow flakes' or 'fish-eyes' are conventionally explained by arising internal pressure [31]. While atomic hydrogen can diffuse through the lattice, molecular hydrogen cannot. When recombination of hydrogen atoms occur, the molecular hydrogen occupies 25 times the volume of atomic hydrogen and internal pressure builds up locally [29]. The pressure induces the crack formation and propagation. While the flakes are induced by the internal pressure only, 'fish-eyes' are induced by additional

tensile stress. When the steel is plastically strained at a slow rate and room temperature the two regions feature emerge [31]. The centre is a pore or an inclusion, for instance a vacancy cluster in which hydrogen got trapped, the region around the centre is characterised by local HE features like cracks and quasi-cleavage. Another feature are pinholes, which can emerge during the production process in steels which are produced by casting [29].

During or after absorption of external hydrogen, hydrogen-induced blistering can appear [29]. Based on the pressure theory, the hydrogen can aggregate at internal defects (Figure 6), recombination builds up internal pressure which can plastically deform the surrounding. Deformations near the surface can lead to visible blisters and dents at the surface. In cases of low ductility, cracks instead of blisters can arise as mentioned above. Besides cracks and blisters, in some materials hydride formation is possible [29]. Those can act as potential nucleation site for crack formation and therefore reduce the toughness of the material. However, in steel hydrogen-induced cracking or blistering is much more common than hydride formation under usual operating conditions. Anyhow, the possible effects highly depend on the specific material and the conditions.

Although the field of research was launched in 1875, there is still no unified theory on the mechanisms of HE nowadays [32]. Nevertheless, many mechanisms have been proposed which can explain individual features and are supported by experimental data or simulations. Additionally, there is no prove, that a unified theory to cover all features can be found. In the following, the most common theories will be introduced.

The oldest theory is the internal pressure theory, already mentioned above [29]. In which the internal pressures favours crack formation.

Besides the internal pressure theory, also the hydrogen-enhanced decohesion (HEDE) theory is based on local aggregation of hydrogen [29]. The agglomeration takes place in imperfections of the metal matrix like grain boundaries, but also on the tip of a crack since its field of tension leads to lattice deformations. Around those aggregations, the bonding energy is decreased, therefore crack formation and propagation is accelerated. The metallic bond breaks when the stress intensity is larger than the cohesive-force, which is reduced by the presence of hydrogen.

In the hydrogen-enhanced localised plasticity (HELP) model [29], as in the other theories, hydrogen aggregates in tension fields of dislocations. The hydrogen reduces the field of tension as well as the interaction forces between dislocations and obstacles. The dislocation mobility/velocity increases and an increased local plasticity is established. Therefore, crack propagation is enhanced.

In the hydrogen-enhanced strain-induced vacancies (HESIV) model, it has been proposed that hydrogen enhances the strain-induced vacancy formation, due to a reduction of the vacancy formation energy [29, 31]. The vacancy density increases and excess vacancies are stabilised and decelerated. The dynamics of dislocations is a major player for plasticity, which is intertwined with HE. The formation of vacancy clusters reduces the load capacity of the material. Experiments showed that the induced vacancies rather than the hydrogen itself leads to degradation, which shifted the viewpoint on HE.

Lastly, the adsorption-induced dislocation emission (AIDE) theory considers the reduction in surface energy by hydrogen adsorption [29]. Therefore, formation energies of dislocations and cracks are reduced and embrittlement takes place. The AIDE model combines the reduction of bonding energies (HEDE) with the crack formation mechanism (HELP).

In this section the most common theories where briefly introduced, detailed descriptions can be found in the literature [29, 31, 33]. It should be noted, that more approaches exist which will not be mentioned in this work. Also, most theories can explain some features but none can cover the variety of aspects connected to HE. However, there are common features between some of the theories. There are indicators that hydrogen induces changes (dislocation density, dislocation mobility etc.) which cause the degradation. Nevertheless, more knowledge in the research field is required and materials have to be tested under the specific operating conditions to guarantee the safety during their application.

2.3.2 Potential materials for Experiments

Since hydrogen storage in salt caverns is not standardised conducted yet, the most suitable construction materials still need to be selected. However, barely any research has been found about the impact of hydrogen on steel materials under salt cavern boundary conditions. The investigation of steel surface changes caused by the various salt cavern conditions are the goal of the master thesis. Anyhow, the consequences of hydrogen on steel materials for hydrogen transportation have been investigated, which give the basis for the following literature background. First, state-of-the-art research for pipeline steels is presented, followed by studies on casing and tubing steels.

2.3.2.1 Pipeline steels

One potential steel category are the pipeline steels, which are used for the transportation infrastructure of oil and natural gas. Replacing these energy sources by hydrogen, the suitability of the transportation infrastructure should be guaranteed for safety reasons. Hence extensive testing of steels in this category is required. Also, their suitability for salt caverns should be tested as it might be a potentially new application field for these steels. In the API standard, the nomenclature for pipeline steels use an X plus a number indicating the strength level of the material [34]. While there are many pipeline steel grades, in the scope of this work not all of them can be discussed. Only two examples will be presented. Those have been chosen based on their relevance and research intensity. The compositional and tensile requirements can be found in Appendix D in Figure 47 and Figure 48, respectively.

There are many studies about the impact of hydrogen on API 5L X70 steel [35-38]. Mohtadi-Bonab *et al.* investigated the steel using scanning electron microscopy (SEM), among other techniques [35]. Polished samples were electrochemically loaded with hydrogen using 0.2 M sulfuric acid solution combined with 3 g/L ammonium thiocyanate. Samples with different charging times of 1 hour to 24 hours were produced and the impact of the hydrogen was examined microscopically. Two types of damages, blisters and internal cracks, could be observed. The amount and size of the blisters showed an increase with charging times up to 1 mm for the 24 h sample. The same dependency was observed for internal cracks. SEM images of crack propagation of a sample with different charging times can be seen in Figure 7 [35]. Inside the microstructure, structural defects and non-metallic inclusions serve as points of attacks [35]. Mohtadi-Bonab *et al.* demonstrated the crack nucleation at precipitates using energy dispersive X-ray spectroscopy (EDX). Also, the grain size and (in)homogeneity of the microstructure impacts the effect of HE, for instance a finer grain structure increases the amount of hydrogen diffusion inhibitors. Nevertheless, further investigations are required, specifically experiments under salt cavern boundary conditions are necessary to assess the suitability of the X70 steel.

Besides the impact of hydrogen, also the impact of hydrogen sulphide (H_2S) has to be studied in these conditions. Wang *et al.* studied the impact of H_2S during oil/natural gas usage by using NACE-A solution with 5 % sodium chloride and 0.5 % acetic acid in which H_2S gas was bubbled for 60 min with 200 mL/(min*L) [39]. HE-effects could be found in the specimens. As H_2S destabilises the passive layer, hydrogen uptake into the material could take place. The destabilisation may have a major impact on the material degradation, especially for the usage in hydrogen systems. Additionally, H_2S has the ability to suppress the recombination of hydrogen atoms, which increases the chance of hydrogen uptake.
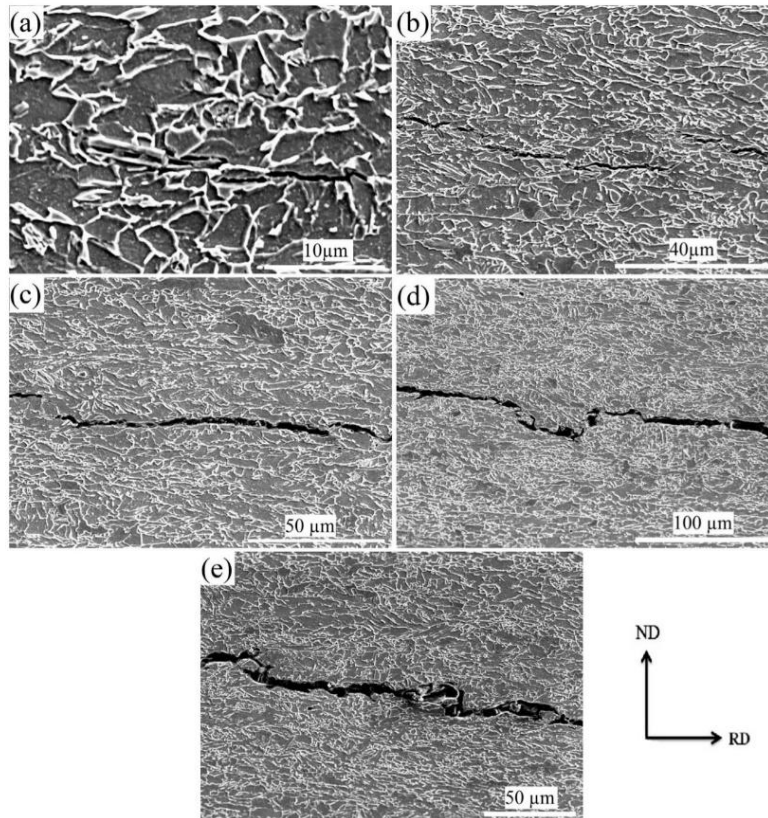
Figure 7: SEM images of crack propagation for different hydrogen charging times of X70 steel. a) 1 h charged, b) 3 h charged, c) 8 h charged, d) 15 h charged and e) 24 h charged. Additionally, indicated the normal direction (ND) and the rolling direction (RD). The figure was taken from [35].

A commonly used steel grade in European's pipeline network is API X52 [40]. Capelle *et al.* showed that hydrogen is able to penetrate into the metal's near surface layers even at pressures of 20 bar and ambient temperature, causing a change in the local fracture mechanism [40]. It has to be noted, that the results are valid for the specific test conditions only. Another investigation by Boukortt *et al.* also demonstrate HE seen by an array of surface cracks close to the fracture surface. Due to the hydrogen environment the fracture is often close to the surface caused by pitting and hydrogen attack [41]. Occasionally the fracture starts at secondary cracks.

A potential pipeline steel for the underground storage within the API X52 grade might be "H_2-ready" from Mannesmann Line Pipe GmbH [42]. Brauer *et al.* investigated two materials of grade API 5L X52, material 1 produced with a normalised hot-rolling mill; material 2 thermomechanical rolled with Mannesmann specifications for "H_2-ready" pipes [42]. For material 2, grain refinement and homogenisation were found compared to material 1. Slow-strain-rate tensile tests, conducted in 80 bar hydrogen gas environments, indicate impact of hydrogen on material 1, while material 2 shows good resistance against hydrogen-induced degradation. Since hydrogen dissociates at active metal surfaces (free of oxide layers), the creation of those should be avoided by the reduction of the occurrence of notches and ridges inside the tube [42]. Also, the reduction suppresses local tension fields and therefore critical crack growth. To improve the resistance against HE the chemical composition of the alloy plays the major role. Reduced carbon content improved the weldability and therefore decreases the probability of hydrogen penetration into the alloy. Reduction of phosphorus and sulphur content decreases the attack points of the material due to less impurities. Another major contributor to the resistance is the microstructure, which can be influenced by the production method. Brauer *et al.* stated the "H_2-ready"- pipes to be safe, clean and economic [42]. However, those results are for pipeline usage and the materials were not tested in salt cavern boundary conditions. Also, there were no independent studies available.

Since the H_2-ready production route seem promising to produce hydrogen resistant steels, in this work another H_2-ready steel from Mannesmann Line Pipe GmbH was investigated, the X56. The steel was provided from

Mannesmann Line Pipe GmbH for the study. X56 has a yield strength of 390 MPa and a minimum tensile strength of 490 MPa [43]. Although these values are not congruous, X56 steel can be produced in such a manner that it not only fulfils the requirements of X56 steel but also of J55 steel. This has been done by Mannesmann Line Pipe GmbH using their H2-ready production method. J55 is a casing steel which is commonly used for UGS, the next subsection elaborates on casing and tubing steels.

2.3.2.2 Casing and tubing steels

Casing and tubing steels might be of great relevance for the UHS in salt caverns. In the API standard, they are named with API 5CT plus an additional letter/number combination [44]. The typical application is for oil wells in the oil and natural gas industry. But some of the materials in the class are developed for underground storage in caverns, for instance Mannesmann Line Pipe GmbH developed API 5CT J55 (weldable) and API 5CT N80 Q (weldable) [45]. The steel grade API 5CT J55 is commonly used for UGS of natural gas in salt caverns, but their usage in traditional UGS does not automatically qualify it for the usage in UHS. Nonetheless, its investigation for UHS in salt caverns is suggestive. The chemical composition of casing steel grades is mostly the same for different grades and does not have great restrictions. The compositional restrictions for all 5CT steels as defined in ISO 11960:2004 are shown in Figure 45 in Appendix D. The distinction between the 5CT grades are conducted over their properties like yield strength and minimum tensile strength. The minimum yield strength is also responsible for the naming of the grade, for instance for J55 it is 379 MPa or in American units 55 ksi [46]. The maximal yield strength of J55 is 552 MPa and the minimum tensile strength 517 MPa [46]. The tensile and hardness requirements for all 5CT steels can be found in the Appendix D in Figure 46.

Boersheim et al. tested the impact of hydrogen on materials typically found in UGS-facilities in Germany [47]. The materials typically found include the casing steel grades N80, P110, K55 and J55; the exact types were not published for reasons of confidentiality. N80, K55 and J55 were tested in an autoclave set-up, recreating UGS conditions containing hydrogen, for 4 weeks but without pressure and temperature cycles. Within the set-up, brine was placed and temperature and pressure were kept at 100 °C and 100 bar, respectively. Stress-strain measurements of the steels before and after exposure to hydrogen can be seen in Figure 8, while a change in shape is visible, HE is not visible. It should be noted, that the moment of failure is not shown in the plots and the scale was not normalised.

Trautmann et al. studied the impact of hydrogen on API 5CT P110, which was regularly found in caverns [47], as well as on L80, which is used for wells in sour environment [48]. The materials have a martensitic microstructure with former austenite grains having the size of 20 μm to 40 μm. The maintaining austenite amount was lower than the detection limit of 1 %. The materials were tested for 30 days in an autoclave at 25 °C and 80 °C with hydrogen gas at partial pressures of 20 bar and 100 bar [48]. Omission and addition of an electrolyte represented dry and wet conditions. An additional test with 5 bar CO_2-gas added were conducted as well. The resulting hydrogen content in L80 and P110 can be seen in Figure 9 and Figure 10, respectively. The results show an increase in hydrogen uptake with temperature and pressure, wet conditions further promote the uptake. Overall, the hydrogen absorption during the testing was low and did not cause HE leading to failure under 90 % specified minimum yield strength of constant load.

Besides investigations of hydrogen gas impact, also the influence of hydrogen sulphide was tested [48]. These tests were conducted at ambient pressure in an acidified H_2S-saturated aqueous brine solution with 5.0 wt.% NaCl and 0.5 wt.% CH_3COOH for 14 days. The hydrogen content as function of time for P110 can be seen in Figure 11. The hydrogen uptake is about one order of magnitude larger than for the autoclave measurements (Figure 10) and the curve can be explained due to the formation of corrosion products. For P110 steel, the test conditions lead to failure within 10 min, while L80 steel did not fail in the measurement period of 14 days.
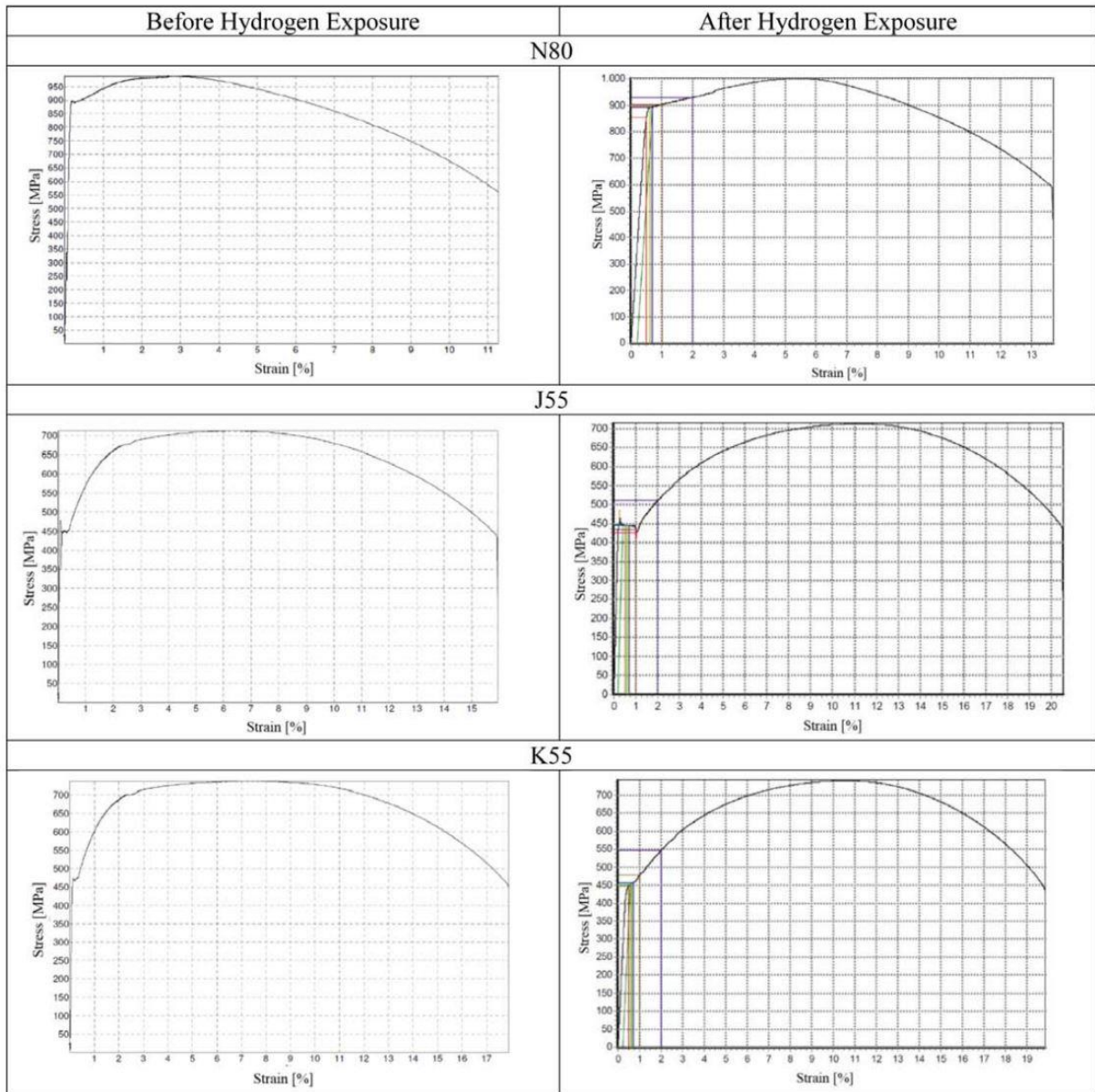
Figure 8: Stress-strain curves for N80, K55 and J55 steel samples before and after hydrogen exposure. Taken from [47].
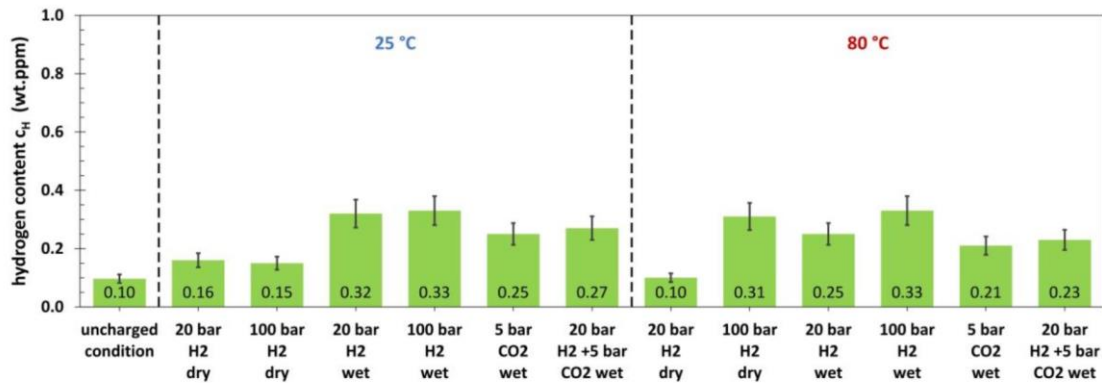

Figure 9: Resulting hydrogen content in L80 steel after testing for 30 days in an autoclave under various temperatures and pressure combinations. Wet conditions describe the addition of an electrolyte with 15,000 ppm Cl⁻. Taken from [48].
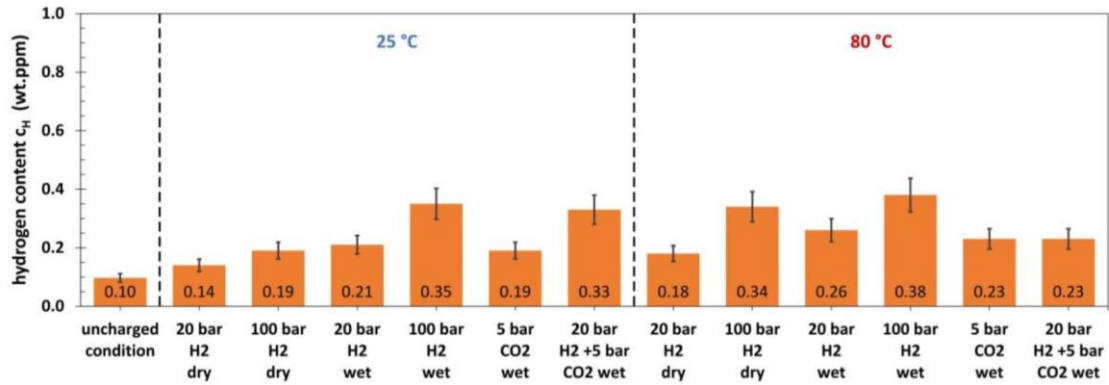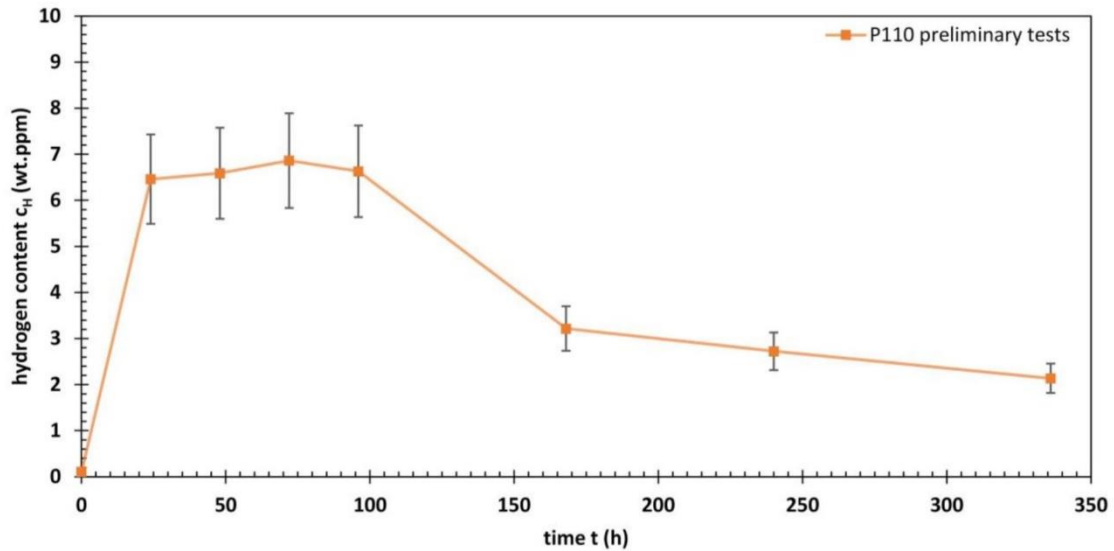
Figure 10: Resulting hydrogen content in P110 steel after testing for 30 days in an autoclave under various temperatures and pressure combinations. Wet conditions describe the addition of an electrolyte with 15,000 ppm Cl⁻. Taken from [48].

Figure 11: Hydrogen content vs time measurement of P110 steel. Test were conducted in room temperature at ambient pressure in an acidified H_2S-saturated aqueous brine solution with 5.0 wt.% NaCl and 0.5 wt.% CH_3COOH for 14 days. Graph was taken from [48].

Despite the topicality of the subject, not much literature could be found on the impact of hydrogen on API 5CT J55 and N80 Q. Therefore, related literature was consulted as well. Willett investigated the susceptibility of electric welded J55 to hydrogen-induced cracking (HIC) [49]. Extensive HIC was observed during a mill audit, which was ascribed to centerline segregation and inhomogeneity of the microstructure. Although the experimental set-up is not closely related with the material testing under hydrogen salt cavern boundary conditions. It should be noted, that under specific treatments and conditions, HE might occur in the material and therefore testing is of high importance. In addition, the example shows, that the pipeline welds should receive some attention.

In the present master thesis, a conventional J55 steel and the H_2-ready X56 steel were examined with regards to the salt cavern boundary conditions. Surface investigations were conducted and the results of the two steels were compared. For simplification reasons the H_2-ready X56 steel, which could also be classified as J55 steel, will be named X56 only. Since surface cracking was expected to take place, for the surface investigation, some background on mechanism of crack formation is required, which will be presented in the next subsection.

2.4 Mechanism of crack formation

In this subsection, crack formation will be introduced, to gain some understanding of the different mechanisms and morphologies.

2.4.1 Corrosion fatigue

Corrosion fatigue (CF), as the name indicates, combines the impact of fluctuating or cyclic stress with a corrosive environment [50]. In general, mechanical loading, metallurgical and environmental variables come into play for CF. But CF is not specifically defined for each material, since it highly depends on the conditions, in which the environment decreases the fatigue life of the material. While mechanical damage is more likely at high load and frequency, intermediate load and frequency increase the probability for corrosion damage. Hence corrosion fatigue is highly complex due to the many influencing factors.

The mechanism of CF is based on localized slip within grains caused by the stress within a cycle [50]. The adsorption of air hinders the rewelding in the reverse stress cycle. Cracks are produced. While this step is based on the mechanical stress cycles, the corrosion removes barriers to plastic deformation, reducing the surface energy which induces plastic deformation and favours slip formation by injection of dislocations along slip planes. The crack initiation mostly takes place at the surface and is independent on the fatigue limit. The initiation is usually associated with surface defects or discontinuities. Localized corrosion such as pitting favours the initiation as it serves as stress concentrator and is correlated with a local acidic environment. The two main mechanism of CF are anodic slip dissolution and HE.

Crack growth by anodic slip dissolution is caused by the diffusion of active water molecules and halide ions to the crack tip. The high concentration of diffused molecules/ions at the crack tip can cause rupture of the passive film and fretting contact between the crack faces [50]. The formation of corrosion products takes place. Crack growth by HE involves diffusion of water molecules or hydrogen ions to the crack tip. There adsorption and absorption as well as the diffusion to critical locations is possible. As described in the section for HE earlier, the tension field of the crack tip attracts hydrogen atoms. The cyclic loading again evokes fretting, but also pumping of aqueous medium to the crack tip by the walls. The blunting and re-sharpening of the tip also impacts the dissolution rate.

The morphology can be described as fine-to-broad cracks with rarely any to no branching, often in transgranular fracture paths [50]. Samples suffering CF may also have pits, grooves or other stress concentrators. In high strength steels CF damage combined with hydrogen damage can be difficult to distinguish from other forms of hydrogen damage. In carbon steels, cracks often arise in corrosion pits and contain corrosion products. The cracks often follow transgranular fracture path with possible branching. However, pits and transgranular fracture are not necessary requirements for CF in carbon steels, but rather can be seen as indicators.

2.4.2 Environmentally induced cracking (EIC)

In specific environments microscopically, brittle fracture of materials can occur below the yielding strength [50]. The susceptibility is connected to the chemical composition and the microstructure of the material as well as an interaction between electrochemical dissolution of the metal, hydrogen absorption of the metal and the mechanical loading factors.

2.4.2.1 Stress corrosion cracking

There are some conditions which need to be fulfilled for stress corrosion cracking (SCC) to take place [50]. The environment needs to be crack-promoting. The material needs to be susceptible to SCC and the threshold value regarding tensile stress needs to be exceeded. While some cracking methods are hard to distinguish, SCC has a striking feature: the stress corrosion faces suffer low corrosion even in damaging solution. The morphology of failed specimen appears brittle in a macroscopic scale. Also, strongly branched cracks can be observed. SCC failure is often caused by residual stresses, possibly caused by cold work or heat treatment. Welds and inserts are often sources of stress, increasing the risk for cracking.

2.4.2.2 Hydrogen-induced cracking

In hydrogen-induced cracking (HIC) brittle fracture occurs under sustained load and in the presence of hydrogen [50]. The mechanism depends on hydrogen fugacity, materials properties (strength, microstructure), the applied stress, and the temperature. While threshold values exist below which HIC occurs, the threshold depends on the material properties and the specific environment and is therefore hard to define. In contrast to the crack morphology of SCC, hydrogen stress cracking produces sharp singular cracks without extensive branching. The damage caused by hydrogen can be accelerated by H_2S, CO_2, Cl^-, CN^- and NH_4^+, for instance by suppression of the recombination of nascent hydrogen atoms. In steels with pearlite structures the cracks propagate rather in a straight manner, but also stepwise can take place.

One type of HIC is hydrogen-induced blistering, which occurs in lower strength steels with tensile strengths <550 MPa and yield strength <535 MPa [50]. The reason behind blistering lies within the pressure-theory. Some of the absorbed hydrogen diffuses into a void inside the material and gets trapped. Recombination within the void builds up pressure from the inside, forming blisters and resulting in HIC.

2.4.2.3 Sulphide stress cracking

Sulphide stress cracking (SSC) is a specific case of HIC, which can take place in hydrogen sulphide medium [50]. It rather effects high-strength steels and localized hard zones for instance in welds. Like in HIC, SSC depends on the material's characteristics as well as the applied stresses. It is directly related to the absorbed hydrogen and normally occurs below 90 °C.

2.4.2.4 Stress-oriented hydrogen-induced cracking

Like hydrogen blistering, stress-oriented hydrogen-induced cracking (SOHIC) is caused by hydrogen absorption followed by internal recombination [50]. Due to external or internal stress the internal recombination of hydrogen atoms produces microfissures. While blisters from HIC or SSC can initiate SOHIC, these cracking methods are not a necessary precondition for SOHIC. The preferential occurrence is in the base material next to welds, where SSC could initiate it. The cracking direction can either be perpendicular to the applied stress or in the plane defined by non-metallic inclusions.

2.4.3 Overall phenomenon of crack formation

As described, there are multiple causes of cracking in a corrosive environment. While CF requires loading cycles, EIC are based on static or slowly increasing loads. Depending on the conditions, even simultaneous occurrence is possible, which hardens the allocation of cracking to a specific mechanism [50]. The morphology can be dominated by the crack initiation process or the propagation. As many environmental factors impact the cracking method and a complex relation exist between the methods, the distinction is extremely difficult. To distinguish between SCC and HE the use of electrochemical polarization technique can be suitable.

2.5 Characterisation techniques

In this subsection, the two characterisation techniques used in this work will be introduced briefly.

2.5.1 Scanning electron microscopy (SEM)

The SEM is an optical characterisation technique, which allows the user to depict the specimen surface with a spatial resolution down to 1 nm, depending on the diameter of the incident beam [51]. The general structure of the SEM is represented in Figure 12. For the generation of an electron beam, different electron emitters exist [52]. They can be categorised in thermionic emitters, field emission emitters and Schottky emitters. In Figure 12 the emitter is represented in the top with a cathode and a Wehnelt cylinder. An anode accelerates the electrons, which are then bundled through a lens system of various electromagnetic lenses and focused onto the sample. The electron beam scans over the surface, where the electrons interact with the surface and subsurface atoms emitting secondary electrons (SE), backscattered electrons (BSE), Auger electrons (AE) and X-rays. Various detectors are used to analyse the emitted particles and a surface image is generated.
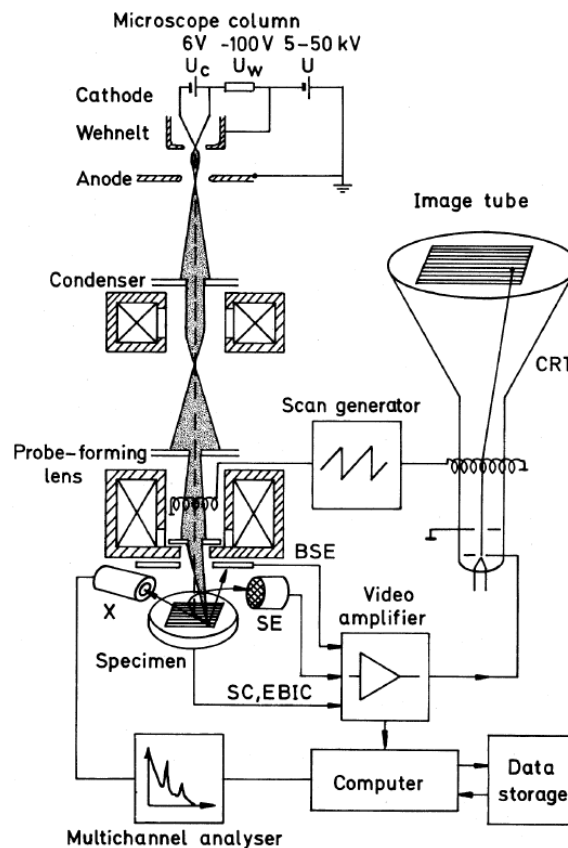
Figure 12: Sketch of general scanning electron microscope structure, including the electron source and acceleration, the electromagnetic lens system, the specimen, various detectors and the imaging set-up. The figure is taken from [53].

2.5.2 Energy dispersive X-ray spectroscopy (EDX)

The EDX is used to determine the elemental composition of surfaces. It is commonly used as add-on tool in SEM devices and makes use of its electron beam. The interaction of the electrons with the surface and subsurface atoms leads to emission of X-rays [52]. Each element emits X-rays with characteristic energy, which allows the identification [54]. An X-ray detector attached to the SEM analyses the X-rays, allowing the software to generate an EDX spectrum or elemental map [52]. The EDX spectrum is a plot of counts vs energy level in keV.

3. Experimental

The purpose of the study is to microscopically investigate the impact of the conditions in a salt cavern, in usage for hydrogen storage, on casing/pipeline steel. Therefore, steel samples were produced in varying conditions of pressure and temperature cycles, pressurised hydrogen/nitrogen gas as well as presence of moisture and brine. Afterwards, the samples were characterised using SEM and EDX techniques. In this chapter the experimental procedure is describe divided in 3.1 Sample preparation and 3.2 Sample characterisation.

3.1 Sample preparation

In Figure 13 an overview is provided to introduce the reader to the various conditions of the sample preparation. Two type of steels, J55 and X56, were used in two surface states each, untreated and sanded, resulting in four test series. Each sample was exposed to temperature and pressure cycles in either hydrogen gas or nitrogen gas. While one sample for each state and gas was prepared in a dry chamber, additional exposure to water and brine inside the chamber was conducted for the other two specimens. The combination of gas and chamber conditions result in six specimens per test serie. In the following, the procedure will be described in detail.
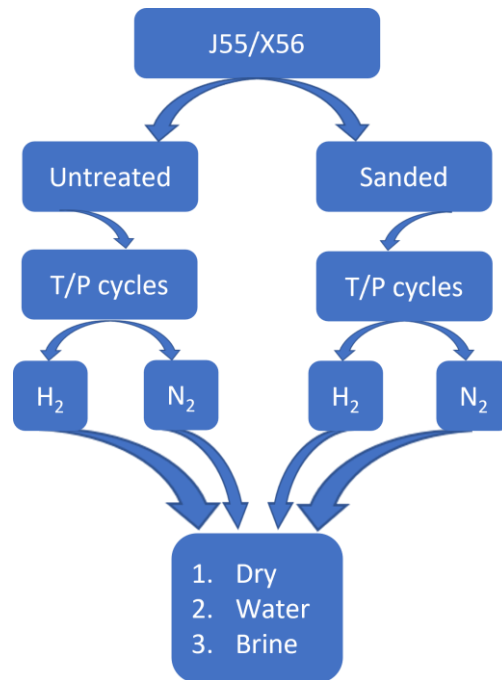
Figure 13: Overview scheme of sample preparation conditions. Two steels (J55 and X56) were used in two surface states each (untreated and sanded). For all samples temperature and pressure cycles were applied. The exposure was given by either hydrogen gas or nitrogen gas with 1. dry, 2. water or 3. brine conditions in the chamber.

For the sample preparation, high-pressure reactors "BR-500" from Berghof Products + Instruments GmbH were used as autoclave. The BR-500 reactor consists of a 316Ti stainless steel cylinder with an inner PTFE cylinder. The inner volume amounts to 500 mL. A CAD drawing of the BR-500 reactor was provided by Berghof Products + Instruments GmbH and is shown in Figure 14. Above 150 °C the maximal allowed pressure inside the reactor is 165 bar, due to the usage of a rupture disc. In this work, the pressure range was 90 to 150 bar and the temperature were cycled between -10 °C and 160 °C. The temperature cycles were regulated using the process thermostat "Grande Fleur" from Peter Huber Kältemaschinenbau AG. The reactor temperature was constantly measured using a PT100 element and recorded by the thermostat. It has to be noted, that the pressure cycling is a consequence of the temperature cycles and was not actively conducted.

The experiments were conducted to study the impact of the salt cavern boundary conditions. Within a real cavern, the permanent brine induces moisture and salt ions, as well as potential contaminants such as hydrogen

sulphide gas. The storage process itself induces the hydrogen gas which is to be stored as well as temperature and pressure.

To study the impact of the individual conditions, these were individually simulated within the autoclave for 72 hours. Since hydrogen potentially intensify occurring condition consequences, for instance cracking of the surface, the experiments were conducted in pressurised hydrogen gas and simultaneously in pressurised nitrogen gas in a second autoclave. Therefore, it is possible to determine whether the surface feature originates from the condition in general, or from the condition including hydrogen atmosphere. Hydrogen gas and nitrogen gas was used from Linde GmbH in 6.0 purity (>99,9999 %) from 50 L - 200 bar cylinder and 40 L – 200 bar cylinder, respectively. In advance to the start of the experiment, the specimen was placed inside the PTFE cylinder and the chamber was purged 6 times with the process gas (hydrogen or nitrogen) at 100 bar and vented into the fume cupboard. The pressure and temperature cycling were regulated only over the temperature cycling. Starting the experiment at room temperature (approx. 25 °C), the process temperature was set to 160 °C. Once the temperature was measured by the PT100 element, the temperature was kept constant for 4 hours. Afterwards the process temperature was set to -10 °C, once reached it was kept constant for 4 hours again. The heating and cooling were repeated for 5 times resulting in 6 cycles. After the last cooling, the temperature was raised to room temperature again, at which the experiment was stopped. The procedure was set filling the timeframe of 72 hours. A scheme of the cycling process is shown in Figure 15. In the end of the experiment at room temperature the hydrogen/nitrogen gas was vented in the fume cupboard, the reactors were opened and the samples were removed. After the removal, the samples were rinsed with isopropanol (Roth 2-Propoanol, purity ≥ 99.5 % for synthesis) and dried with a nitrogen gas gun. The pressure and temperature cycling were conducted in all experiments. However, besides hydrogen/nitrogen gas at dry condition, additionally 20 mL liquid was used to simulate either moisture or brine. For the moisture high-purity water ($\rho \geq 18{,}2$ MΩ/cm) was used and the brine was artificially recreated in regards to the measured composition of a brine extracted from a salt cavern in Jemgum operated by the EWE GASSPEICHER GmbH. The measured composition of the extracted brine is subject to confidentiality; however, the weighing of the artificial brine is shown in Table 2. The artificial brine was mixed based on K_2SO_4, $CaCl_2$, $MgSO_4$, NaCl, KBr. The weighing and mixing were conducted by Holger Janßen in advance to the start of the Master thesis. Due to the varying conditions in the process gases (hydrogen and nitrogen) and process conditions (dry, water and brine) in total 6 samples per test series were received. Each condition was conducted with one sample only. Samples produced with liquid (water or brine) inside the reactor were partly immersed into the liquid to accelerate ageing processes, providing two surface areas for testing.

Table 2: Composition and weighed mass for 4 L artificial brine used for autoclave experiments.

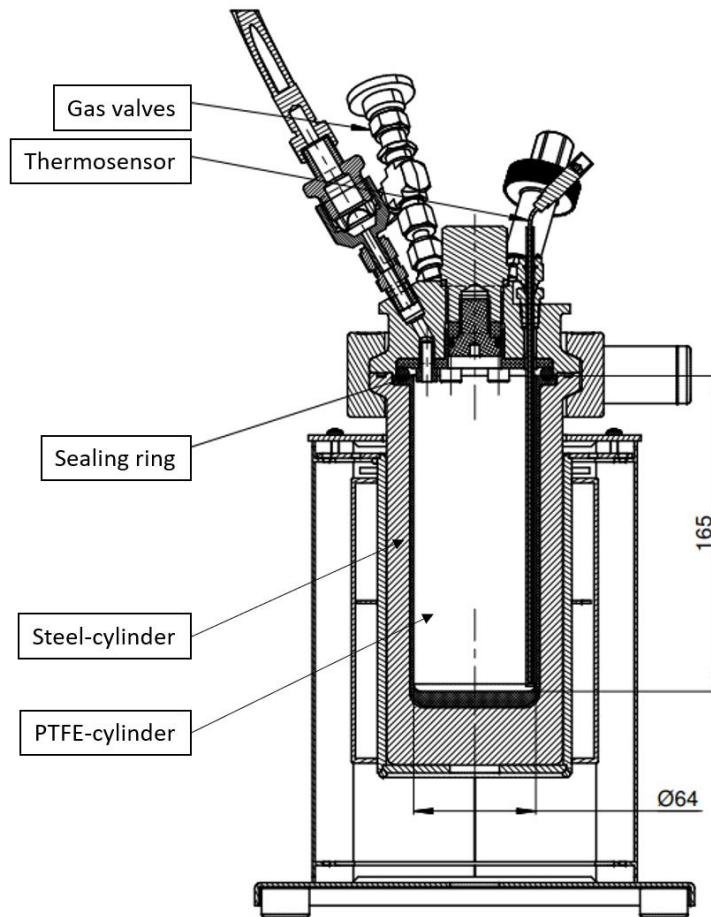|	c / mg/L	m calculated / g	m weighed out / g
Sodium	126,810.00	507.24	507.24
Potassium	574.00	2.30	0.13 (KBr) + 2.17 (K_2SO_4) = 2.30
Magnesium	246.00	0.98	3.44
Calcium	945.00	3.78	3.78
Chloride	192,903.00	771.61	760.86 (NaCl) + 6.68 ($CaCl_2$) = 767.54
Sulphates	4070.00	16.28	2.65 (K_2SO_4) + 9.73 ($MgSO_4$) = 12.38
Bromide	28.00	0.11	0.27

Figure 14: CAD drawing of BR-500 reactor provided by Berghof Products + Instruments GmbH.
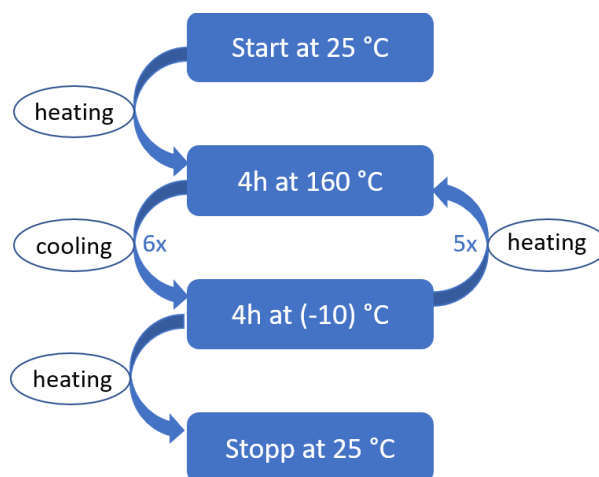

Figure 15: Temperature cycling scheme for 72 hours autoclave experiments of steel specimen placed in a BR-500 (Berghof Products + Instruments GmbH) reactor. The temperature cycling was regulated using the thermostat "Grande Fleur".

The experiments were conducted for two type of steel: J55 (coated) and X56. The J55 steel were chosen, as it is commonly used for salt cavern storage of natural gas. A continuous usage would be beneficial, which requires studies to test its suitability. The X56 steel were chosen since it is produced as H_2-ready steel, suggesting higher resistance against the hydrogen stored inside the cavern. Additionally, although it is classified as pipeline steel, the used steel fulfils the criteria for J55 steels, enabling comparability between the two steels to some degree. The J55 samples were provided by the project partner EWE GASSPEICHER GmbH and the X56 samples were provided by the steel producer Mannesmann Line Pipe GmbH. Since geometrical aspects of the test specimen can have an impact on the result, the samples were cut out of a pipe by water jet

cutting in squares of 20 mm * 20 mm. Hence the inner stresses due to pipe curvature and thermal treatments were expected to be comparable to the stresses if applied in the salt cavern system. The sample thickness of the J55 is approx. 19 mm and the thickness of X56 approx. 13 mm. Pictures of the pipe cutting can be found in Appendix A – Experimental.

The steel specimens were used in two surface states: untreated and sanded. The sanding was conducted to accelerate ageing processes due to three effects. Firstly, the sanding process induces cracks inside the material. Hence, further cracking is simplified. Secondly, the surface structure due to the sanding enlarges the surface area, which increases the attack area for corrosion and hydrogen. Thirdly, hydrogen uptake takes place at active metal surface. Due to the removal of the oxide from the sides, active metal surface is provided and hydrogen uptake probability therefore increased. The J55 samples were sanded by hand using P180 sanding paper. For the X56 steel the process was optimised by using the LaboPol-20 sanding machine from Struers GmbH with the MD-Piano 220 from Struers GmbH. The MD Piano 220 is a resin bonded diamond disc with a hardness classification of HV 220. For both steel grades only the four sides facing the pipe were sanded not the exterior and interior of the pipe. This approach was chosen to maintain coatings and curvature of the specimens. The sanded specimen was washed for 2 min in isopropanol (Roth 2-Propoanol, purity $\geq$ 99.5 % for synthesis) in the "Elmasonic S10H" ultrasonic-bath, the specimen was removed, the isopropanol replaced and the specimen washed for 2 min more in the ultrasonic-bath. The washing was conducted to remove any potential contaminants caused by the sanding process.

Besides the 72 hours experiments, two weeks experiments with hydrogen gas were conducted for the extreme conditions (dry and brine) and both surface states (untreated and brine), to examine the effect of long-term exposure. The extreme conditions were chosen, since most information flow was expected. Additionally, as outlook, one 2-week experiment was conducted for sanded J55 with hydrogen gas (6.0 purity) with 40 Mol-ppm H_2S from Air Liquide S.A from a 40 L – 150 bar cylinder, to study potential gas contaminations during storage in a salt cavern caused by microorganism-catalysed reactions. The concentrations of such contaminations in a salt cavern are not known yet. The concentration for the study was chosen based on the 0.004 ppm allowed for fuel cell applications [20] multiplied by 20 years á 365 days of minimum lifetime of the salt cavern. The relatively high concentration is supposed to accelerate the ageing process and to compare the sample with the pure hydrogen scenario.

3.2 Sample characterisation

Before characterisation of the specimens, they were washed to remove salt and loose dirt. The washing was conducted by 2 steps in the "Elmasonic S10H" ultrasonic-bath. Firstly, they were immersed in ultrapure water for 2 min then the water was rinsed off with isopropanol. Secondly, they were immersed in isopropanol for 2 min then the specimens were dried with a nitrogen gas gun. The isopropanol was used to remove the water to prevent corrosion processes caused by the cleaning through water.

The samples were investigated using the "ZEISS NEON 40 EsB" for SEM and EDX imaging. To compare the samples to each other, each sample was characterised with 15 kV acceleration voltage at a working distance of 4 mm. For all samples generally, the same magnifications were used, including 35X, 100X and 200X. EDX was conducted with magnification 35X at three surface areas, to generate an overall elemental distribution of the surface. The mean value of all three measurement was used as representation of the weight percentage of an element. The error value was determined as sum of the standard deviations of the three measurement values plus the maximal error of the values determined by the EDX device. Additionally, the presence of pits and cracks was checked scanning over the surface with approximately 500X. Pictures of the pits were made with 320X or 360X, and for cracks magnifications of 1000X, 3500X and 8000X were used. Also, EDX measurements were conducted at distinctive points at visible features like cracks and pits. Samples which were treated in liquid (water or brine) in the chamber experiment were examined at the surface which was exposed to liquid, as well as at the surface which was exposed to gas (H_2 or N_2).

Individual specimen cannot be characterised before and after the reactor experiment, as the test set-up requires carbon tape for the sample fixation onto the SEM sample holder. The tape contaminates the sample. Hence reference samples are needed for the comparison. Since there are no identical specimen, but each specimen is an individual piece of the pipe, more than one sample needed to be studied for the reference. Consequently, three separated pristine specimens were characterised and the mean values are used as reference. The reference specimens were not in the reactor at any time.

For both pristine steels, microstructural imaging was conducted. For this, the steel samples were sanded with the LaboPol-20 sanding machine from Struers GmbH. In the beginning, the sanding was done with the MD-Piano discs 80, 220 and 500 from Struers GmbH. The sanding was continued with SiC Foils 800, 1200 and 2000 also from Struers GmbH, which were hold in place by the MD-Gekko. The MD-Gekko from Struers is an adapter disc for sanding foils for magnetic fixation. After the last sanding step (SiC 2000 foil), the sample was polished using polishing cloths and mono-crystalline water-based diamond suspensions by Schmitz Metallographie GmbH. Firstly, the MolTEC was used with 3 µm diamond suspension; followed by NapTEC with 1 µm suspension and ChemTEC with 0.25 µm suspension. In between the specimen was rinsed with water, after the last polishing the specimen was rinsed with water and cleaned in the ultrasonic baths "Elmasonic S10H" in isopropanol (Roth 2-Propoanol, purity $\geq$ 99.5 % for synthesis) for 2 min and dried with the nitrogen gas gun. The surface was visually checked for scratches. For visualising the microstructure, the polished surface was etched with Nital 3 % (97 mL Ethanol and 3 mL HNO_3). The etching was conducted with a sterile "Rotilabo cotton" bud from Roth GmbH + Co. KG until the mirror finish vanishes and a cloudy finish becomes visible. Then the specimen was dunked in deionised water, rinsed with isopropanol and dried. The imaging was conducted with the "ZEISS NEON 40 EsB" SEM and EDX measurements were recorded. The grain size was determined by averaging the length of multiple grains in different directions. 200 to 300 length measurements per sample were conducted for this purpose, and the average of three specimen per steel considered. The evaluation was conducted in imageJ.

4. Results and Discussion

In this work the impact of UHS salt cavern boundary conditions on casing and pipeline steel was investigated. The studied conditions are a dry chamber as well as moisture induced by water and salt ions induced by the artificial brine. As constant values the hydrogen itself and temperature/pressure cycles are present. Each condition was conducted in hydrogen gas and nitrogen gas for an allocation of the impact of hydrogen gas, yielding 6 specimen per test series. The experiments were conducted in an autoclave for 72 hours. In total, 4 test series were conducted, based on two type of steels (J55 and X56) in two surface states (untreated samples and sanded samples). In addition, 8 two weeks experiments were conducted in hydrogen gas; 4 per type of steel. For these long-term experiments, untreated and sanded state were used in dry and brine conditions. The 2-weeks experiments were conducted to visualise the effect of long-term exposure. All samples were characterised with SEM and EDX. Due to the amount of SEM images as well as EDX data, only a selection of the images and data will be shown in the main part of this work, Appendix B – Results will be used for a larger collection.

In the following, the results of the experiments will be shown and the specific discussion on the results conducted. Within each subsection, first J55 will be discussed, afterwards X56. However, for X56 the focus lies upon the differences to reduce repetition within the specific discussion.

4.1 Microstructural Characterisation of Steels

The microstructure of a material is an important factor for its properties. It impacts the mechanical properties greatly and it plays a crucial role for the interplay of the material with hydrogen. Hydrogen can get trapped at grain boundaries, interstitial sites, impurities etc. (see Figure 6). Hence, some knowledge of the present microstructure could help during the interpretation of the results. The microstructure has been made visible by polishing up to 0.25 µm and etching with 3 vol. % Nital etch.

4.1.1 Microstructure of J55

In Figure 16 the microstructure of the studied J55 steel is shown. Visual comparison with literature images of the grains indicate the microstructure to be a mix of ferrite and pearlite [55], which is in agreement with the results of Hassan Sk *et al.* [56]. Using three specimens, the average grain size has been determined to 6.94 µm.
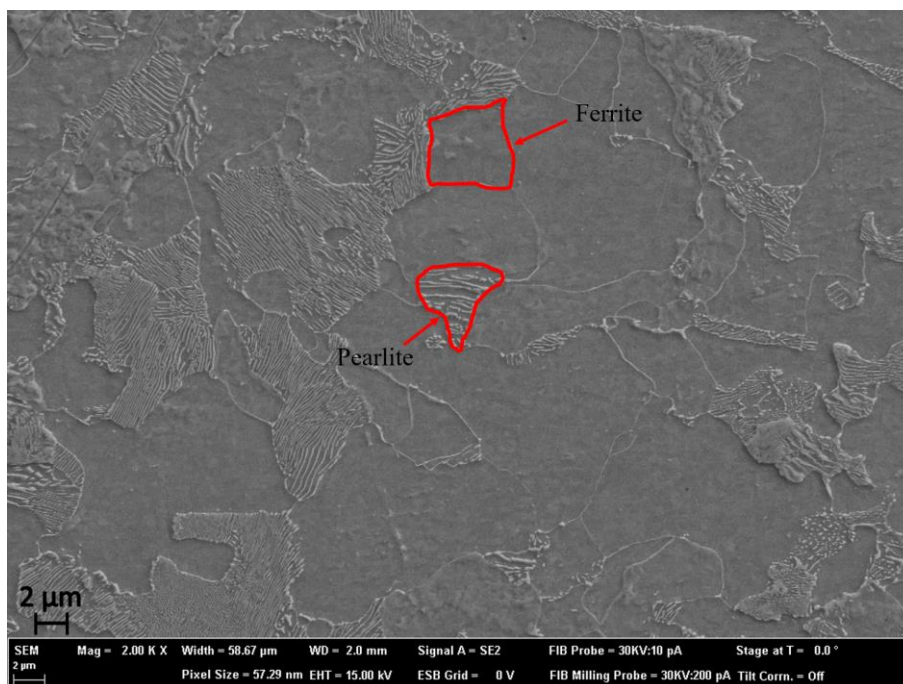
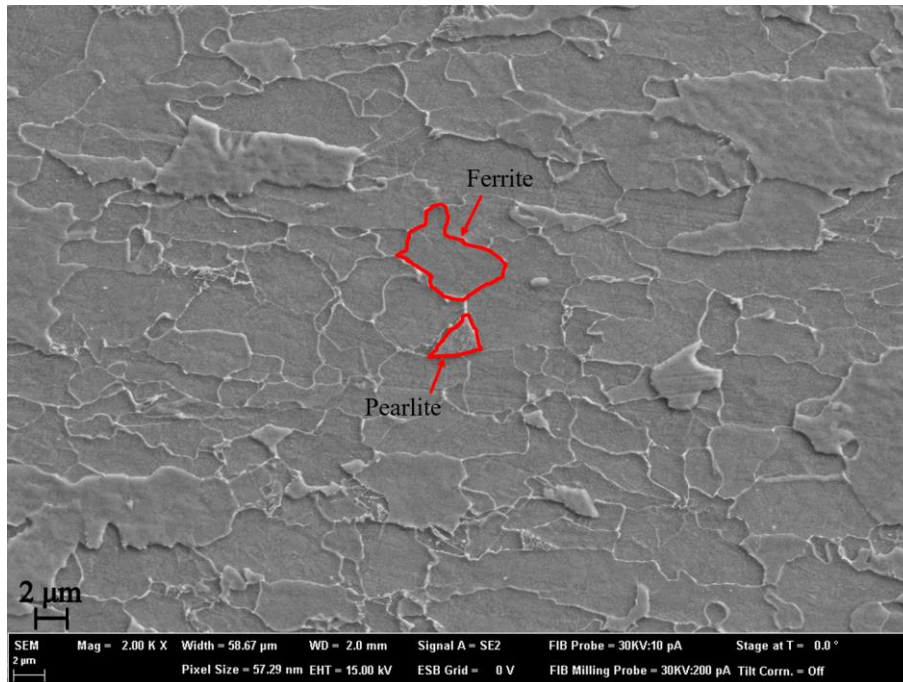**Figure 16: Microstructure image of J55 reference. J55 was polished up to 0.25 µm and etched with 3 vol.% Nital. Visible are ferrite and pearlite grains.**

4.1.2 Microstructure of H₂-ready X56

The microstructure of the X56 steel, shown in Figure 17, is a ferrite microstructure with small isolated pearlite grains. The microstructure was determined by visual comparison with literature images [55]. This result is in accordance with the results by Clover *et al.*, who found X56 with ferrite structure in one sample and a mix of mainly ferrite with small pearlite grains in another sample [57]. The microstructure depends on the chemical composition as well as the production route. Averaged over three specimen the grain size was determined to 3.95 µm.

Figure 17: Microstructure image of X56 reference. X56 was polished up to 0.25 µm and etched with 3 vol.% Nital. Visible are ferrite grains and small isolated pearlite grains.

4.2 Energy dispersive X-ray spectroscopy characterisation of steels

In this subsection the EDX results are presented. The EDX is able to detect the surface composition as it measures the energy of X-rays emitted by excited elements. Each element has a characteristic X-ray spectrum which acts like a fingerprint for its identification. In the different device settings, either an area or individual points can be measured. Within this work, the surface of the specimens is characterised, for which the chemical composition provides some insight in potential reactions between the samples and their environment. While hydrogen cannot be detected using EDX, iron and oxygen amounts provide insights in corrosion aspects.

The EDX surface data of the experiments are visualised in the pillar charts in the subsections below. In these charts, iron and oxygen are shown only, the extended pillar charts including all elements determined by EDX can be found in Appendix B – Results. Iron and oxygen were chosen since corrosion aspects are represented by these two elements. The pillar charts are structured with a colour code. Grey colour is used for reference samples. It has to be noted, that the EDX results for the reference consists of the average of three reference specimen. The averaging has been conducted since the characterisation of one steel cuboid before and after the autoclave is not possible. Hence, the reference has to be determined separately. The red pillars represent the specimens exposed to hydrogen, while blue represents exposure to nitrogen. For the red and blue pillars, the results are allocated to one sample each. Samples immersed in liquid provided two surfaces, one water/brine side and the gas side, resulting in two EDX results for one sample.

4.2.1 EDX results and discussion of J55

4.2.1.1 Short-term exposure

In Figure 18 the EDX data for the 3 days experiments of J55 are shown. The figure is structured in the variable process conditions; the left column is for untreated steel and the right column for the sanded steel. The rows are ordered considering the condition, from dry (top row), ultrapure water, to brine (bottom row).
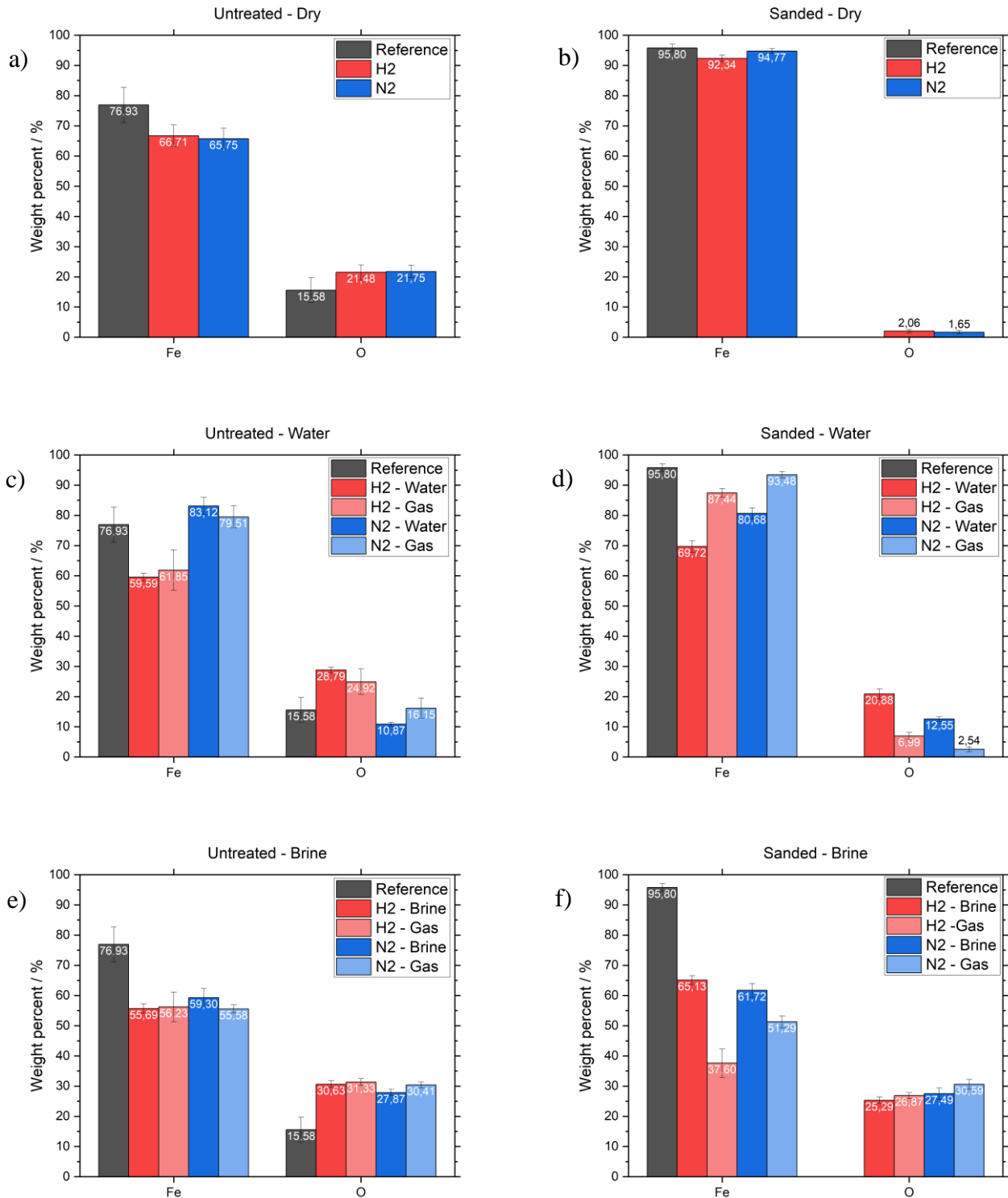

Figure 18: EDX data for Fe and O on J55-samples surface of 3 days experiments. a), c) and e) for untreated specimens and b), d), and f) for sanded specimen. Dry (a, b), ultra-pure water (c, d) and brine (e, f) conditions in H₂ (red) and N₂ (blue) are compared to reference (grey).

Generally striking is, that the weight percent of iron decreases due to the chamber experiments while the weight percent of oxygen increases, with one exception for the untreated sample with water and nitrogen inside the chamber. However, since the weight percent of the reference is the average of three samples, the real values of the specific specimen before the autoclave experiment are not known and the results will be seen as an exception. Nevertheless, the general trend indicates that the surface is corroding during the experiments.

In the dry condition (Figure 18a, b), less iron oxide formation takes place than in the conditions including some liquid (Figure 18-f). While in dry conditions, oxide formation is generally much lower than in the presence of moisture, these samples show particularly low oxide formation due to the exposition to high purity hydrogen / nitrogen gas. Since there is barely any oxygen gas or water (≤ 1 ppm [58, 59]) expected in the high purity gases (6.0 purity), the potential cathodic reactions should not be able to take place. The Pourbaix diagram of water is shown in Figure 19, the corresponding reactions are not shown to keep the Figure clear. The cathodic reaction of interest depends on the pH of the liquid, for acidic solutions [60]:

$$O_2 + 4H^+ + 4e^- \leftrightarrow 2H_2O \tag{4.1}$$

For alkaline solutions:

$$O_2 + 2H_2O + 4e^- \leftrightarrow 4OH^- \tag{4.2}$$
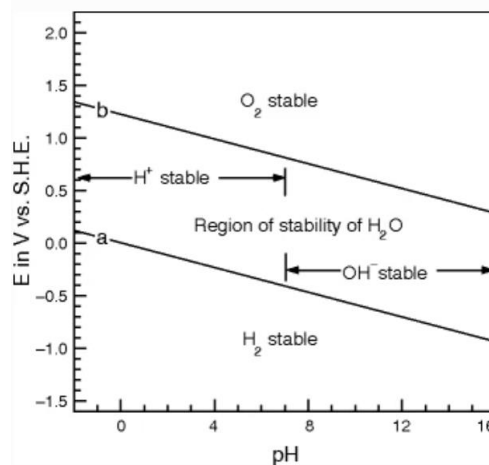
Figure 19: Pourbaix diagram of water. Taken from [60].

Although the cathodic reaction should not be able to take place, still oxide formation is visible in the EDX results since the iron values decrease and oxygen values increase. Also, for the hydrogen samples (untreated and sanded) moisture was observed inside the chamber when removing the samples after the experiment. One possible explanation for the moisture would be the reaction 4.3. The reaction was introduced earlier (2.4) as reaction catalysed by microorganisms, in dry conditions no microorganisms are present. However, since the microorganisms are a catalyser only, their absence do not exclude that the reaction take place at much slower rate.

$$H_2 + Fe_2O_3 \rightarrow 2FeO + H_2O \tag{4.3}$$

However, wüstite is not stable below 570 °C, which further decreases the probability of the reaction 4.3 to neglectable amounts [61]. Below 570 °C a stepwise reduction of Fe_2O_3 with intermediate formation of magnetite (Fe_3O_4) is more likely as shown in reaction 4.4 and 4.5 [61].

$$3Fe_2O_3 + H_2 \rightarrow 2Fe_3O_4 + H_2O \tag{4.4}$$

$$Fe_3O_4+4H_2\rightarrow3Fe+4H_2O \tag{4.5}$$
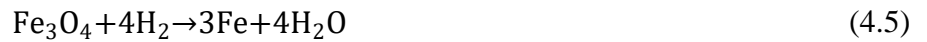
Since all samples (untreated and sanded) have iron oxide on the interior and exterior of the pipe, the hydrogen gas might reduce the iron oxide forming water molecules. Changes in the chemical composition of the exterior and interior where not characterise, hence the reactions cannot be confirmed. Even though no pure oxygen gas evolves through the reaction, the water might allow the cathodic reaction to take place and iron oxide emerges on the characterised side. While the reactions would explain why moisture were found for the samples exposed to H_2 but not the ones exposed to N_2, there is nearly identical oxide formation for both gas exposures which contradicts this explanation being the reasoning behind the oxide formation. While the reaction of the iron oxide with hydrogen still might take place, it does not seem to have an effect on the rate of rust formation of the specimen.

Another possibility is the presence of oxygen and water molecules inside the reactor. In the beginning of each experiment the chamber is purged. The number of purging cycles were determined by preliminary tests conducted by Holger Janßen in advance to the master thesis start. After filling the chamber 6 times at room temperature with 100 bar hydrogen (purity 6.0), each time venting the gas in the fume cupboard, the hydrogen purity level in the chamber was higher than hydrogen gas purity 5.0 (>99.999 %). Meaning, the oxygen concentration was lower than 2 ppm and the water concentration was lower than 5 ppm [62]. Hence oxygen and water molecules are not expected to be present in such high amount for corrosion to take place. While, the gas tightness has been checked by observation of the pressure stability, a change in the composition of the gas cannot be ruled out. Oxygen and water molecules inside the chamber would explain the nearly identical weight percent of oxygen on specimen surface (Figure 18a, b) since similar amounts might be found in a reactor filled with hydrogen gas and nitrogen gas during the experiments, enabling the same oxidation rate. In order to investigate the gas composition inside the reactor and hence potential theories on oxide formation in dry conditions, gas analysis has to be conducted in the beginning and end of the experiments. The comparison of the gas composition would allow further interpretations.

In general, samples immersed in liquid (water or brine) show significantly more iron oxide formation on the sample surface (Figure 18c-f). While this can also be seen on the surface of untreated samples, the effect is even more pronounced on sanded surface since no oxygen could be found for its reference. These results show that the corrosion effects clearly depend on moisture inside the chamber. The corrosion in water is taking place through multiple steps [63]. At neutral pH the alkaline cathodic reaction is more dominant than the acidic one. Giving cathodic absorption of oxygen:
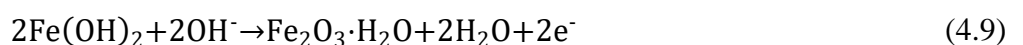
$$O_2+2H_2O+4e^-\leftrightarrow4OH^- \tag{4.6}$$

This is accompanied by the anodic dissolution of iron [63]:

$$Fe \leftrightarrow Fe^{2+}+2e^- \tag{4.7}$$

The primary products react to ferrous hydroxide ($Fe(OH)_2$) by the reaction [63]:

$$2Fe^{2+}+4OH^- \leftrightarrow 2Fe(OH)_2 \tag{4.8}$$

In contact with water, $Fe(OH)_2$ can for instance further oxidise to haematite by the oxidation reaction below [63]:

$$2Fe(OH)_2+2OH^-\rightarrow Fe_2O_3\cdot H_2O+2H_2O+2e^- \tag{4.9}$$

Besides haematite, other forms of iron oxide might emerge on the specimen surface during the autoclave process. In total 16 iron oxides exist, including hydroxides and oxide-hydroxides [64]. They mainly differ in the arrangement of the basic structural units in space, but also in their solubility, colour, structural impurities

as well as their catalytic activity. The identification of the iron oxide on specimens surface is not possible using EDX, due to insensibility to the exact iron-oxygen ratios. Additionally, hydrogen cannot be detected with the EDX device, which further hinders the identification. While the colour of the surface can be an indicator for the form of oxide, the identification by visible inspection is a subjective impression only. This type of identification is inaccurate and hardly reproducible even in a pure state. Anyhow, a comparison of the specimens' surface with a colour scale indicates a mixture of oxide present. Hence, an identification of individual forms of oxide is not feasible and was not conducted. Various techniques exist for further characterisation of the iron oxide, one of which is infrared spectroscopy [64]. It uses the interactions of iron oxides with electromagnetic radiation. An overview of the techniques can be found in the literature [64].

Additionally, a trend can be seen, that the samples exposed to liquid (water/brine) and hydrogen gas show more iron oxide formation, hence higher corrosion rates, than the equivalents exposed to liquid and nitrogen gas. This is in accordance with earlier studies reviewed by Thomas *et al.* [65]. The reviewed studies demonstrate aggravation of corrosion effects for H-charged iron as well as for various types of H-charged steels. The aggravation could be attributed to various effects of the hydrogen onto the steel and its passivation layer. Due to the enrichment of the metal lattice, local phase transformation may occur. Also, various postulations state, that hydrogen could cause a destabilisation of the passive film. While the mechanistic aspects of the destabilisation are not clearly understood yet, various mechanism were proposed. Most commonly, hydrogen is thought to reduce oxygen, the passive film and oxygen-containing species like O_2^- and OH^- within the passive film. Due to these reduction processes the chemical composition of the passive layer changes which alters its electronic properties and its stability. While this theory could explain the increase of corrosion for the untreated samples, the sanded samples don't have a passive layer on the surface sides under investigation. When there is no passive layer on the investigation side, the destabilisation theory cannot be applied and the corrosion intensification requires an alternative explanation. Thomas *et al.* showed that in H-charged steel the hydrogen intrinsically increases the anodic reaction (iron dissolution) [66]. Hence, hydrogen not only destabilise the passive layer but actively promotes corrosion of steel. The observation could be substantiated by an atomistic model indicating weakening of local metallic bonding due to interstitial hydrogen atoms [65]. The combination of the proposed mechanism, passive film destabilisation and promotion of iron dissolution, could alter the chemical composition of the passive film in such a way, that more iron and less oxygen would be present. Such a shift in weight percent cannot be observed in the measured EDX results. However, the experimental set-up has not been designed for the observation of such an effect. The EDX technique might not be sensitive enough for such observations and too many mechanism and reactions come to play in the designed experiment. Hence for verification of such an effect in the studied J55 steel, another experimental set-up would need to be designed for a follow up study. The oxide layer could be characterised by secondary ion mass spectrometry (SIMS), which is a destructive technique to analyse the composition of solid surfaces [67]. A focussed ion beam is used to sputter the surface and ejected secondary ions are detected. Hence the composition of the passive layer could be characterised layer by layer and a depth profile can be received. Alternatively, Mott-Schottky analysis could be used to characterise the semiconductive properties of the passive layer in dependence of the exposure conditions [68]. Although the visible trend in this work cannot be assigned to one of the mentioned postulated theories, hydrogen does seem to aggravate corrosion. Since the trend is not only seen for the untreated samples, but also the sanded samples, this could be an indicator for the promotion of iron dissolution.

The sanded sample in hydrogen gas and brine (Figure 18f), does not follow the trend clearly. In the margin of error, the results for the nitrogen equivalent are the same as for the hydrogen sample. The absolute values are higher than the hydrogen ones. However, it should be noted that only iron and oxygen are shown in the reduced pillar charts. In Figure 20 the complete EDX results are shown. It can be seen, that after the washing process (2 min ultrasonic bath in ultra-pure water followed by 2 min ultrasonic bath in isopropanol), still large quantities of salt components are detected on the hydrogen sample, while only residues of the salt components are detected for the nitrogen sample. Besides the salt components, also Zinc is detected in both specimens, but only for the hydrogen specimen in large quantities. The origin of the Zinc cannot be the brine, as no Zinc components were added in the brine as can be seen in Table 2. A potential origin of the Zinc is the coating which is on the exterior side of the J55 pipe applied. The coating consists of two layers, they were not determined in detail but only categorised using EDX results, the evaluation can be found in Appendix C. The

inner layer was categorised as Zinc-rich paint. Hence, for all J55 specimen, measured Zinc could origin from the coating. For the sanded J55 sample in brine conditions and hydrogen gas, some reaction between hydrogen, brine components and the paint might take place, leading to deposition of Zinc onto the surface. As the weight percentage for the nitrogen sample is much lower, the reaction should depend on the hydrogen gas. Reactions between coatings within the conditions of a salt cavern are not the focus of this work, therefore they will not be discussed further. Anyhow, it should be noted, that a reaction might take place, which can be look into further in future studies. Since weight percent are shown in the pillar charts, for the hydrogen sample the weight percent of iron as well as oxygen are reduced due to the presence of the salt and Zinc on the surface, distorting the charts regarding iron oxide formation. Also, there is a specific penetration depth for the primary electrons causing the element specific X-ray emission. The penetration depth depends on the material and the acceleration voltage. The acceleration voltage was kept constant. When material is deposited on top, two effect arise. Firstly, the material composition on the surface changes potentially leading to a different penetration depth. Secondly, even for a comparable penetration depth, due to additional material on the surface, different amounts of iron from the bulk material is measured. Hence, less of the bulk iron might be measured reducing the percentage of iron but not oxygen.
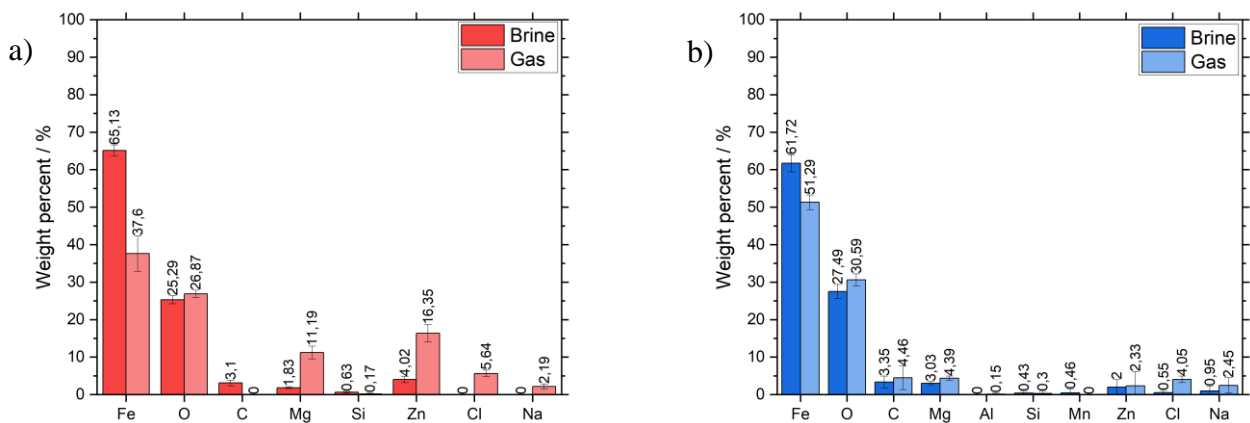
Figure 20: Pillar charts of EDX measurements of sanded J55 sample after autoclave experiment in brine conditions. a) with hydrogen gas and b) with nitrogen gas.

In the pillar charts (Figure 18c-f), the EDX results are shown for the surface previously immersed into liquid (water or brine) and the surface exposed to the pressurised gas. For some specimen the liquid side shows a higher corrosion rate while for others the gas side shows higher corrosion rate. No clear trend can be seen. In an atmospheric environment, most corrosion would be expected close to the interface and above the interface on the gas side, due to the higher oxygen concentration in the air than in water. However, neither the hydrogen gas nor the nitrogen gas contains relevant amounts of oxygen. As discussed, oxygen residues might be present, but these amounts of oxygen are not expected to exceed the concentration within the liquid. Since the specimen are quite small, regarding corrosion aspects the entire surface can be seen as one interfacial area.

The last striking feature in the charts is, that more oxide formation takes place in the brine condition (Figure 18e,f) than in the ultrapure water condition (Figure 18c,d) . The trend is more pronounced for the sanded samples than for the untreated samples. For an understanding of the difference in the corrosion rate between ultrapure water and brine, the effect of salt components on the corrosion require some attention. Multiple salt ions are present in the artificial brine, each affecting the corrosion in a specific way. A few ions and their effects will be discussed here as examples. The effect of three metal ions from the salts (Na^+, Mg^{2+} and Ca^{2+}) on N80 were studied by Lin *et al.* [27]. N80 is another casing steel within the API 5CT classification. The effect of the ion concentrations was measured in relation to the corrosion rate, shown in Figure 21. For sodium a decrease in the corrosion rate was found with increasing ion concentration. The evolution was attributed to reduction of oxygen dissolution caused by the sodium ions. In contrast to sodium, magnesium was shown to increase the corrosion rate radically by acceleration of ion transport in the brine. Calcium showed initially suppression of corrosion with increasing ion concentration. At around 30 wt. % the inflection point of the graph is reached. The dynamic plot is caused by dynamic formation of scale of calcium precipitation. While

Lin *et al* investigated N80, not J55, the same effects can be expected for J55 steel as oxygen dissolution and ion transport depend on the solution not the steel.
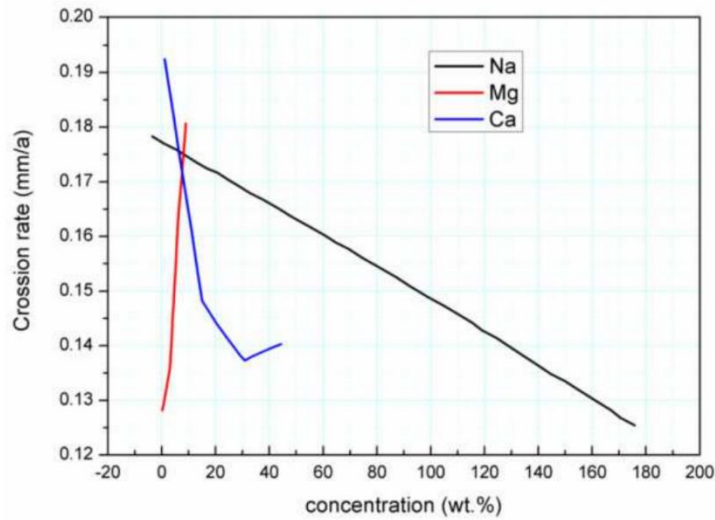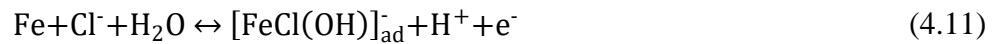

Figure 21: Impact of ions concentration on corrosion rate of Na^+, Mg^{2+}, and Ca^{2+}. Figure is taken from [27].

The effect of chloride concentrations on the corrosion rate in carbon steels was studied by Elfergani and Abdalla [69]. The chloride concentration was regulated by addition of NaCl, leading to an equivalent increase in sodium ions concentration. A maximum in the corrosion rate was found for 3 wt. % NaCl. The maximum can be explained as equilibrium position between the corrosion acceleration of chloride and the corrosion suppression of sodium. Anyhow, the chloride negatively affects the corrosion. On the one hand by its capability to penetrate through the passive layer, leading to destabilisation and localised corrosion attacks. On the other hand, by catalysis of the anodic reaction of iron shown in the equations below [69].

$$Fe+2Cl^-\rightarrow FeCl_2+2e^- \rightarrow Fe^{2+}+2Cl^-+2e^- \qquad (4.10)$$
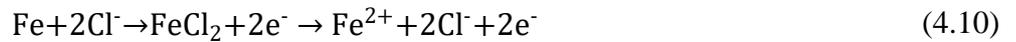
Zhao *et al.* described another potential catalytic mechanism, accelerating the corrosion reaction due to chloride [70]. The reactions are shown below.

$$Fe+Cl^-+H_2O \leftrightarrow [FeCl(OH)]^-_{ad}+H^++e^- \qquad (4.11)$$

$$[FeCl(OH)]^-_{ad} \rightarrow FeClOH+e^- \qquad (4.12)$$

$$FeClOH+H^+ \leftrightarrow Fe^{2+}+Cl^-+H_2O \qquad (4.13)$$

Kasthuri *et al.* [71] studied the impact of chloride in context with capture and storage of CO_2 (CCS). Similar results, initial rise followed by decline in the corrosion rate, were found. While no study was found investigating the effect of chloride on J55, a similar trend is expected since the chemistry of the passive layer as well as the catalytic reaction will be similar. Chloride ions aggravate the corrosion of the specimens. Overall, the chemistry behind the visible increase in oxide formation on the specimen surface is a complex interplay of many mechanisms. While some salt components increase the corrosion, others have decreasing affects like the suppression of oxygen dissolution. Hence, different chemical compositions of brine in various salt caverns might impact the steel differently. The simulated brine from the Jemgum cavern overall show intensification of the corrosion. The allocation of the intensified corrosion to the different ions cannot be undertaken by the experimental setup. For an allocation, the experiment would need to be conducted in solutions with individual ions present.

4.2.1.2 Long-term exposure

For an investigation of long-term exposure of hydrogen on the steel, 14 days experiments were conducted. The EDX results of 3 days and 14 days were compared in the pillar charts below (Figure 22). It is striking that more oxygen is measured after 14 days than after three days in three out of four cases. The untreated dry sample will be seen as an exception as each specimen is an individual sample and the initial values are not known. The decrease in weight percent of iron and increase in weight percent of oxygen lead to the conclusion that more oxide formation could take place in the longer exposure time. However, once the surface is covered with iron oxide and the equilibrium composition is reached, no further change in the weight percent take place. The results suggest, that the maximum weight percent of oxygen could be between 34 to 35 %. However, this assumption would need to be verified, extending the time frame of an experiment to one month, which was not conducted within this work.
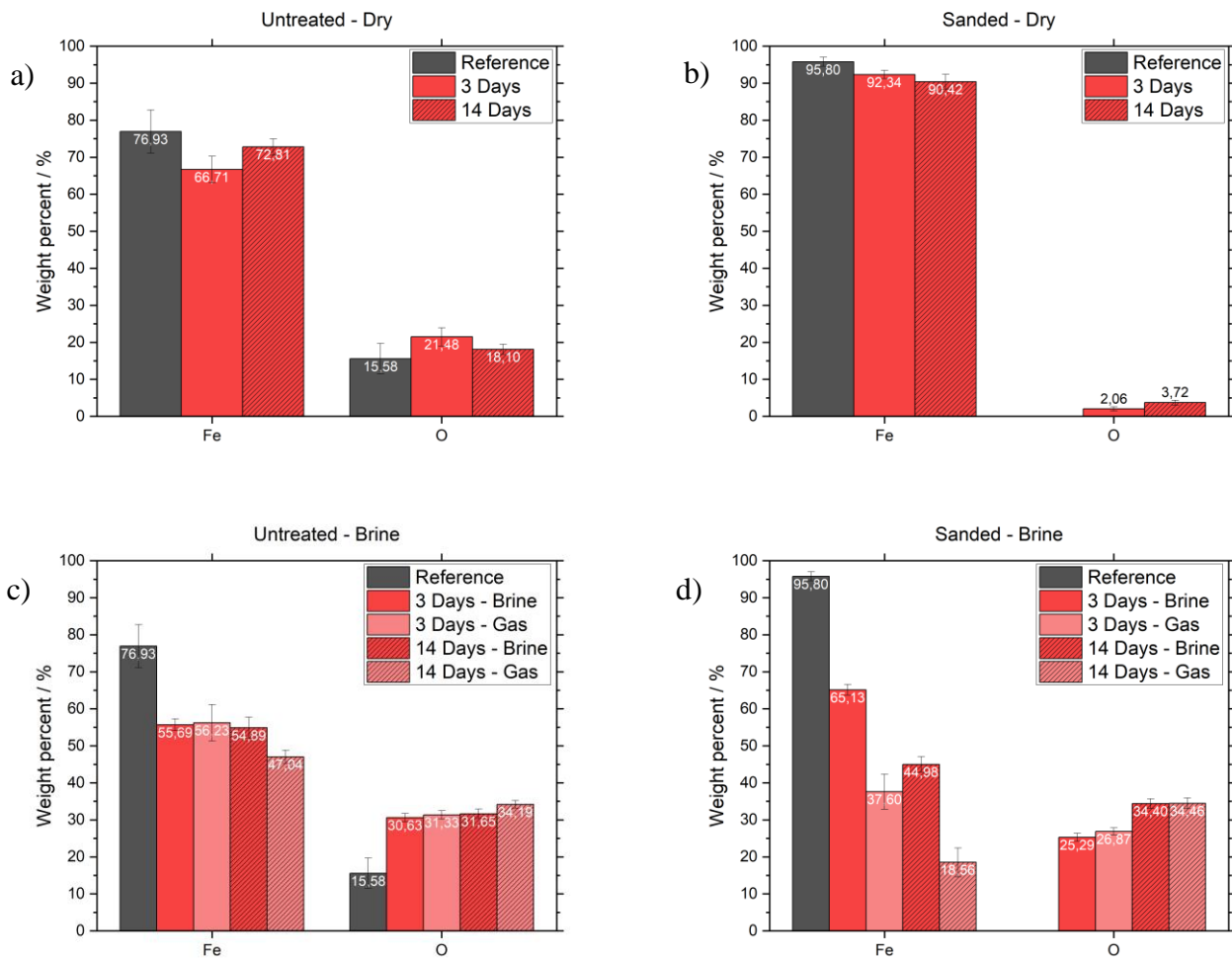
Figure 22: EDX data for Fe and O on J55-samples surface. a) and c) for untreated specimen; b) and d) for sanded specimen. Dry (a, b) and brine (c, d) conditions in H$_2$ atmosphere for 3 days (red) and 14 days (red-hatched) experiments are compared to the reference (grey).

4.2.2 EDX results and discussion of X56

4.2.2.1 Short-term exposure
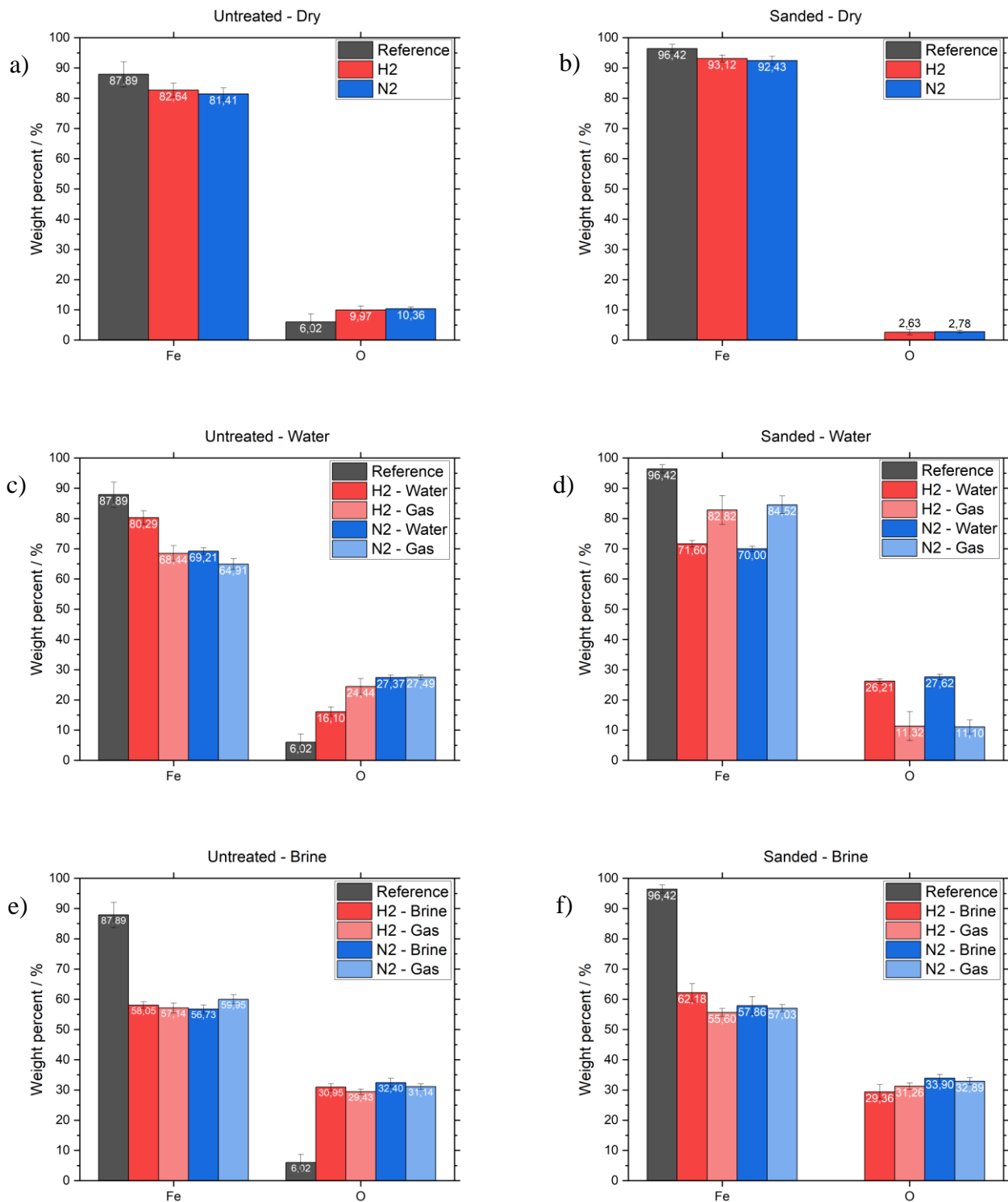
Figure 23: EDX data for Fe and O on X56 samples surface of 3 days experiments. a), c) and e) for untreated specimens and b), d), and f) for sanded specimens. Dry (a, b), ultra-pure water (c, d) and brine (e, f) conditions in H2 (red) and N2 (blue) are compared to reference (grey).

In Figure 23 the EDX data for the 3 days experiments of X56 are shown, for the untreated as well as the sanded steel. Generally, the same trend as in J55 can be seen, that the weight percent of iron decreases due to the chamber experiments while the weight percent of oxygen increases, indicating surface corrosion during the experiments.

For the dry condition (Figure 23a, b) the same observations and their explanation come to play, with small iron oxide formation taking place. Also, like in J55, the hydrogen and the nitrogen sample weight percent match within the margin of error. Suggesting again, corrosion processes potentially caused by oxygen and water residues in the chamber.

Also, like J55, the samples immersed in liquid (Figure 23c-f) show much higher oxygen amounts. While there can be variations within the reactions taking place for different steels, the overall principle does not change. Cathodic absorption of oxygen and anodic dissolution of iron provide the educts for the reaction to form ferrous hydroxide. Further oxidation forms iron oxide on the sample surface. The form of oxide being built on the surface cannot be determined by the used methods in this work.

While there are many similarities between the J55 and X56 EDX results, it is striking that for the X56 steel there is no clear difference between the samples exposed to hydrogen gas or nitrogen gas present. This is the most important difference which can be extracted from the pillar charts. It suggests that hydrogen does not affect the corrosion process of the specific steel X56, hence the steel has higher resistance against hydrogen. A clear allocation of the effect to the steel property cannot be conducted based on the generated samples and their characterisation. Especially since barely any information on the steel is available. However, some information for a similar steel the H_2-ready X52 by Mannesmann Line Pipe GmbH are available from a company's internal study [42]. As mentioned in the theory section, the H_2-ready X52 production route lead to grain refinement and homogenisation of the material. Also, the usage of lower phosphorus and sulphur content in the alloy reduces the impurities and hence the attack points for hydrogen atoms. The microstructural imaging conducted for J55 and X56 (4.1 Microstructural Characterisation of Steels) indicates finer grains for X56 than the J55 steel. Also, only isolated pearlite grains are visible in X56 (Figure 17) while in J55 a clear mix of ferrite and pearlite grains exists (Figure 16). While the study by Brauer *et al.* [42] compared X52 steel of different production routes within one steel classification, the argument can be hold when comparing J55 and X56 in this work. Comparing the microstructural images finer grains and a more homogeneous microstructure is present in X56. The changes in the material characteristics reduces the trap spots for hydrogen inside the material. As discussed for the J55 steel, it was postulated that trapped hydrogen increases the probability for iron dissolution since the metallic bond strength close to the trapped hydrogen is reduced. As an increase in iron dissolution intensify corrosion effects, trapping of hydrogen could directly be related to increased corrosion. When the materials treatment reduces the trapping possibilities for hydrogen, consequently it also reduces the aggravating effect of hydrogen on the corrosion. While there is no clear difference between the samples exposed to hydrogen and the nitrogen equivalents, it cannot be excluded that the hydrogen has some impact on the corrosion which is not visible within the sensitivity of the characterisation method used.

In the EDX results the untreated-water conditioned samples (Figure 23c) stand out and do not show nearly identical values for the hydrogen and nitrogen sample. But, also in this condition, the oxygen weight percentage of the hydrogen sample does not exceed the weight percentage for the nitrogen sample. This is opposite to the trend seen for J55, which was indicating a raised corrosion effect induced by hydrogen. Rather than indicating a trend or even an effect of hydrogen, it can be seen as artefact from the experiment set-up. As mentioned for other specimens earlier, each result is one individual specimen and might have varying initial conditions. Hence, the result for this specimen will be seen as an exception.

4.2.2.2 Long-term exposure
The EDX results of the 2-weeks experiments of X56 are shown in Figure 24. No significant difference to the long-term exposure results of J55 can be noticed. The maximum value of 34.62 % oxygen in Figure 24c agrees with the suggestion of 34-35 % being the equilibrium percentage for complete surface coverage with iron oxide.

One striking aspect is visible in Figure 24a. Similar to the result in the same conditions but with J55 steel, the results indicate less iron oxide formation after 14 days than after 3 days. As discussed earlier, this could be caused by the testing conditions, of each results origin being one specimen only. Yet, since the effect is visible in the exact same conditions for both steels, the result cannot simply be called a coincidence. Critical thinking

and revision are urgently required to confirm the result being accidental or an actual effect. For this purpose, at least a repetition of the 4 specimens under discussion will be required. Alternatively, another test-set up should be established.
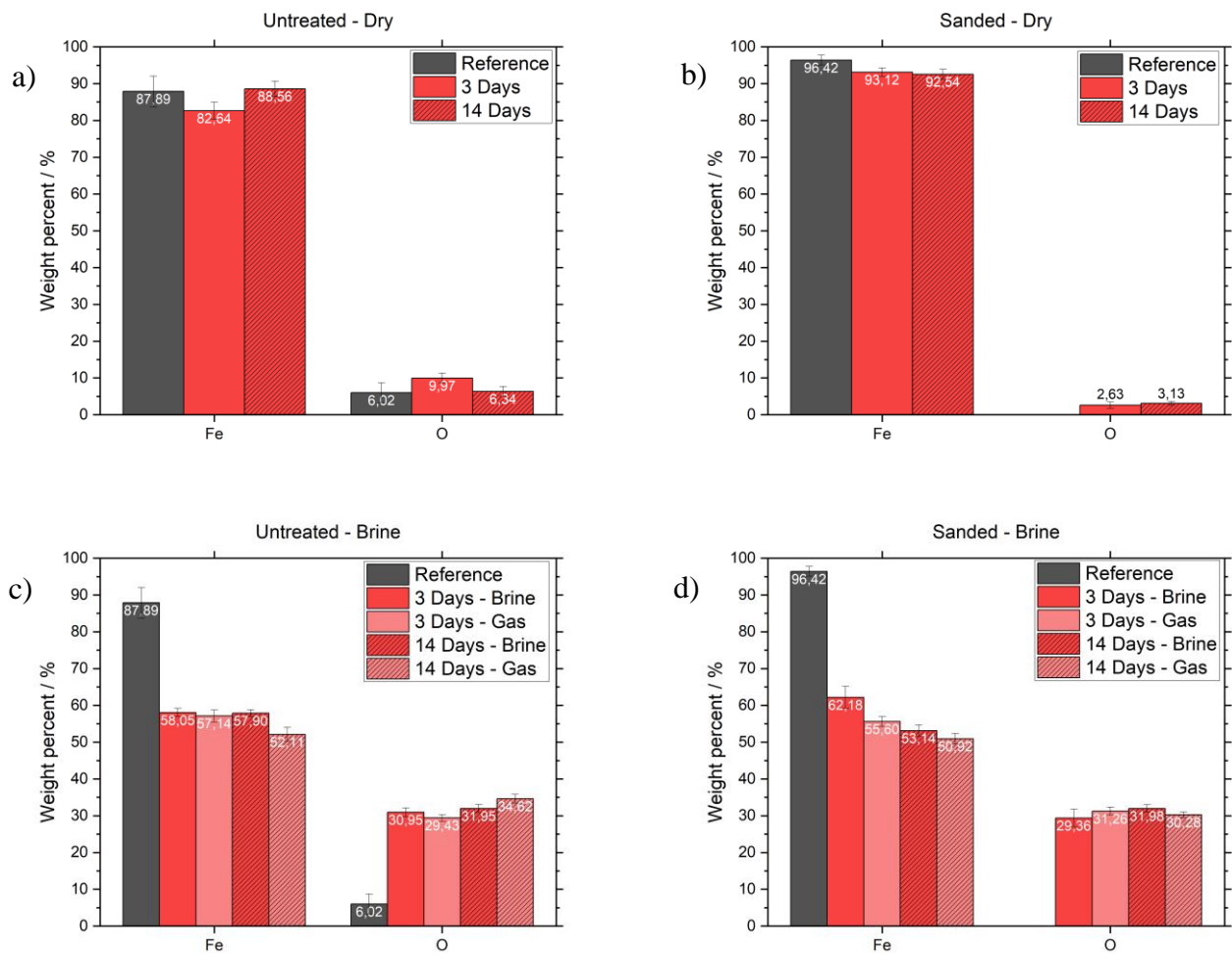

Figure 24: EDX data for Fe and O on X56 samples surface. a) and c) for untreated specimens; b) and d) for sanded specimens. Dry (a, b) and brine (c, d) conditions in H2 atmosphere for 3 days (red) and 14 days (red-hatched) experiments are compared to the reference (grey).

4.3 Scanning electron microscopy characterisation of steels

In this subsection, SEM results are presented. The SEM is a microscopic characterisation technique. It was chosen, as the used SEM system allows a resolution of 1.1 nm at 20 kV and 2.5 nm at 1 kV acceleration voltage [72]. Due to the high resolution, small surface features like surface cracks can be recorded. Even hairline fractures are visible. The results are the combination of SEM images as well as observations during the characterisation procedure. Especially the occurrence of surface cracking is of great interest. As described in 2.4 , there are multiple mechanisms of crack formation.

4.3.1 Surface cracks – J55

In this subsection, SEM images of surface cracks will be shown and the trends of crack formation will be discussed. The keypoints of observations during the characterisation procedure are summarized in Table 3 for untreated J55 samples and in Table 4 for sanded J55 samples. The observations on the crack occurrence frequency were categorised in 5 categories. The categories are: 1) not obvious, no cracks or only hairline fractures are found after intensive surface investigation; 2) occasionally present, cracks can be found on surface, but are hard to find; 3) multiple locations, cracks can be found when scanning over the surface; 4) regularly present, cracks are easy to find when scanning over the surface and 5) all over surface, cracks are all over surface, there is no need to search or scan.

Table 3: Summary of observations on occurrence frequency of surface cracks on the untreated J55 specimen.

	Hydrogen		Nitrogen	
Dry	3) Multiple locations		2) Occasionally present	
Ultrapure water (20 mL)	Water: Gas:	4) Regularly present 2) Occasionally present	Water: Gas:	3) Multiple locations 2) occasionally present
Artificial brine (20 mL)	Brine/Gas:	5) All over surface	Brine: Gas:	4) Regularly present 3) multiple locations

Table 4: Summary of observations on occurrence frequency of surface cracks on the sanded J55 specimen.

	Hydrogen		Nitrogen	
Dry	1) Not obvious		1) Not obvious	
Ultrapure water (20 mL)	Water/Gas:	4) Regularly present	Water/Gas: 1) Not obvious	
Artificial brine (20 mL)	Brine/Gas:	5) All over surface	Brine: Gas:	4) Regularly present 2) occasionally present

In general, it has to be noted that an assignment of cracks to a specific cracking mechanism is difficult to make. Especially since only visible features and EDX data are used for the characterisation. However, the potential mechanism will be discussed based on literature descriptions of morphology features and the knowledge about the autoclave conditions. Nevertheless, the purpose of this work is to find trends in surface features emerging from salt cavern conditions rather than clear allocations to underlying mechanism. As mentioned (2.4 Mechanism of crack formation) multiple potential cracking methods exist, for instance corrosion fatigue (CF) or multiple types of environmentally induced cracking (EIC) such as stress corrosion cracking (SCC), hydrogen-induced cracking (HIC), sulphide stress cracking (SSC) and stress-oriented hydrogen-induced cracking (SOHIC). More cracking mechanism exist but will not be discussed in this work.

Starting with the least aggressive environment (dry-N_2 conditions), in the sanded condition, with no oxide film present, no cracking could be found. In untreated condition, only occasional cracking was found in oxide structures on the surface. While general fatigue is most probably not the overall reason behind cracking in all test conditions, as more cracking would have been found in this sample in that case, it might be the cause in dry-N2 for cracking in the oxide structures. An example crack can be seen in Figure 25.
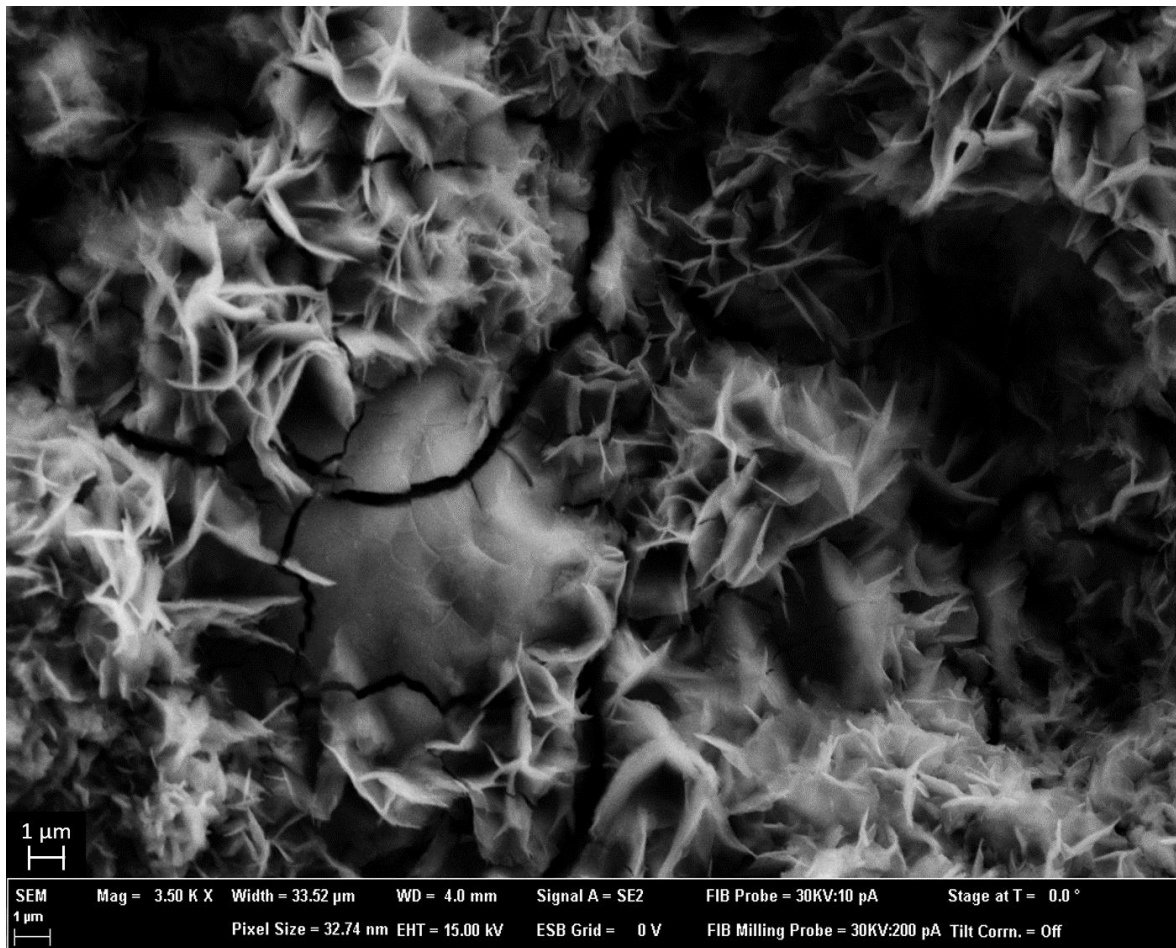
Figure 25: Crack in oxide structure on surface of a J55 specimen after 3 days in an autoclave with pressure/temperature cycling and nitrogen gas (purity 6.0).

In more corrosive environments, the cracking is more pronounced. This can be seen in Table 3 and Table 4 in all columns, as the frequency category number rises from dry to brine conditions. The cracking is branched and has less oxide in the cracks than in the surroundings. Yet some oxygen can be measured with the EDX in the cracks themselves. The cracked surface overall show oxidation as was seen previously (4.2 Energy dispersive X-ray spectroscopy characterisation of steels). Based on the testing, an allocation can only be done by the surface data. SCC shows a striking feature of low corrosion on the stress corrosion face even in a corrosive solution [50]. Based on the EDX data presented earlier, this distinguishable feature does not apply. Only the extensive branching can be observed. Nevertheless, SCC seem not to be applicable as main cracking mode. HIC regularly shows straight cracking without branching, which is not observed. Additionally, cracking in nitrogen gas is observed as well as in hydrogen gas, which rules out HIC and SOHIC as main cracking mechanism. SSC is a special type of HIC and can only be applied in hydrogen sulphide environment.

While the environmentally induced cracking methods seem not to be applicable as main cracking mechanism, corrosion fatigue potentially could be the cause of the cracking. Corrosion fatigue combines a corrosive environment, like water or brine, with cycled stresses, which could be caused by the temperature and pressure cycles. Characteristics are corrosion products within the cracks as well as barely any branching [50]. Additionally, the crack initiation often starts in localised surface features like pits. While there is less oxygen found within the cracks than the surrounding, EDX results still suggest the presence of some corrosion products. Also, cracking often starts in pit-like structures or local oxide particles on the surface, which agrees to CF. However, branching is visible in the cracking structure. As mentioned, more than one cracking mechanism tend to occur simultaneously, which complicates interpretation. From the testing conditions and some visible features, corrosion fatigue probably plays a major role in the cracking of the steel specimen. CF also potentially explains the trend of increasing cracking frequency from water to brine conditions, since the brine provides a harsher corrosive environment. Meaning that more localised corrosion attacks take place in the brine condition due to the salt ions and localised corrosion provides initiation points for CF. The branching

could indicate some influence of SCC. A clear allocation is not possible based on the characterisation methods. The surface of a sanded sample which was exposed to brine and hydrogen gas for 3 days is shown in Figure 26a. The initiation of cracks in local corrosion features on the surface can be seen. In Figure 26b the comparison for the same conditions but 14 days exposure clearly shows the branching of cracks.

Comparing specimens in environments with N_2 exposure to H_2 exposure, an increase in the cracking frequency can be observed. In Figure 27 the surface cracking can be compared. The untreated-brine condition has been chosen for the comparison since cracking can easily be seen on those surfaces. In a) the surface of a specimen exposed to hydrogen gas is shown, it can be seen that cracking takes place in a large area and is less restricted to one specific surface feature. With close attention even more cracking areas can be found. The surface of a specimen exposed to nitrogen gas is shown in b). Less cracking can be found and the cracking specifically takes place in an individual oxide structure. These results suggest some impact of hydrogen on the J55 steel. As mentioned (2.4 , different cracking methods can appear simultaneously, in which case the morphology of one cracking method can be dominate [50]. The morphology of HIC is regularly sharp without extensive branching. Yet, the morphology might be dominant from fatigue cracking or corrosion fatigue cracking, possibly combined with SCC, while also HIC or hydrogen-assisted cracking (HAC) is present. Hydrogen atoms might be absorbed and clustered in the crack tip, accelerating further cracking. The exact mechanism of hydrogen embrittlement is not known, but multiple theories exist (2.3.1 Hydrogen Embrittlement). In the HEDE theory, crack propagation and acceleration are explained by reduced bonding energy of the lattice caused by hydrogen atom agglomeration at the crack tip [29]. This provides a potential explanation for the increase of the crack formation in hydrogen atmosphere. It should be noted, that the exposure to hydrogen gas also led to intensification of corrosion effects in J55, which potentially increases the initiation points for cracking, hence an increased cracking frequency.

Another trend can be seen comparing the results of untreated (Table 3) and sanded specimens (Table 4). In dry conditions, the sanded specimens do not show cracking, whereas in untreated cuboids, cracks can already be found. In the brine condition, both pre-treatments show cracks all over the surface. These results support, that cracking is initiated in local oxide formations on the surface. Further, the results suggest that the crack initiation is delayed in the sanded specimen. The sanding was conducted to accelerate aging processes; hence the results are unexpected. The effect can be explained by the removal of the oxide from the surface. For the untreated sample the surface is covered with iron oxide from the beginning, therefore crack initiation in oxide features could take place in every condition directly. At the sanded sample surface, oxide features need to form on the surface first, before crack initiation in the features can take place. Especially in dry conditions, the oxide formation on the surface is slow. After three days no large oxide structures are formed on the surface. This difference might lead to the delay.

It has to be noted, that for untreated samples larger cracks might be in the oxide structures only. The microstructural imaging does not provide information whether the steel itself is affected as well. For sanded specimens after 14 days in hydrogen gas and brine, the image clearly shows cracking of the steel surface itself. In Figure 28 SEM images of an untreated (a) and a sanded (b) specimen after 14 days in hydrogen gas and brine is shown and can be compared.

For all conditions, more cracking was found after 14 days than after 3 days. The results are shown in Table 5. It can be seen, that in all conditions the same or a higher category is reached after 14 days, indicating further material degradation with time. It is important to note, that the frequency categories do not provide information on the size of the crack. For instance, after 3 days in sanded-brine conditions, cracks can already be found all over the surface. As this is the highest category, after 14 days no aggravation is apparent in the table. Nevertheless, there is a tremendous difference visible in the SEM images. After 14 days the cracks grow through the entire surface, which was not the case after 3 days yet. The comparison can be seen in Figure 26. To conclude, with time the cracks grow and more crack initiation takes place. Hence, the material suffers with longer exposition to the salt cavern conditions.

Table 5: Summary of observations on occurrence frequency of surface cracks on J55 specimens comparing 3 days to 14 days autoclave experiments.

	3 Days		14 Days	
Untreated - Dry		3) Multiple locations		4) Regularly present
Untreated - Brine	Brine/Gas:	5) All over surface	Brine/Gas:	5) All over surface
Sanded - Dry		1) Not obvious		4) Regularly present
Sanded - Brine	Brine/Gas:	5) All over surface	Brine: Gas:	5) All over surface - covered by salt
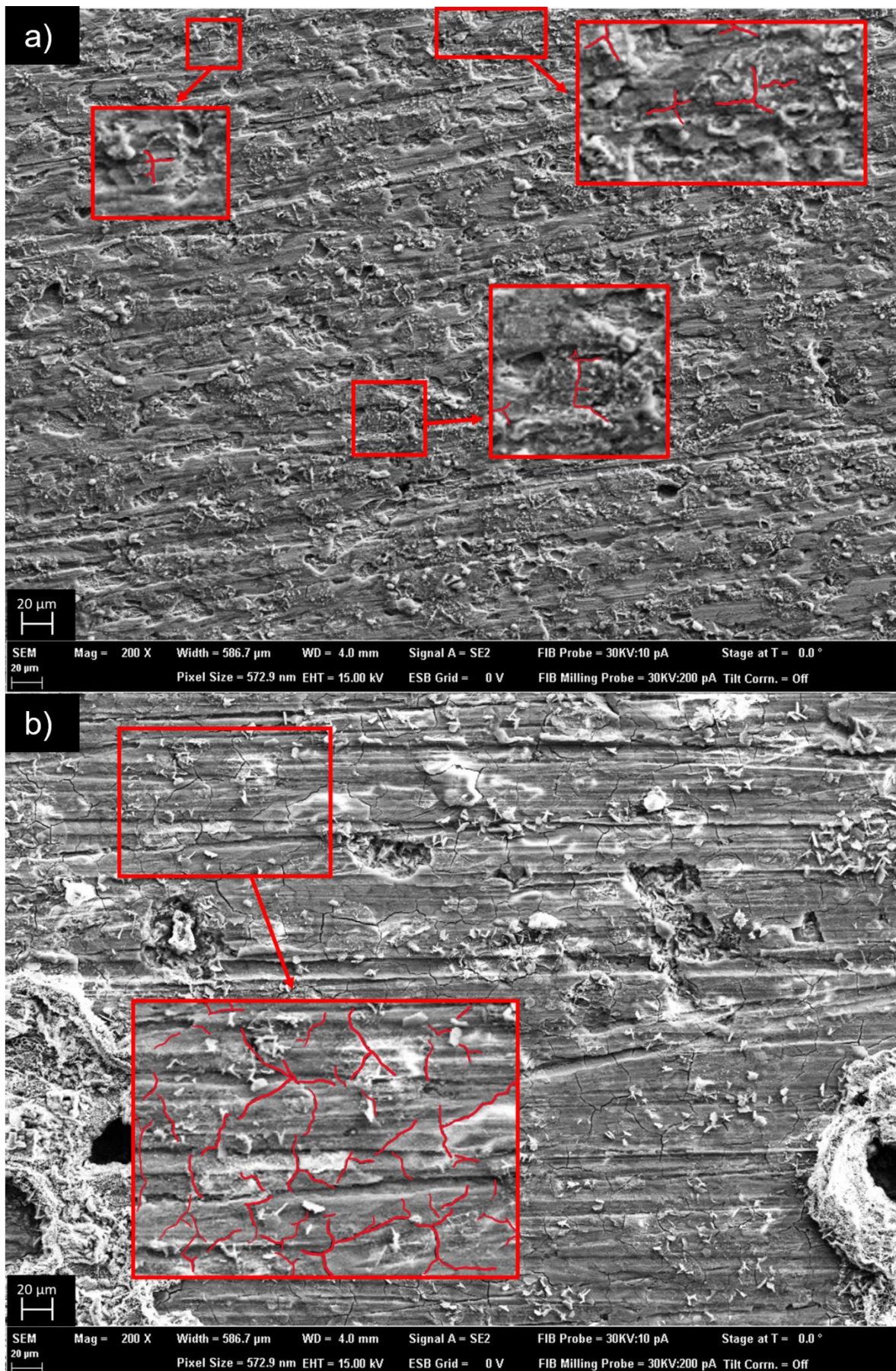
Figure 26: Cracks on the surface of sanded J55 specimens a) after 3 days and b) after 14 days in an autoclave with pressure/temperature cycling, 20 mL brine and hydrogen gas (purity 6.0). The figures show the side exposed to the brine. The red marked area has been magnified and cracks within the area are marked in red.
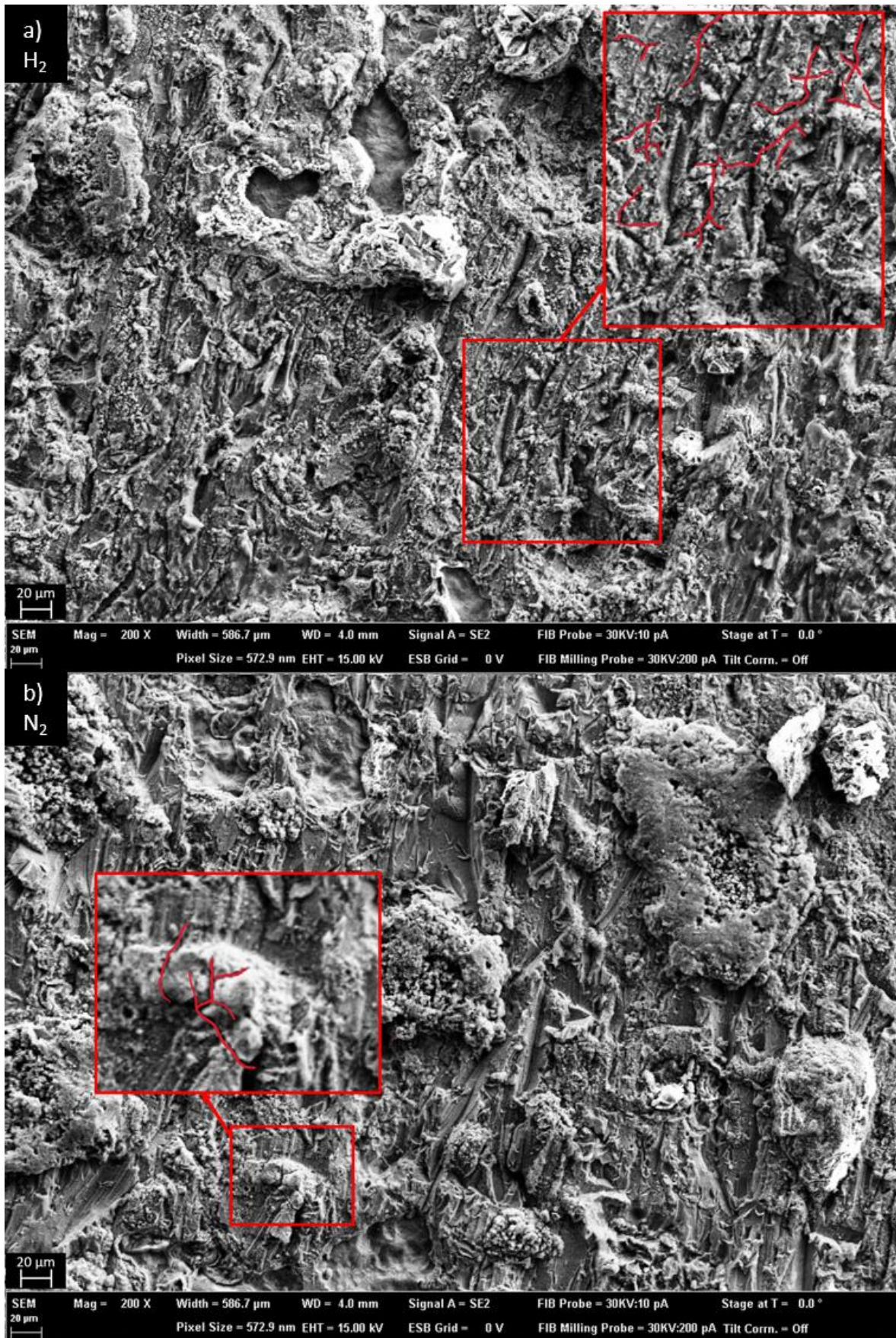
Figure 27: Cracks on the surface of an untreated J55 specimen after 3 days in an autoclave with pressure/temperature cycling, 20 mL brine and a) hydrogen gas (purity 6.0) or b) nitrogen gas (purity 6.0). The figures show the side exposed to the gas directly. The red marked area has been magnified and cracks within the area are marked in red.
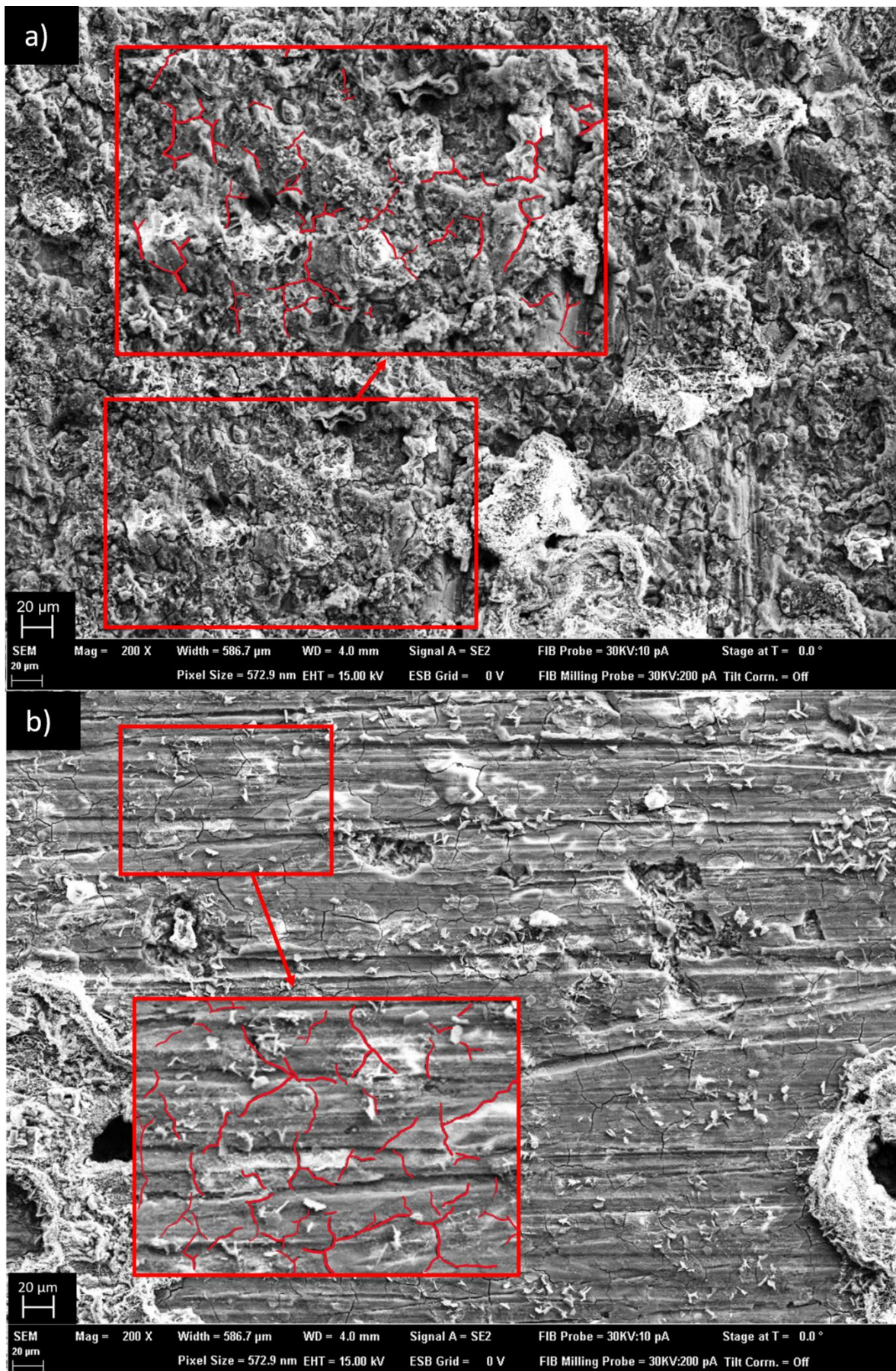
Figure 28: Cracks on the surface of J55 specimens in a) untreated state and b) sanded state after 14 days in an autoclave with pressure/temperature cycling, 20 mL brine and hydrogen gas (purity 6.0). The figures show the side exposed to the brine. The red marked area has been magnified and cracks within the area are marked in red.

4.3.2 Surface cracks – X56

The key points of observations during the characterisation procedure are summarised in Table 6 for untreated X56 samples and in Table 7 for sanded X56 samples. The same cracking frequency categorisation as for J55 is used.

Table 6: Summary of observations on occurrence frequency of surface cracks on untreated X56 specimens.

	Hydrogen	Nitrogen
Dry	4) Regularly present	2) Occasionally present
Ultrapure water (20 mL)	Water/Gas: 1) not obvious	Water/Gas: 1) not obvious
Artificial brine (20 mL)	Brine/Gas: 4) Regularly present	Brine/Gas: 4) Regularly present

Table 7: Summary of observations on occurrence frequency of surface cracks on sanded X56 specimens.

	Hydrogen	Nitrogen
Dry	1) not obvious	1) not obvious
Ultrapure water (20 mL)	Water/Gas: 1) not obvious	Water/Gas: 1) not obvious
Artificial brine (20 mL)	Brine: 4) Regularly present Gas: 3) multiple locations	Brine: 4) Regularly present Gas: 3) multiple locations

There is a clear difference of the X56 frequency of surface cracks compared to the J55 results. It is striking, that in general less cracking occurred, indicating a better resistance again the salt cavern conditions. This is shown in the specimen exposed to hydrogen gas but also in the specimen exposed to nitrogen gas, suggesting a better overall resistance against the temperature and pressure cycling as well as against moisture. Even in the brine condition less cracking was observed, but the salt ions seem to significantly decrease the resistance of the steel. This could be caused by the ability of localised corrosion, producing stress concentration points and consequently initiation points for cracking. In the CF mechanism local corrosion points, such as pits, often serve as initiation point [50]. As two different steel types are compared and no detailed information on these are available, reasoning on the origin of the improved resistance is difficult. Yet, the production route and the chemical composition are the major player. As mentioned, the used X56 fulfils the strength requirements for a J55 classification, hence the small variation in the strength is likely to be negligible.

Also, it is noticeable that in contrast to the J55 specimen there is no clear overall difference in cracking frequency between X56 specimen exposed to hydrogen gas or nitrogen gas. As described earlier, the microstructure of the steel affects the hydrogen diffusivity. Homogenisation is shown to reduce the negative effects of hydrogen [42]. In 4.1 Microstructural Characterisation of Steels, the microstructure of both steels was determined and X56 shows a finer more homogeneous grain structure than J55. As trapped hydrogen can cause a reduction in bonding strength and resulting crack acceleration when hydrogen aggregates at the crack tip (HEDE model), hydrogen trapping prevention is of significance importance. As the results clearly show no effect of the hydrogen, HIC and HAC as well as SOHIC does not take place.

Another trend which was visible for J55 was the difference in cracking between untreated and sanded specimens; in X56 the trend is not as pronounce. The sanding, which was conducted partly as ageing accelerator did not seem to result in the desired effect. While internal effects due to a potential increase in hydrogen uptake cannot be seen by the conducted characterisation techniques, the surface does not prove the sanding to accelerate the aging. It is striking, that for untreated-dry specimens (Table 6, first row) cracks were found on the surface, while in the more extreme conditions including water, no cracks are visible. These results support the results from the J55 specimens, that general fatigue could take place in the dry conditions for the oxide features. In the water condition, the kinetics of oxide formation seem to be faster than the cracking, therefore no cracks could be found. Additionally, for this condition (untreated-dry), a different cracking frequency was found for the two gases. However, as this is not the case for the other conditions, it needs to be confirmed by repetition of the untreated-dry experiment. Without confirmation it could be coincidental, rather

than an effect. While in the untreated sample cracks are found in the dry conditions, this is not the case for sanded specimens. Only the dry conditions show a difference between the two material states (untreated/sanded). It can be explained with the cracks initiate in oxide structures, as these are not present in the sanded specimen from the beginning. Even after 3 days no large oxide features can be found, which can be seen in Figure 29.
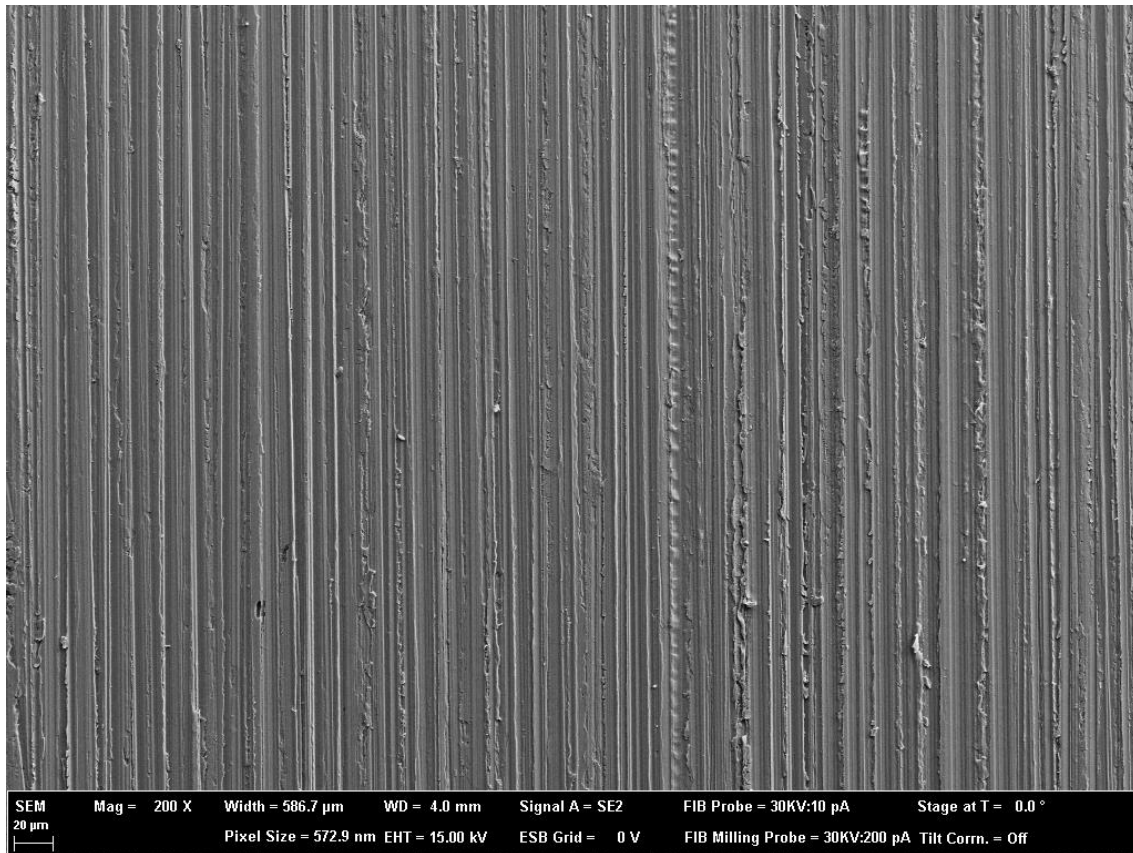

Figure 29: Surface of sanded X56 steel sample after 3 days in autoclave with hydrogen gas (purity 6.0) in dry conditions.

Comparing 3 days and 14 days exposure to hydrogen gas in dry and brine conditions, the results shown in Table 8 indicate barely any increase in cracking frequency with time. In addition, also the crack size barely changes which can be seen in Figure 30 suggesting a good resistance against the salt cavern conditions. It can also be seen, that a close to uniform oxide film was built. Iron oxide can serve as natural protection layer when uniform corrosion takes place on the surface.

Table 8: Summary of observations on occurrence frequency of surface cracks on X56 specimens comparing 3 days to 14 days autoclave experiments.

	3 Days		14 Days	
Untreated - Dry	4) Regularly present		5) All over surface	
Untreated - Brine	Brine/Gas:	4) Regularly present	Brine: Gas:	3) Multiple locations 5) all over surface
Sanded - Dry	1) Not obvious		1) Not obvious	
Sanded - Brine	Brine: Gas:	4) Regularly present 3) multiple locations	Brine: Gas:	4) Regularly present 2) Occasionally present
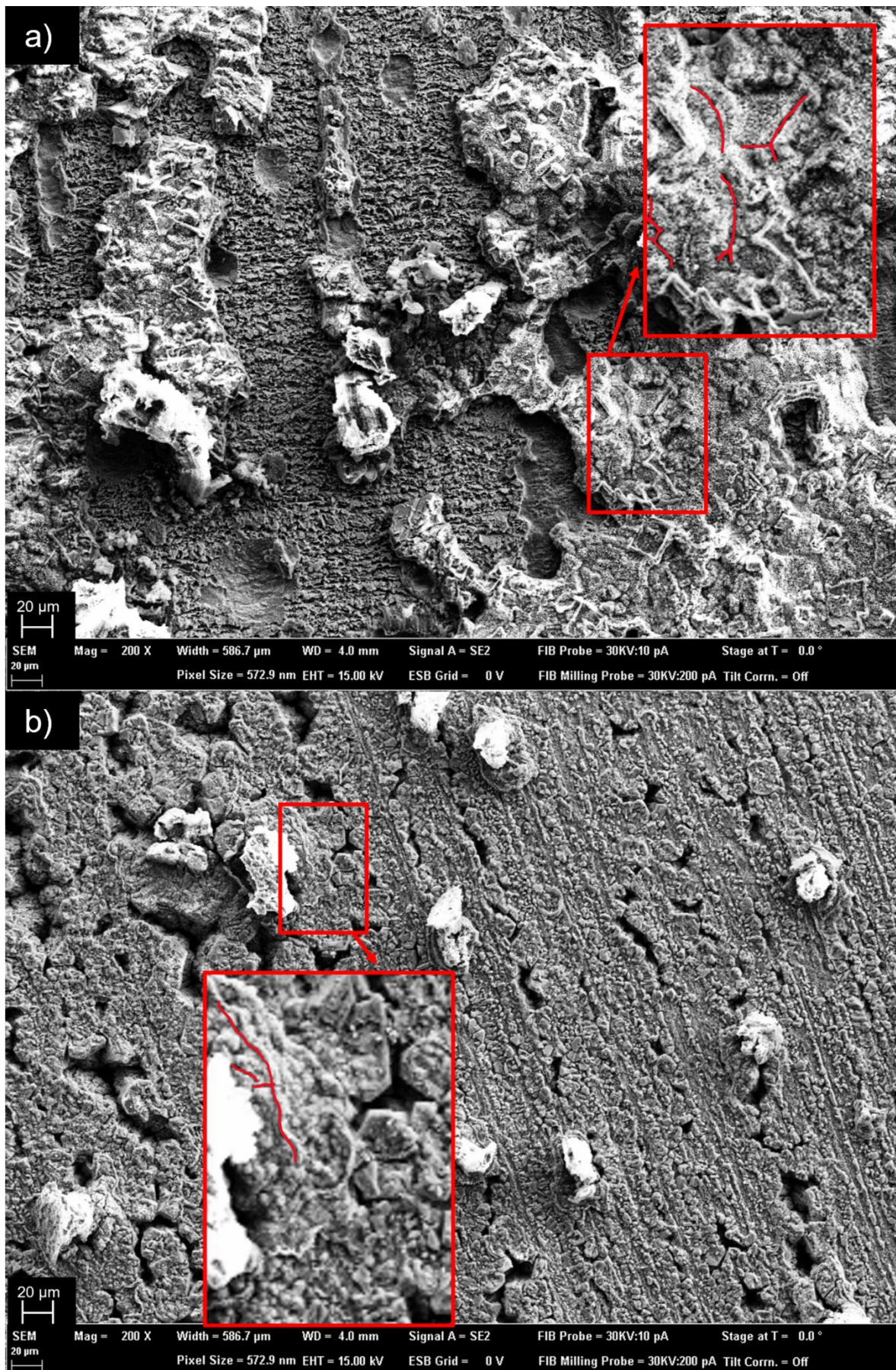
Figure 30: Cracks on the surface of a sanded X56 specimens a) after 3 days and b) after 14 days in an autoclave with pressure/temperature cycling, 20 mL brine and hydrogen gas (6.0). The figures show the side exposed to the brine. The red marked area has been magnified and cracks within the area are marked in red.

4.4 Impact of hydrogen sulphide on J55

In 2.2.3 Impurities it was described, that hydrogen sulphide (H_2S) might emerge in a salt cavern during hydrogen storage, as sulphate-reducing bacteria catalyse a reaction of sulphate with hydrogen (Eq. 2.3). H_2S is known to have intensification effects on hydrogen embrittlement, as it suppresses the re-formation of hydrogen molecules on the metal surface. Hydrogen atom uptake is therefore increased. The state-of-the-art literature showed the effect as for instance the steel P110 demonstrate a hydrogen uptake one magnitude larger than with pure hydrogen and steel failure within 10 min [48]. Hence, an exposition to H_2 with H_2S impurities needs to be conducted to test the impact of H_2S.

One test was conducted, as an outlook for future experiments, with sanded J55 steel, exposed for 2 weeks to hydrogen gas (6.0 purity) with 40 Mol-ppm H_2S in dry chamber conditions. The sample was characterised using SEM and EDX. The EDX results are shown in Figure 31. In Figure 31a the results are compared to the reference values (grey) and to exposure in the same conditions to pure hydrogen (red). It can be seen, that more oxygen is detected on the surface and the iron values are significantly reduced. In Figure 31b the reduced iron values could be explained by surface coverage with sulphur. The origin of the high oxygen values remains unclear, but the results evidently indicate an impact of H_2S which should be tested. The SEM results can be seen in Figure 32, only fine cracks can be found on the surface. The occurrence frequency was categorised to "3) multiple locations", which is less often than in pure hydrogen gas (category 4). This result is surprising as more crack formation due to the addition of H_2S gas was expected. The EAC mechanism includes one mechanism of crack formation called sulphide stress cracking, which was expected to take place. It is likely, that sulphur on the surface covers cracks. However, it is also possible, that J55 has a higher resistance against H_2S than expected. More testing is required to allow for well-founded statements. A potential test series could include the exposure to gas with varying hydrogen sulphide amounts. The lower impurity content is expected to decrease the surface coverage. Hence, coverage of cracking could be confirmed or excluded. Also, the gas should be tested in a chamber with water and brine as well, as these data could be compared with the data in this work.
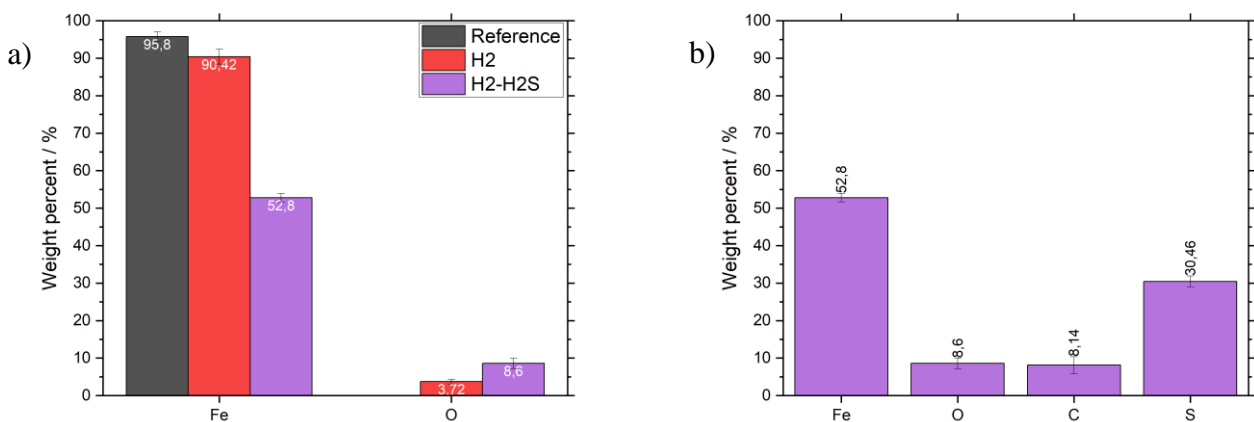
Figure 31: a) Reduced pillar chart of EDX results comparing the reference (grey chart) with 2 weeks exposure of sanded J55 in a dry chamber with H_2 (6.0 purity) (red chart) and with H_2-H_2S (6.0 purity with 40 Mol-ppm H_2S) (purple chart). b) Extended EDX pillar chart of sanded J55 specimen after 2 weeks exposure to H_2-H_2S in a dry chamber.
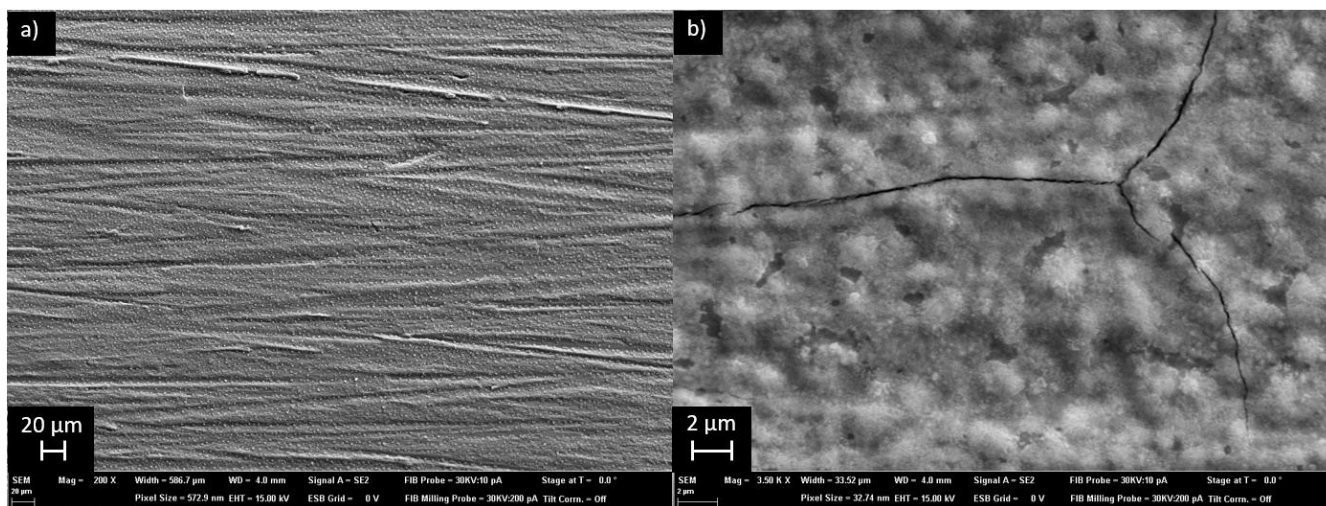
Figure 32: SEM images of sanded J55 specimen 2 weeks exposed to H₂-H₂S gas (6.0 purity with 40 Mol-ppm H₂S) in a dry chamber. a) overview image at 200X and b) image of crack at 3500X magnification.

5. Discussion

5.1 Test set-up

In this work, two type of steels (J55 and X56) were tested on their resistance against UHS salt cavern boundary conditions. For this purpose, the steel samples were exposed to hydrogen gas in dry, ultra-pure water and brine conditions in an autoclave for three days. Simultaneously another specimen was tested in the same conditions with nitrogen gas exposure. Testing series were done with both, steels with untreated and sanded surface. Hydrogen gas exposure in dry and brine conditions for 14 days was conducted to investigate the effect of longer exposition times. The impact of all conditions was characterised using SEM and EDX techniques.

The study was conducted using one specimen only per testing conditions. As seen in the previous parts, this choice led to some uncertainties in the EDX results. While the overall trends are clearly visible, individual results strike since they are clearly higher or lower than expected compared to the reference and the visible trends. It can be explained by the test set-up. Since the SEM sample holder used for characterisation requires carbon tape to stick the sample onto the holder, each specimen can only be characterised after the autoclave procedure, meaning the actual initial values of a specimen are not known. To counteract an imbalance in the initial values for various specimen, the reference values were averaged over three specimens. Leading to a mean value to compare the results to, but with a high margin of error. This is caused by the origin of the pieces. The specimen pieces were cut out of a pipe for a real cavern, hence its state is not new but with natural change of the surface and with dirt of the storage period. Therefore, while all pieces are similar since they originate from one pipe and were stored as large pipe, no piece is exactly like the others, especially in the untreated state. As the goal in this work was to find trends, the discrepancies do not negatively impact the evaluation process. Nevertheless, it is necessary to acknowledge that individual results need to be verified and particularly flashy results should be repeated.

Particularly noticeable are the results comparing the short-term to long-term exposure for both untreated steels, shown in Figure 33. The results suggest for both steels more oxide formation after 3 days than after 14 days, which is contrary to the expectations. While these results are against the trend seen in the other testing conditions and are hard to explain reasonable, it cannot be ruled out, that an actual affect can be seen. For verification an improvement in the test set-up could be established by usage of a specific SEM-specimen holder for large specimens. There are specimen holders which do not require taping the specimen, but make use of screws holding the specimen in its place. The usage of such a specimen holder would allow one individual specimen to be characterised after multiple time periods. Meaning, one steel cuboid could provide results before its exposure (reference), after 3 days and after 14 days with interrupted exposure to the conditions within the autoclave. Consequently, the margin of error could be drastically reduced and insecurities about results prevented. In this set-up the side of investigation should be marked, to rule out the observation of

scratches potentially originating from the holder screws. It should also be noted, that destructive characterisation techniques, like microstructural imaging with the SEM, will only be possible after the last exposure.
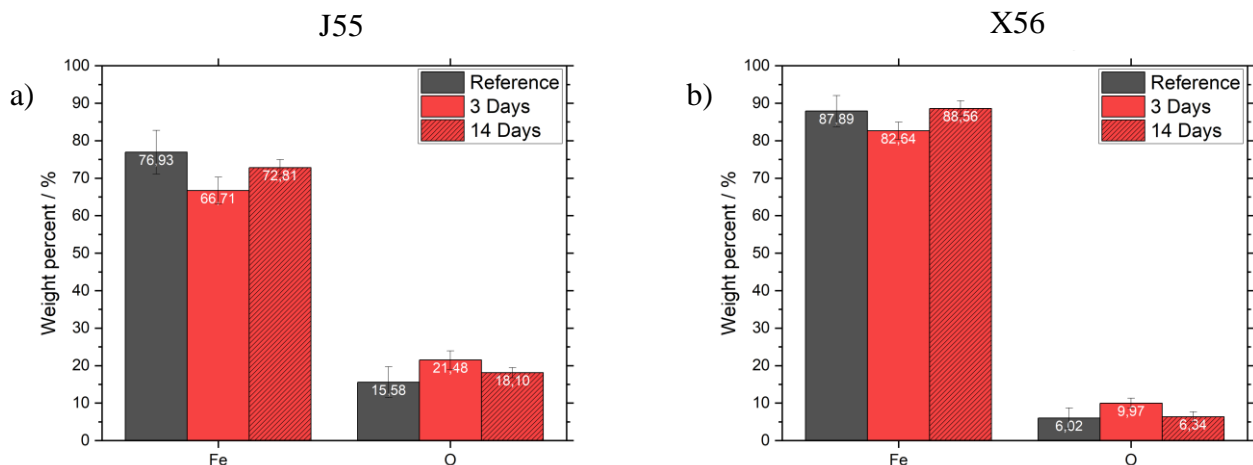

Figure 33: EDX results of a) J55 steel and b) X56 steel of experiments conducted with untreated samples in dry pressurised hydrogen gas (purity 6.0). Comparing the results of the experiment for 3 days (red) and 14 days (red-hatched) experiments with the reference (grey).

Another aspect of the experiment design is the aging acceleration. The aging of the specimens was accelerated by multiple ways, including extreme temperature cycling, sanding and direct contact to water or brine. It was not determined how much the taken steps accelerate the aging. The usage of the alternative specimen holder for SEM characterisation allows characterisation after multiple time periods. A test series could be conducted using more time steps than 3 days and 14 days only, documenting the surface changes after each step. Comparing the development with a test series with less acceleration steps could give an indication on the factor. It should be noted, that the high-pressure reactor combine with the thermostat, does not allow automated pressure cycling without the extreme temperature cycling.

5.2 Material specifics

In this work, two specifically provided steels, J55 from EWE GASSPEICHER GmbH and H_2-ready X56 from Mannesmann Line Pipe GmbH were investigated. The aim of the work was to investigate occurring surface changes as well as their trends depending on the applied conditions. The characterisation was conducted by surface methods only which limits the knowledge of the specific material as well as the allocation of features to existing postulations. In this section the consequences need to be discussed.

J55 and X56 are definitions for steel types defined primarily over the material strength. No strict restrictions on the chemical composition of the steels (Figure 45 and Figure 47 in Appendix D) or the microstructure exist. Hence, two specific steels of type J55 (or X56) are not necessarily interchangeable for each application. This can be seen in the example of X52 steel (2.3.2.1 Pipeline steels) in which two X52 samples produced by different production routes and alloying element adjustment show significantly different resistance against hydrogen embrittlement [42]. For this work, it means that the results are not generally valid but specifically for the provided steels. The used materials should be characterised in great detail regarding chemical composition, microstructure and internal stresses. Improvements in the resistance can still be discussed based on literature descriptions, but should be further studied to gain certainty. Various steels from one steel type should be tested with focus on the differences in surface changes between them. Comparing the results as well as the material specifics for the steels, the dominant property regarding resistance against the salt cavern conditions could be determined. For the specimen selection, in the optimal case one production parameter should be different between two steels only. For instance, two J55 with same chemical composition but differently produced or vice versa. Such a study would provide insight into the fundamental mechanisms. In addition, it could help for future material selection, as closer attention can be spent on the dominant property.

5.3 Suitability of steels for salt caverns

The material selection for UHS is one of the main challenges when tackling the task of large-scale hydrogen storage. While UGS in general is used for decades already, due to hydrogens ability to diffuse into and leak through materials the safety considerations have to be revised. While safety aspects are a general concern, companies construct caverns for gas storage to make profit, hence also economic factors such as the lifetime of the steel is of great interest. In this work, surface investigations were conducted for two steels exposed to salt cavern boundary conditions.

Based on these surface investigations trends regarding the corrosion and cracking of the surface could be observed. After 14 days in the chamber with brine, the EDX results for both steels show similar oxygen amounts, indicating surface coverage with iron oxide. Iron oxide naturally forms on iron/steel surfaces and was expected to be formed. It can serve a natural protection layer and is no general indication for a loss in material strength. However, an impact of hydrogen was observed in the EDX results for J55 suggesting additional reactions to take place besides the natural oxide formation. As explained, hydrogen could be able to change the composition of the oxide film by reducing oxygen species within it as well as catalysing iron dissolution. Changes in the chemical composition can induce changes in the electronic properties and stability, potentially resulting in a reduction of material strength. Comparing the J55 oxide film after 14 days in hydrogen gas and brine with the oxide film of X56, it can be seen that a uniform film is built on X56 while J55s surface is rough with local attack points. The images are shown in Figure 34. Protective oxide layers are produced by uniform corrosion, like the one in X56. Localised corrosion induces stress concentration factors, decreasing the material strength and resistance rather than increasing. Hence, the results suggest better resistance of X56 than J55.

In Figure 34a it can also be seen that extensive cracking over the entire surface of J55 takes place while for X56 (Figure 34b) only small cracks can be found. Further indicating better resistance of X56 than J55. In general, crack formation leads to a reduction in the material strength. No mechanical tests were conducted within this work; however, they are urgently required to determine the level of degradation. Classical tensile tests cannot be conducted with the specimens used in this work, as the cuboids do not fulfil the shape requirements. In addition, achieving the bone shape cutting a piece of the pipe is extremely difficult, considering the curvature of the pipe. Hence, alternative characterisation routes are required, micro tensile tests (M-TT) or the small punch test (SPT) might be possible [73]. The use of small specimens would additionally allow the characterisation of the exterior/interior as well as the characterisation of the perpendicular. Besides tensile tests other mechanical properties of the samples can be tested. The Rockwell hardness test is a feasible way to determine the hardness of a material [74]. As fully automated machines exist, it is suitable to be applied to all specimens comparing the hardness after each condition to the reference specimen. Usage of mechanical testing would allow for well-founded statements on the steel's suitability. Nevertheless, all results in this work indicate a better suitability of X56 than J55 from the scientific point of view. Note, in industrial applications there is always the need to find a compromise between economical and scientific arguments, which will not be discussed in this work.
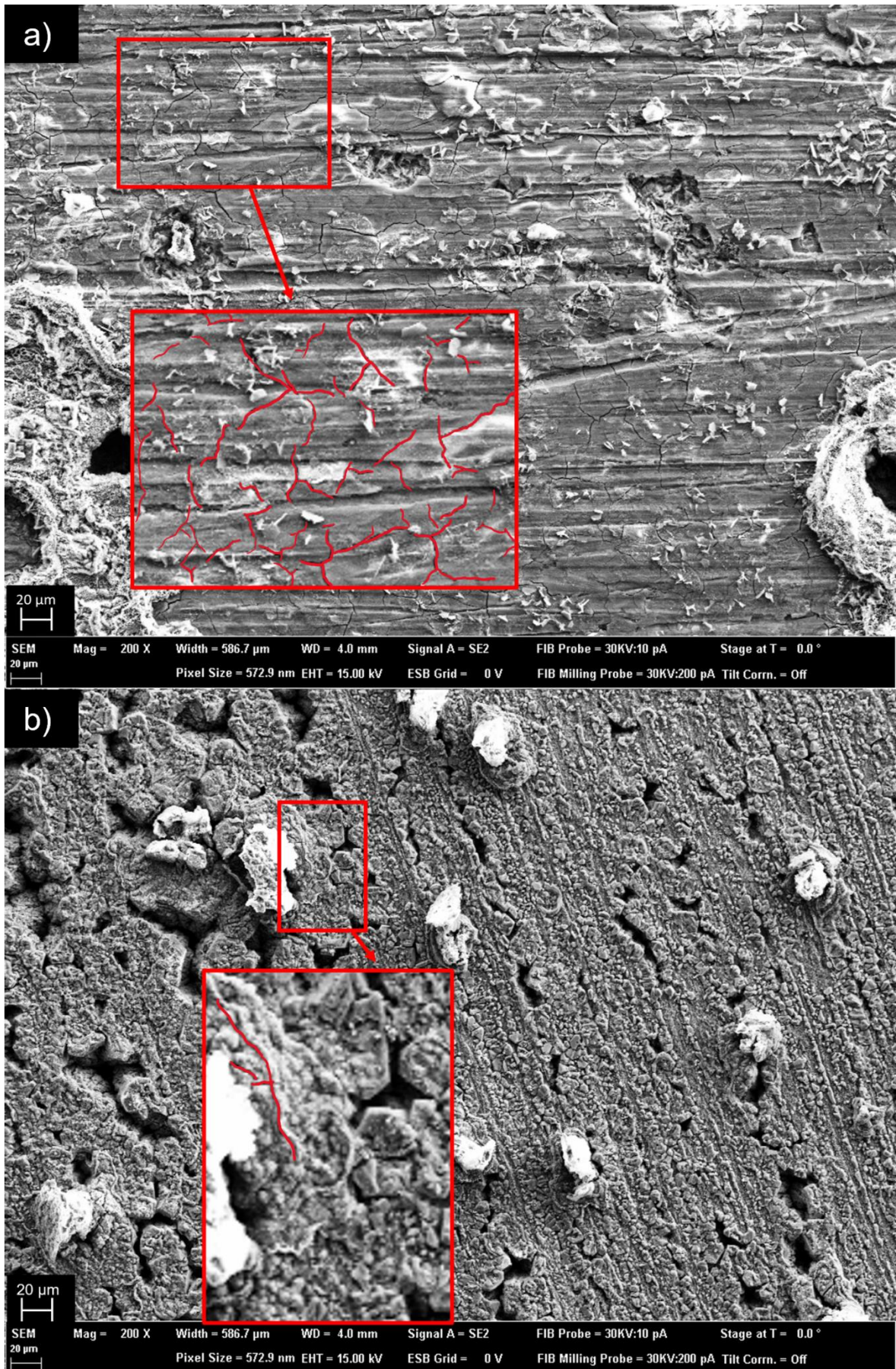
Figure 34: Cracks on the surface of a sanded a) J55 specimen and b) X56 specimen after 14 days in an autoclave with pressure/temperature cycling, 20 mL brine and hydrogen gas (purity 6.0). The figures show the side exposed to the brine. The red marked area has been magnified and cracks within the area are marked in red.

6. Conclusion

The impact of hydrogen under elevated pressure and temperature conditions with emulated salt cavern environments on the surface of the casing steel J55 and pipeline steel X56 was investigated in this work. Pressurized hydrogen gas with a purity of >99.9999 % in the experimental setup and the applied temperature/pressure cycles were kept constant. The pressure cycles between 90 bar and 150 bar resulted from the temperature cycling between -10 °C and 160 °C. The varied conditions were a dry chamber as well as moisture induced by ultra-pure water and salt ions induced by artificial brine. For comparison purpose, the same conditions were tested with nitrogen gas (purity >99.9999 %). For an allocation of the effects onto the surface, specimens were exposed to each condition for 72 hours in an autoclave. The effect of longer exposition times was studied for the extrema (dry and brine) in 2 weeks autoclave experiments. All specimens were characterised with SEM and EDX, focussing on corrosion effects and crack formation on the steels' surface.

The EDX results clearly show, that surface corrosion took place in all specimens of both steels; the degree of the corrosion depends on the applied conditions (dry, water or brine). A clear trend could be observed, that moisture and salt ions have an increasing intensification effect on the corrosion in both steels. But, only for J55 steel an raise of corrosion caused by hydrogen gas exposure was found. Another difference was observed in the SEM images, indicating localised corrosion for J55 steel but uniform corrosion for X56 steel. The differences are first indicators for a higher resistance of X56 steel than J55 steel against the conditions of UHS in salt caverns.

SEM imaging was also used to study the crack formation behaviour of the specimens. For J55 it was found, that the more extreme the condition, the more crack formation is obvious. Again, intensification due to the exposure to hydrogen gas could be seen. The results suggest HIC to be present when the steel is exposed to hydrogen gas. As also specimens exposed to nitrogen gas show crack formation, HIC cannot be the only crack formation mechanism but another mechanism must be present simultaneously. Comparison of the images with descriptions of various crack mechanisms suggests CF to be present, and potentially also SCC. Overall, pronounced crack formation over the entire surface of J55 was evident, resulting in the strong recommendation of further testing preferably including mechanical tests.

For X56 steel, significantly less crack formation could be observed and no clear dependency of the crack formation to the experimental conditions could be seen. A striking result, no intensification in crack formation could be observed for specimens exposed to hydrogen gas compared to specimens exposed to nitrogen gas. Hence, no HIC was present for X56 steel.

From the corrosion and crack formation results, it can be concluded, that X56 steel is not affected by hydrogen gas in the tested conditions. Overall, the results suggest better resistance against hydrogen gas and general salt cavern conditions for the studied X56 steel than J55 steel. Hence, from the scientific point of view, the results indicate better suitability of X56 steel. Nonetheless, the results need to be supported by mechanical testing prior to an implementation in salt caverns. For a broader discussion on the feasibility, environmental and economic aspects should be considered.

7. Outlook and Recommendations

In this work, steel samples were systematically exposed to salt cavern conditions and microscopically investigated. EDX results indicated corrosion of the steel surface wherein visible trends depending on the cavern conditions were found. SEM imaging showed surface cracking, for which trends could be found as well. The aim of the work was to find out about the visible effects and allocate them to their origin. Furthermore, trends should be found. While this aim was achieved, the work also demonstrated a great research potential for future studies not only for the applicability of the steels in salt caverns but also for fundamental research.

Future studies focussing on the applicability of the steels in salt caverns should include mechanical tests. The mechanical properties are important key parameters for the life cycle assessment (LCA) of the steels. While large specimens, as commonly used for classical tensile tests, might not be possible to realise, M-TT and SPT tests could be used for the determination of the parameters [73]. Also, hardness tests, for instance the Rockwell hardness test, are realisable for the shape of the steel specimens [74]. The comparison of mechanical properties for specimens with and without exposure to salt cavern conditions will provide information on the level of degradation of the material strength due to the corrosion and surface cracks.

Also recommended is another test series, in which the hydrogen gas/nitrogen gas is replaced by natural gas only. J55 is a commonly applied steel in salt caverns for natural gas storage, hence its life cycle is known. Conducting the same experiments using natural gas, common features with the hydrogen gas experiments would allow an assessment of the extent of degradation. While corrosion is known to have the ability to protect rather than harm steel, depending on the corrosion type, especially the occurrence frequency and size of surface cracking would be of interest.

Besides studies on the applicability of the steels, also fundamental research is recommended. In the EDX results of J55, a trend was visible indicating corrosion intensification by hydrogen exposure. More than one postulates exist on the reasoning. A reduction of the passive layer by hydrogen would cause a change in its stability and electronic properties. The change in properties could be measured by Mott-Schottky analysis [68]. Also, an intrinsic aggravation was postulated due to the accelerated iron dissolution triggered by a reduction in bonding strengths caused by trapped hydrogen. The iron dissolution could by confirmed by SIMS measurements, creating a depth profile of the oxide film [67].

Besides examination of the surface, also the internal changes in the bulk are of interest. In this work, the impact of the hydrogen gas was only determined indirectly by comparing the data. However, knowledge about amounts of hydrogen absorbed would potentially allow further interpretation of the data, especially for the comparison of steels. The usage of thermal desorption spectroscopy (TDS) can provide the information on the amount of adsorbed and absorbed hydrogen [75]. Further X-ray diffraction (XRD) could be used to receive microstructural data of the specimens before and after hydrogen exposure [76, 77]. In contrast to microstructural imaging in the SEM, XRD is a non-destructive technique which allows more characterisation techniques to be used for one sample.

Besides future studies on the steels, it is also recommended to test the resistance of further materials commonly applied in salt caverns, like sealing polymers and the cement. Especially the material combinations should be tested, as the interface of the materials is a particular weak point of the entire construction.

Bibliography

1.   Sun, Y.S., et al., *Overview of Energy Storage in Renewable Energy Power Fluctuation Mitigation.* Csee Journal of Power and Energy Systems, 2020. **6**(1): p. 160-173.
2.   Ball, M. and M. Wietschel, *The future of hydrogen – opportunities and challenges.* International Journal of Hydrogen Energy, 2009. **34**(2): p. 615-627.
3.   Kurrer, C., *The potential of hydrogen for decarbonising steel production*, S.F.U. (STOA), Editor. 2020, EPRS | European Parliamentary Research Service.
4.   Caglayan, D.G., et al., *Technical potential of salt caverns for hydrogen storage in Europe.* International Journal of Hydrogen Energy, 2020. **45**(11): p. 6793-6805.
5.   Papadias, D.D. and R.K. Ahluwalia, *Bulk storage of hydrogen.* International Journal of Hydrogen Energy, 2021. **46**(70): p. 34527-34541.
6.   Ma, X., *Handbook of underground gas storages and technology in china.* 2021, Singapore: Springer.
7.   Plaat, H., *Underground gas storage: Why and how.* Geological Society, London, Special Publications, 2009. **313**(1): p. 25-37.
8.   Panfilov, M., *4 - Underground and pipeline hydrogen storage*, in *Compendium of Hydrogen Energy*, R.B. Gupta, A. Basile, and T.N. Veziroğlu, Editors. 2016, Woodhead Publishing. p. 91-115.
9.   Rahman, M.M., et al., *Assessment of energy storage technologies: A review.* Energy Conversion and Management, 2020. **223**.
10.   Amrouche, S.O., et al., *Overview of energy storage in renewable energy systems.* International Journal of Hydrogen Energy, 2016. **41**(45): p. 20914-20927.
11.   Zohuri, B., *Hydrogen Energy: Challenges and Solutions for a Cleaner Future*. 2018.
12.   Hirscher, M., et al., *Materials for hydrogen-based energy storage - past, recent progress and future outlook.* Journal of Alloys and Compounds, 2020. **827**.
13.   Schlapbach, L. and A. Zuttel, *Hydrogen-storage materials for mobile applications.* Nature, 2001. **414**(6861): p. 353-358.
14.   Liebscher, A., J. Wackerl, and M. Streibel, *Geologic Storage of Hydrogen – Fundamentals, Processing, and Projects.* Hydrogen Science and Engineering : Materials, Processes, Systems and Technology, 2016: p. 629-658.
15.   Ozarslan, A., *Large-scale hydrogen energy storage in salt caverns.* International Journal of Hydrogen Energy, 2012. **37**(19): p. 14265-14277.
16.   IEA. *Key energy statistics - Germany.* [cited 2022 20.01]; Available from: https://www.iea.org/countries/germany.
17.   Crotogino, F., et al., *Large-Scale Hydrogen Underground Storage for Securing Future Energy Supplies.* 2010.
18.   Zivar, D., S. Kumar, and J. Foroozesh, *Underground hydrogen storage: A comprehensive review.* International Journal of Hydrogen Energy, 2021. **46**(45): p. 23436-23462.
19.   Berest, P. and F. Louvet, *Aspects of the thermodynamic behavior of salt caverns used for gas storage.* Oil & Gas Science and Technology-Revue D Ifp Energies Nouvelles, 2020. **75**.
20.   DIN, *DIN EN 17124:2019-07, Wasserstoff als Kraftstoff - Produktfestlegung und Qualitätssicherung - Protonenaustauschmembran(PEM) - Brennstoffzellenanwendungen für Stra\ss enfahrzeuge; Deutsche Fassung EN 17124:2018*. 2019.
21.   Ratnakar, R.R., B. Dindoruk, and A. Harvey, *Thermodynamic modeling of hydrogen-water system for high-pressure storage and mobility applications.* Journal of Natural Gas Science and Engineering, 2020. **81**.
22.   Wiebe, R. and V.L. Gaddy, *The Solubility of Hydrogen in Water at 0, 50, 75 and 100° from 25 to 1000 Atmospheres.* Journal of the American Chemical Society, 1934. **56**(1): p. 76-79.
23.   Maslennikova, V.Y., et al., *Solubility of Water in Compressed Hydrogen.* Zhurnal Fizicheskoi Khimii, 1976. **50**(2): p. 411-414.
24.   Rahbari, A., et al., *Solubility of Water in Hydrogen at High Pressures: A Molecular Simulation Study.* Journal of Chemical and Engineering Data, 2019. **64**(9): p. 4103-4115.

25. Réveillère, A., B. Azimi, and C. Arnold, *Prevention of stored gas humidification: lessons learnt and review of possibilities*. 2016.

26. Laban, M.P., *Hydrogen Storage in Salt Caverns: Chemical modelling and analysis of large-scale hydrogen storage in underground salt caverns.*, in *Mechanical, Maritime and Materials Engineering*. 2020, Delft University of Technology.

27. Lin, F., et al., *Experimental Studies on Corrosion Behaviors of Casing Steel N80 in High Salinity of Brine.* Advanced Materials Research, 2014. **1081**: p. 205-209.

28. Mao, X., X. Liu, and R.W. Revie, *Pitting Corrosion of Pipeline Steel in Dilute Bicarbonate Solution with Chloride-Ions.* Corrosion, 1994. **50**(9): p. 651-657.

29. Faust, S.F.I.J.U., *Forschungen zum Wasserstoffeinfluss auf das Verhalten von Konstruktionswerkstoffen in Kernkraftwerken*. 2020.

30. Pundt, A. and R. Kirchheim, *Hydrogen in metals: Microstructural aspects.* Annual Review of Materials Research, 2006. **36**: p. 555-608.

31. Nagumo, M., *Fundamentals of Hydrogen Embrittlement*. 2016. 1-239.

32. Robertson, I.M., et al., *Hydrogen Embrittlement Understood.* Metallurgical and Materials Transactions B-Process Metallurgy and Materials Processing Science, 2015. **46**(3): p. 1085-1103.

33. Li, X.F., et al., *Review of Hydrogen Embrittlement in Metals: Hydrogen Diffusion, Hydrogen Characterization, Hydrogen Embrittlement Mechanism and Prevention.* Acta Metallurgica Sinica-English Letters, 2020. **33**(6): p. 759-773.

34. Group, H.S.S.C.a.H.I. *X70 steel*. 2017 [cited 2022 05.01]; Available from: https://www.hu-steel.com/news363_822.html.

35. Mohtadi-Bonab, M.A., et al., *The mechanism of failure by hydrogen induced cracking in an acidic environment for API 5L X70 pipeline steel.* International Journal of Hydrogen Energy, 2015. **40**(2): p. 1096-1107.

36. Bae, D.S., et al., *Effect of highly pressurized hydrogen gas charging on the hydrogen embrittlement of API X70 steel.* Metals and Materials International, 2014. **20**(4): p. 653-658.

37. Haq, A.J., et al., *Effect of microstructure and composition on hydrogen permeation in X70 pipeline steels.* International Journal of Hydrogen Energy, 2013. **38**(5): p. 2544-2556.

38. Hejazi, D., et al., *Effect of manganese content and microstructure on the susceptibility of X70 pipeline steel to hydrogen cracking.* Materials Science and Engineering a-Structural Materials Properties Microstructure and Processing, 2012. **551**: p. 40-49.

39. Wang, P.Y., et al., *Tensile and impact properties of X70 pipeline steel exposed to wet H2S environments.* International Journal of Hydrogen Energy, 2015. **40**(35): p. 11514-11521.

40. Capelle, J., et al., *Sensitivity of pipelines with steel API X52 to hydrogen embrittlement.* International Journal of Hydrogen Energy, 2008. **33**(24): p. 7630-7641.

41. Boukortt, H., et al., *Hydrogen embrittlement effect on the structural integrity of API 5L X52 steel pipeline.* International Journal of Hydrogen Energy, 2018. **43**(42): p. 19615-19624.

42. Brauer, H.S., Manuel; Wanzenberg, Elke; Henel, Marco; Huising, Otto Jan, *Energiewende mit Wasserstoffrohren "H2Ready" und Umstellung existierender Erdgasnetze.* 3R Fachzeitschrift für sichere und effiziente Rohrleitungssysteme, 2020. **3**: p. 32-45.

43. Institute, A.P., *Line Pipe - API SPECIFICATION 5L*. 2018, API Publishing Services: Washington, D. C.

44. Octal. *API 5CT Casing and Tubing Specification*. [cited 2022 07.01]; Available from: https://www.octalsteel.com/api-5ct-specification.

45. Mannesmann-Line-Pipe-GmbH. *Oilfield tubulars (OCTG)*. [cited 2022 07.01]; Available from: https://www.mannesmann-linepipe.com/en/supply-range/oilfield-tubulars-octg.html.

46. Institute, A.P., *Casing and Tubing - API Specification 5CT*. 2018, API Publishing Services: Washington, D. C.

47. Boersheim, E., et al., *Experimental Investigation of Integrity Issues of UGS Containing Hydrogen*. 2019.

48. Trautmann, A., et al., *Hydrogen Uptake and Embrittlement of Carbon Steels in Various Environments.* Materials, 2020. **13**(16).

49. Willett, E., *Hydrogen induced cracking of electric welded J55 casing.* NACE - International Corrosion Conference Series, 2010.

50. Sastri, V.S., *Challenges in Corrosion*. Costs, Causes, Consequences, and Control. 2015: John Wiley & Sons. 1-432.

51. Joseph I. Goldstein, D.E.N., Joseph R. Michael, Nicholas W.M. Ritchie, John Henry J. Scott, David C. Joy, *Scanning Electron Microscopy and X-Ray Microanalysis*. Vol. 4. 2018, New York: Springer.

52. S. L. Flegler, J.W.H.J., K. L. Klomparens, *Elektronenmikroskopie: Grundlagen, Methoden, Anwendungen*. 1995, Berlin, Oxford,: Spektrum Akademischer Verlag.

53. Reimer, L., *Scanning Electron Microscopy*. 1998, Münster: Springer-Verlag.

54. indirekt, C. *Energiedispersive Röntgenspektroskopie*. [cited 2022 12.09]; Available from: https://www.cosmos-indirekt.de//Physik-Schule/Energiedispersive_R%c3%b6ntgenspektroskopie.

55. Meetyou. *8 Common Microstructures of Metal and Alloy*. 2019 [cited 2022 09.08]; Available from: https://www.meetyoucarbide.com/common-microstructures-of-metal-and-alloy/.

56. Sk, M., et al., *The Effects of Cr/Mo Micro-Alloying on the Corrosion Behavior of Carbon Steel in CO_2-Saturated (Sweet) Brine under Hydrodynamic Control.* Journal of The Electrochemical Society, 2018. **165**: p. C278-C288.

57. Clover, D., et al., *The influence of microstructure on the corrosion rate of various carbon steels.* Journal of Applied Electrochemistry, 2005. **35**(2): p. 139-149.

58. *Produktdatenblatt Wasserstoff 6.0*, L. GmbH, Editor.

59. *Produktdatenblatt Stickstoff 6.0*, L. GmbH, Editor.

60. McCafferty, E., *Thermodynamics of Corrosion: Pourbaix Diagrams*, in *Introduction to Corrosion Science*. 2010, Springer: New York. p. 95-117.

61. Spreitzer, D. and J. Schenk, *Reduction of Iron Oxides with Hydrogen—A Review.* steel research international, 2019. **90**(10): p. 1900108.

62. *Produktdatenblatt Wasserstoff 5.0*, L. GmbH, Editor.

63. Talbot, D.E.J. and J.D.R. Talbot, *7.2.1.2 Iron(II) Oxides, Hydroxides and Derivatives*, in *Corrosion Science and Technology (3rd Edition)*. CRC Press.

64. Cornell, R.M. and U. Schwertmann, *The iron oxides : structure, properties, reactions, occurrences, and uses*. 2003, Wiley-VCH: Weinheim.

65. Thomas, S., et al., *The Effect of Absorbed Hydrogen on the Corrosion of Steels: Review, Discussion, and Implications.* Corrosion, 2017. **73**(4): p. 426-436.

66. Thomas, S., et al. *The effect of absorbed hydrogen on the dissolution of steel*. Heliyon, 2016. **2**, e00209 DOI: 10.1016/j.heliyon.2016.e00209.

67. Heide, P.v.d., *Secondary Ion Mass Spectrometry - An introduction to Principles and Practices*. 2014, New York: John Wiley Sons.

68. Zonno, I., et al., *Understanding Mott-Schottky Measurements under Illumination in Organic Bulk Heterojunction Solar Cells.* Physical Review Applied, 2017. **7**(3): p. 034018.

69. Elfergani, H. and A. Abdalla, *EFFECT OF CHLORIDE CONCENTRATION ON THE CORROSION RATE IN CARBON STEEL*. 2017.

70. Zhao, X.H., et al. *Effects of Cl- concentration on corrosion behavior of carbon steel and super13cr steel in simulated oilfield environments*. in *Proceedings of the 2016 International Conference on Innovative Material Science and Technology (IMST 2016)*. 2016. Atlantis Press.

71. Kasthuri Rajagopalan, K., *Effect of Sodium Chloride Concentration on the Corrosion of Carbon Steels and Stainless Steels in CO2 Environment at Atmospheric Pressure under Turbulent Flow Condition*. 2014.

72. Konstanz, U. *SEM-FIB Systeme*. [cited 2022 31.08]; Available from: https://www.physik.uni-konstanz.de/nano/ausstattung/mikroskopie/sem-fib-systeme/.

73. Konopik, P., et al., *Application of micro-tensile test for material characterization of mild steel DC01*. Ubiquity Proceedings, 2018. **1**: p. 33.

74. Low, S., *NIST Recommended Practice Guide: Rockwell Hardness Measurement of Metallic Materials*. 2001, National Institute of Standards and Technology: Gaithersburg.

75. Verbeken, K., *2 - Analysing hydrogen in metals: bulk thermal desorption spectroscopy (TDS) methods*, in *Gaseous Hydrogen Embrittlement of Materials in Energy Technologies*, R.P. Gangloff and B.P. Somerday, Editors. 2012, Woodhead Publishing. p. 27-55.

76. Cullity, B.D., *Elements of X-ray Diffraction*. 1978: Addison-Wesley Publishing Company.

77.   Ungár, T., *Microstructural parameters from X-ray diffraction peak broadening.* Scripta Materialia, 2004. **51**(8): p. 777-781.

78.   Katsina, C., et al., *Characterization of Beach/River Sand for Foundry Application.* Leonardo Journal of Sciences, 2013. **12**: p. 77-83.

79.   Fergusson, J.E., et al., *The elemental composition and sources of house dust and street dust.* Science of The Total Environment, 1986. **50**: p. 217-221.

80.   Finlay, C. and C.T. Morley-Smith, *ZINC-RICH PAINTS.* Anti-Corrosion Methods and Materials, 1954. **1**(10): p. 383-385.

81.   Tabish, A., *Carbon based Coatings.* 2018. p. 321-354.

82.   Boan, M., et al., *Ionic liquids improve the anticorrosion performance of Zn-rich coatings.* RSC Adv., 2014. **4**.

Appendix A – Experimental

The J55 and X56 samples were provided by the EWE GASSPEICHER GmbH and Mannesmann Line Pipe GmbH, respectively. It has to be noted, that the EWE GASSPEICHER GmbH could not provide information about the material, hence the J55 material should be confirmed. However, for simplification the naming J55 will be used throughout the work. Both companies provided the material as pipe, the specimen cutting with a water jet cutter was outsourced and afterwards punched out of the pipe by Holger Janßen. Pictures of the pipes and the cutting are shown below in Figure 35 and Figure 36.
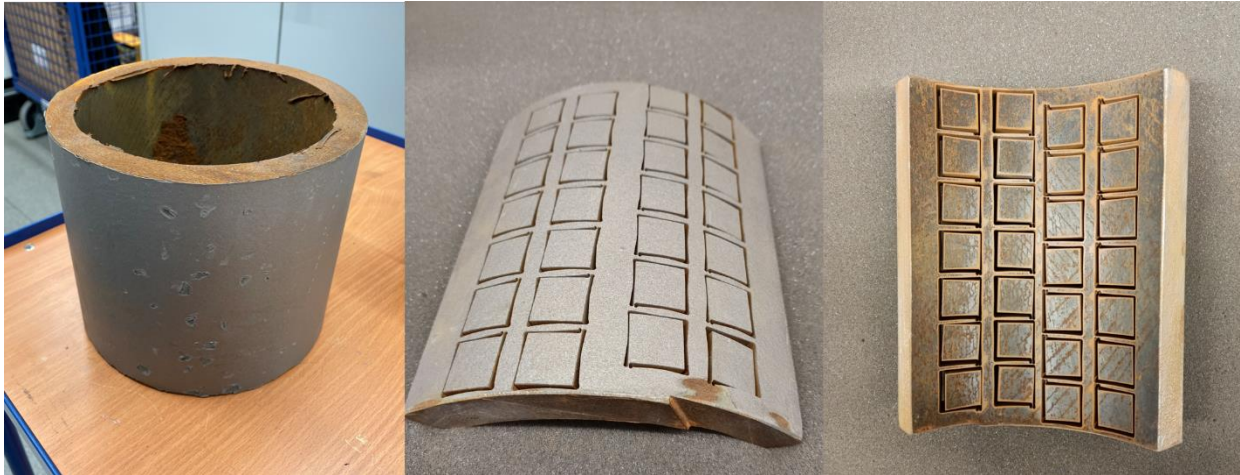
Figure 35: J55 steel pipe provided by the EWE GASSPEICHER GmbH. a) entire piece, b) exterior with water jet cuts and c) interior with water jet cuts.

Figure 36: H2ready X56 steel provided by Mannesmann Line Pipe GmbH. Interior sides with water jet cuts.

Each experiment was conducted with one of the steel cuboids, which can be seen in the Figures. For clear assignment of each specimen after the experiment, each experiment was numbered consecutively, the same was conducted for the specimens themselves. The 3 days experiments were assigned with numbers, the 14 days experiments with letters. The specimen numbers are continuous over all experiments. The assignment to the testing conditions is shown in Table 9 for J55 and Table 10 for X56. Missing numbers in the specimen count are caused by failed experiments which needed to be redone.

Table 9: Assignment of numbering of experiments and specimens for the J55 steel structured in testing conditions.

3 days	J55 untreated – number (H2 | N2)		J55 P180 sanded – number (H2 | N2)	
Dry	Exp 4 – S8	Exp 4 – S9	Exp 8 – S19	Exp 8 – S20
Q-milli water	Exp 6 – S14	Exp 6 – S15	Exp 9 – S24	Exp 9 – S25
Artificial brine	Exp 3 – S6	Exp 3 – S7	Exp 5 – S11	Exp 5 – S13
14 days	J55 untreated – number (H2)		J55 P180 sanded – number (H2)	
Dry	Exp A – S18		Exp C_2 – S35	
Artificial brine	Exp B_2 – S34		Exp D_2 – S36	

Table 10: Assignment of numbering of experiments and specimens for the X56 steel structured in testing conditions.

3 days	X56 untreated – number (H2 | N2)		X56 P220 sanded – number (H2 | N2)	
Dry	Exp 12 – S30	Exp 12 – S31	Exp 11 – S28	Exp 11 – S29
Q-milli water	Exp 7 – S16	Exp 7 – S17	Exp 13 – S32	Exp 13 – S33
Artificial brine	Exp 2 – S2	Exp 2 – S4	Exp 10 – S26	Exp 10 – S27
14 days	J55 untreated – number (H2)		J55 P180 sanded – number (H2)	
Dry	Exp E – S37		G – S39	
Artificial brine	Exp F – S38		H – S40	

Appendix B – Results

EDX - J55 steel provided by EWE GASSPEICHER GmbH

In this part, the complete EDX results of the J55 specimen are presented. In Figure 37 untreated specimens exposed to hydrogen gas (left column) or nitrogen gas (right column) for three days can be seen. The rows are structured in dry, water and brine conditions from top to bottom. Using the same structure in Figure 38, the results for sanded specimens are represented. In Figure 39 are the results for 14 days hydrogen gas exposition shown. In this figure, untreated (left column) and sanded (right column) specimens are represented together. The top row represents dry condition, the bottom row brine conditions.

Comparison of the untreated and the sanded specimen in dry conditions show, that Aluminium (Al), Magnesium (Mg) and Calcium (Ca) can only be found for untreated specimen. As the pipe, from which the specimen was cut out, was stored in a non-laboratory environment, the elements can originate from the storage. The untreated specimen was not washed before the autoclave experiment, but afterwards (2 min ultrasonic bath in ultrapure water followed by 2 min in isopropanol). As corrosion products deposit on the sample surface during the autoclave experiment, potentially the contaminations from storage are contained after the washing. Al, Mg and Ca can all be found in sand [78]. Also, Al and Ca can be found in dust [79], however dust would potentially bring more elemental contamination into the system. Since sand can commonly be found on construction sites, its presence is likely.

In the water conditions, the moisture in the chamber can lead to relocation of elements from the exterior and interior to the characterised side. It has to be noted that an extra coating is present on the exterior, inserting for instance zinc. For the brine condition the processes are much more complex due to the chemical composition of the brine itself.
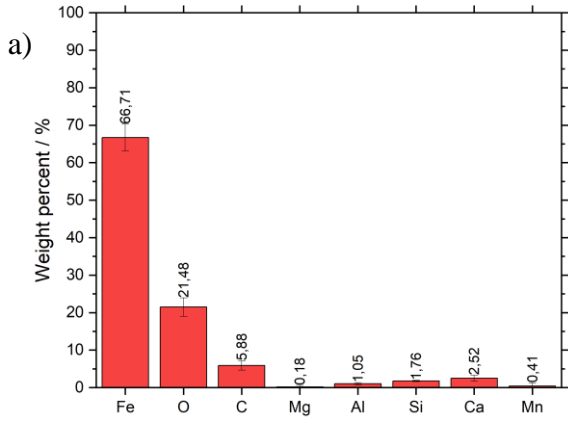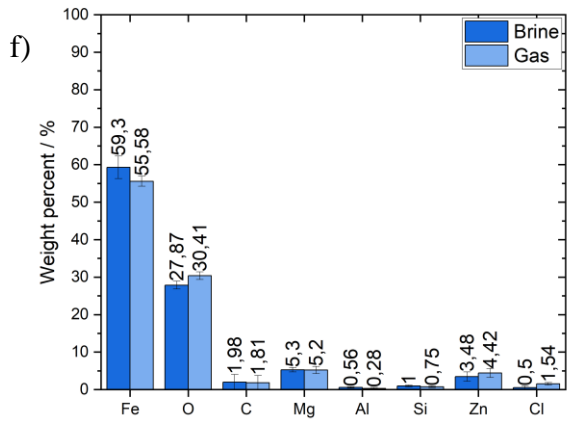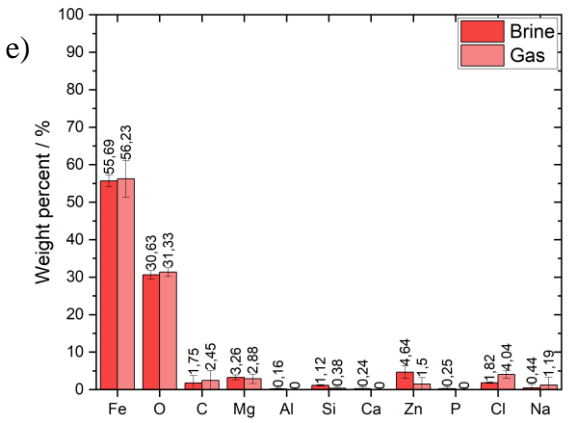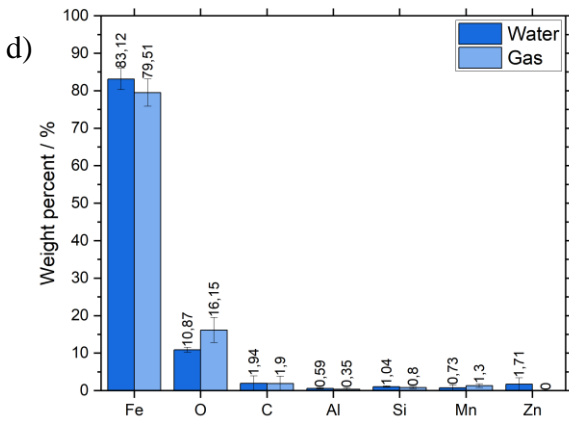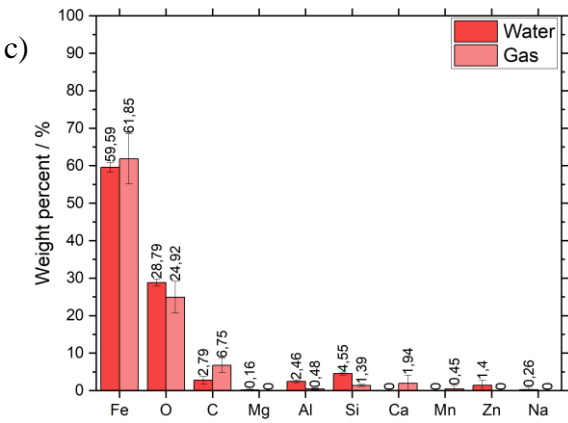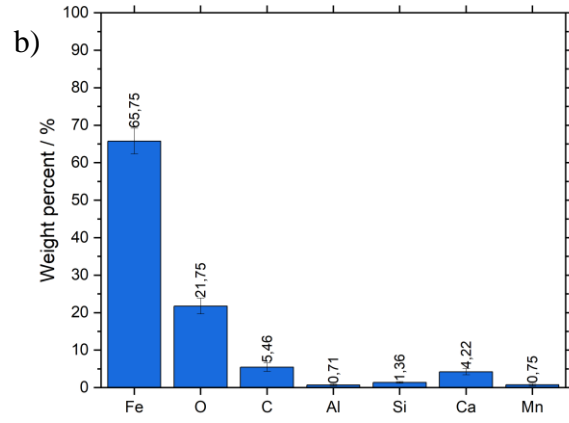
Figure 37: EDX surface data of untreated J55 samples, in chamber for 3 days. a) and b) samples for dry conditions, c) and d) samples for ultra-pure water conditions, e) and f) samples for artificial brine conditions.
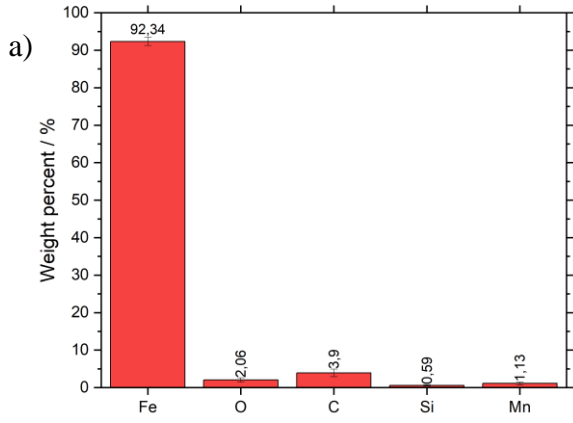
Figure 38: EDX surface data of sanded J55 samples, in chamber for 3 days. a) and b) samples for dry conditions, c) and d) samples for ultra-pure water conditions, e) and f) samples for artificial brine conditions.
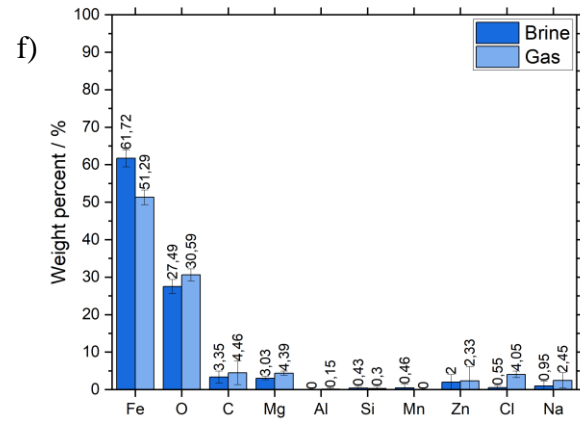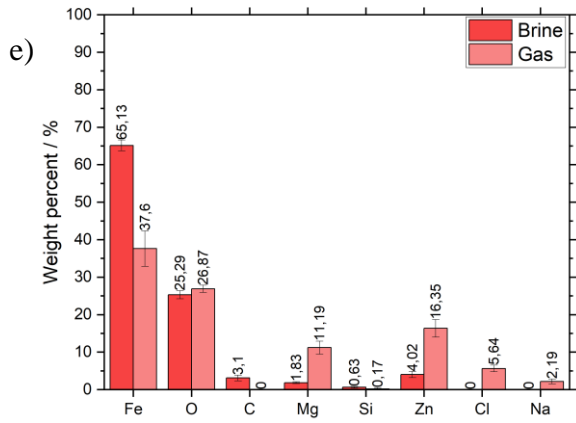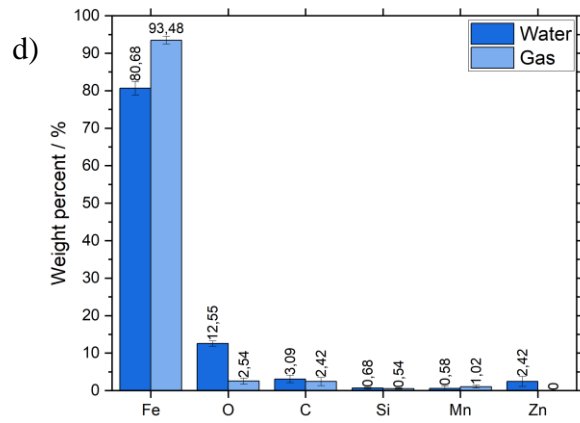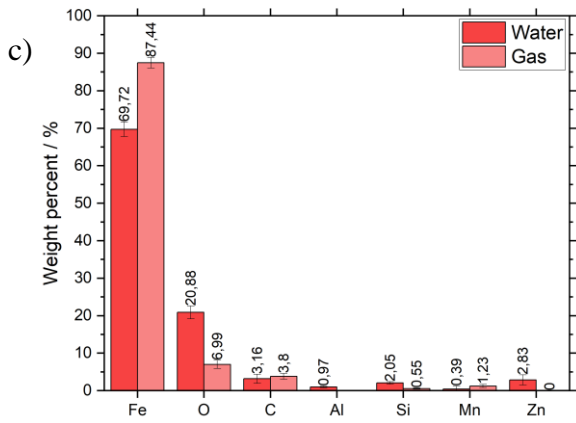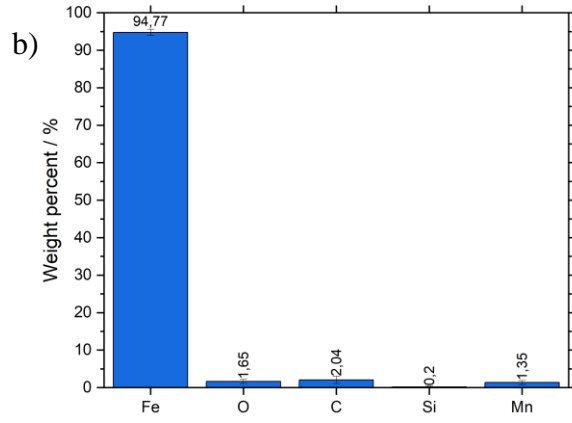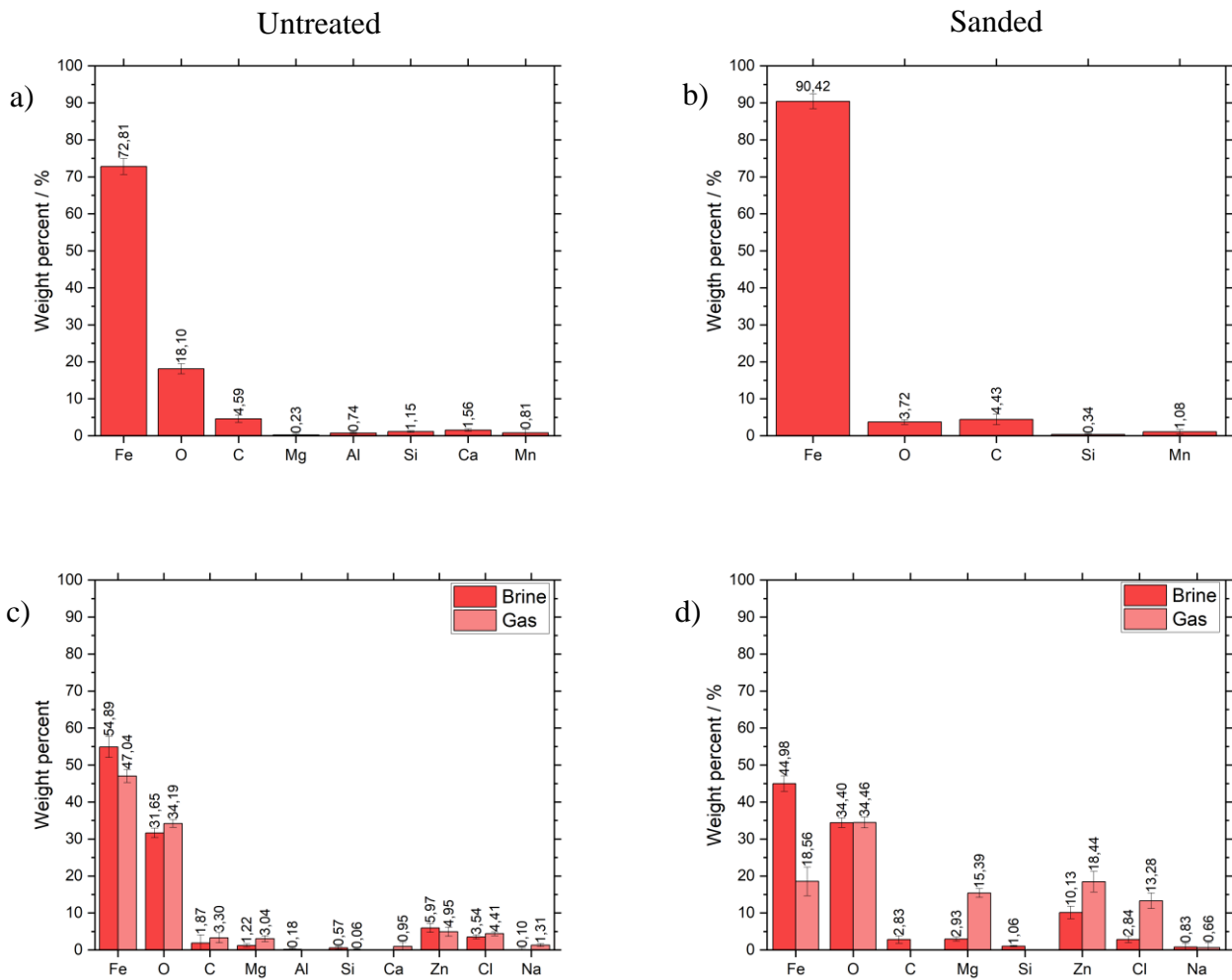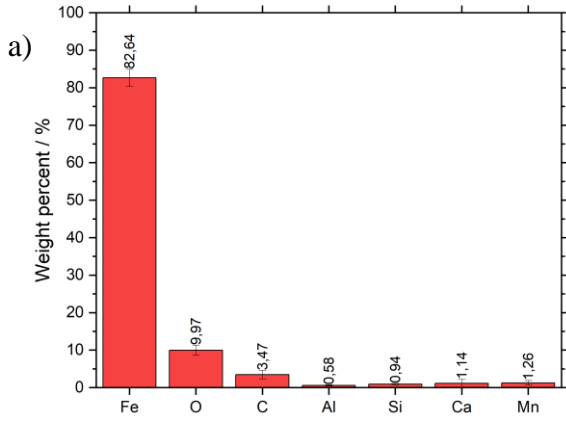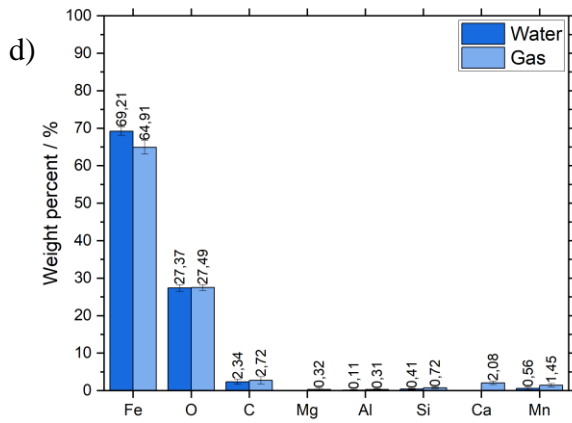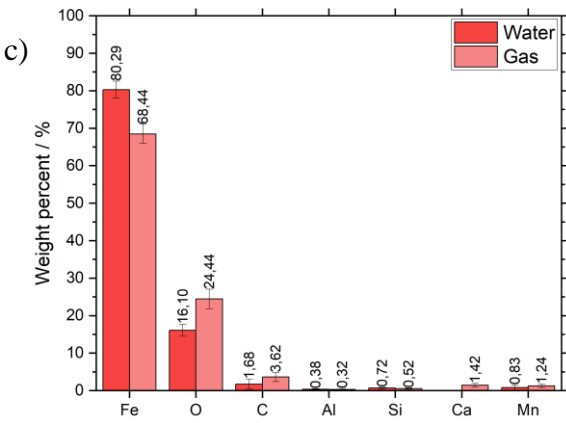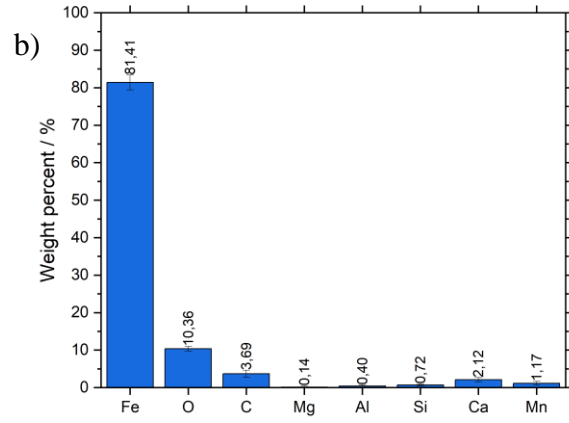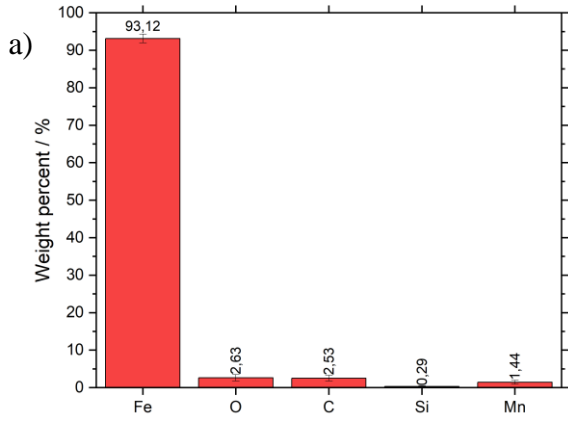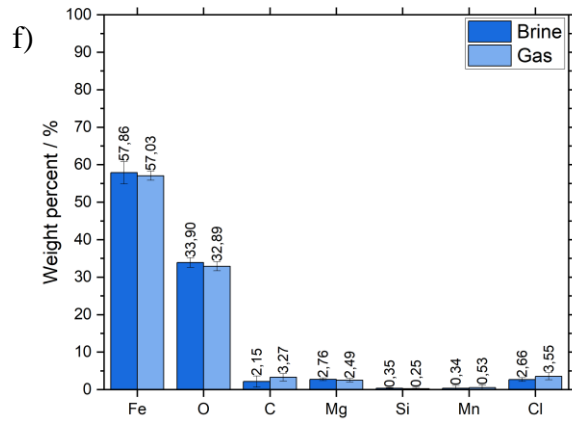
Figure 39: EDX surface data of J55 samples, in chamber for 14 days. a) and b) samples for dry conditions, c) and d) artificial brine conditions. Results in column 1 (a) and e)) are for untreated samples and column 2 (b), and d)) for sanded samples.

EDX - H₂-ready X56 steel provided by Mannesmann Line Pipe GmbH

In this part, the complete EDX results of the H_2-ready X56 specimens are presented. In Figure 40 untreated specimens exposed to hydrogen gas (left column) or nitrogen gas (right column) for three days can be seen. The rows are structured in dry, water and brine conditions from top to bottom. Using the same structure in Figure 41, the results for sanded specimens are represented. In Figure 42 are the results for 14 days hydrogen gas exposition shown. In this figure, untreated (left column) and sanded (right column) specimens are represented together. The top row represents dry condition, the bottom row brine conditions.

The differences of the elemental distribution between untreated and sanded specimen are similar to J55 and will not be elaborated upon once again. No zinc was measured, which confirms the coating as origin for the zinc in J55 measurements as no coating was present on the surface of X56.
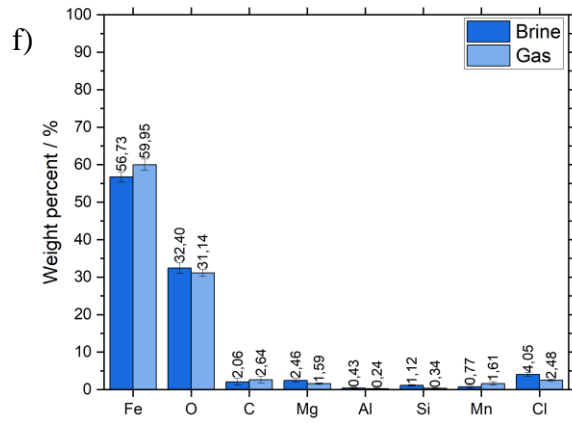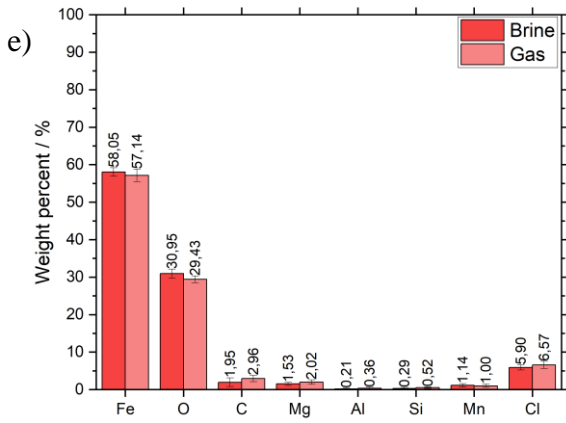
Figure 40: EDX surface data of untreated X56 samples, in chamber for 3 days. a) and b) samples for dry conditions, c) and d) samples for ultra-pure water conditions, e) and f) samples for artificial brine conditions.
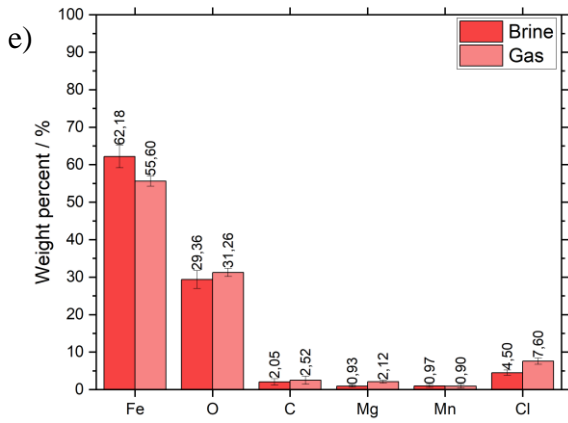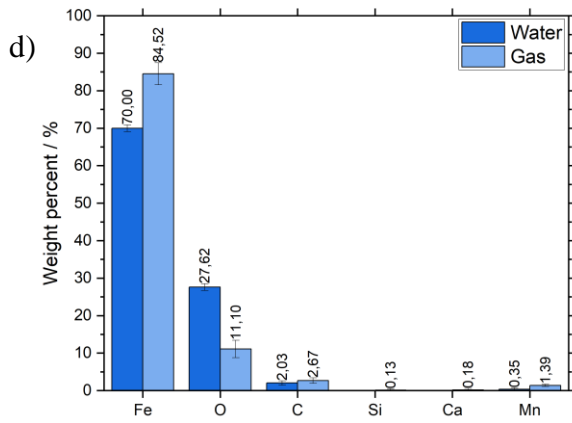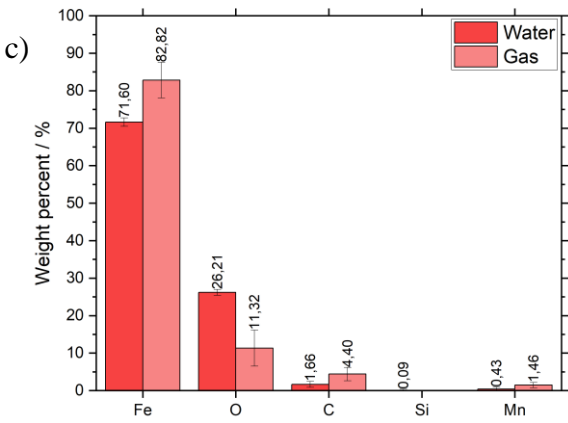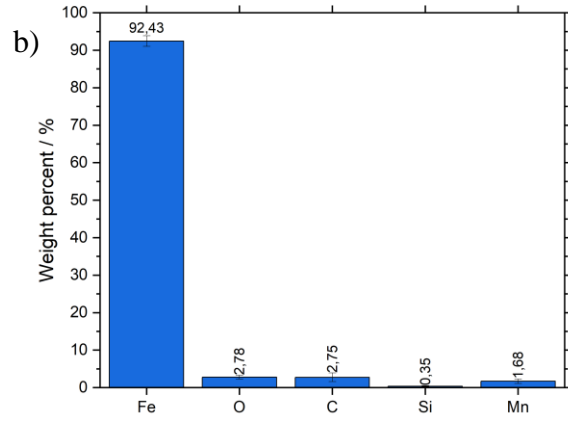
Figure 41: EDX surface data of sanded X56 samples, in chamber for 3 days. a) and b) samples for dry conditions, c) and d) samples for ultra-pure water conditions, e) and f) samples for artificial brine conditions.

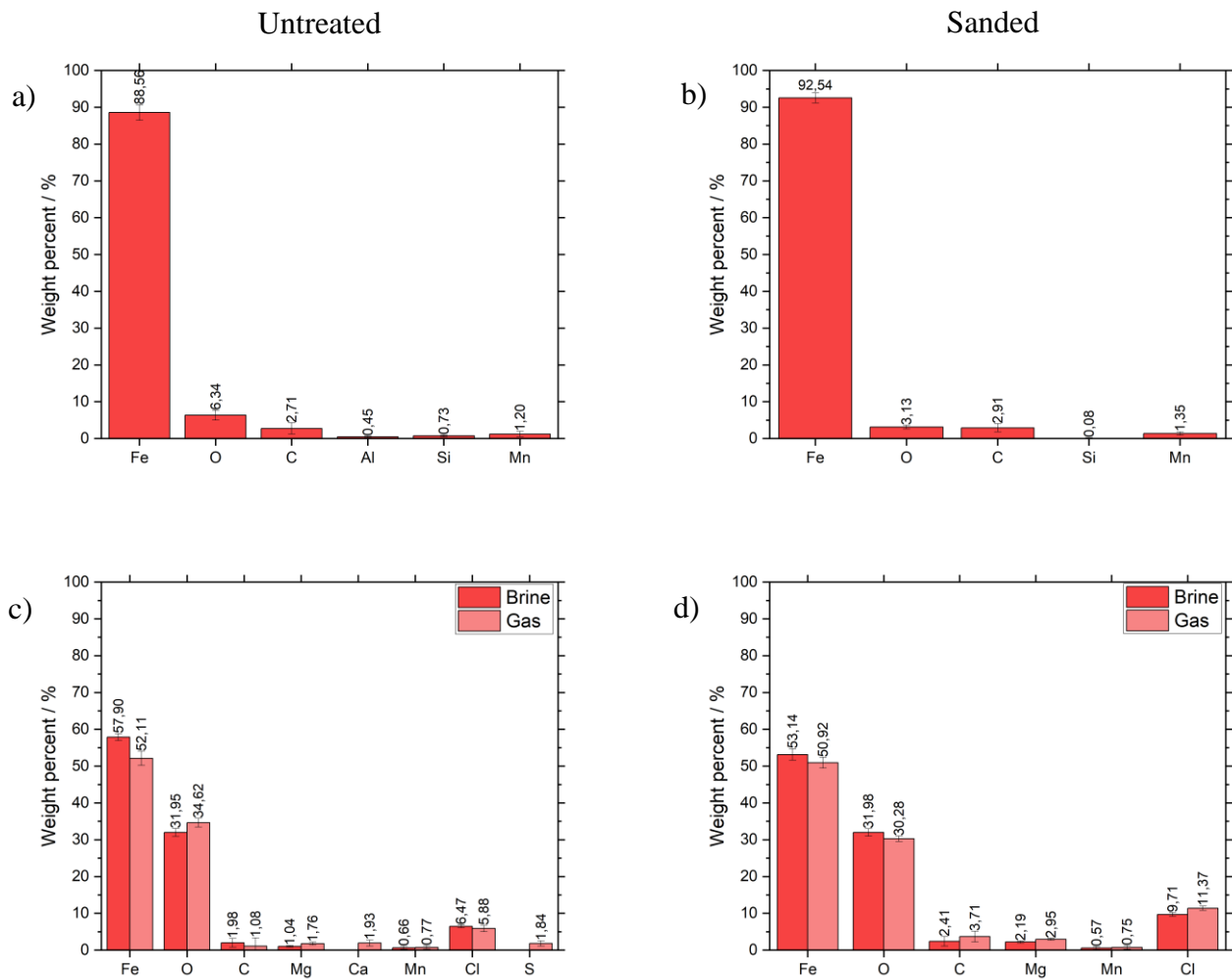Untreated   Sanded

Figure 42: EDX surface data of X56 samples, in chamber for 14 days. a) and b) samples for dry conditions, c) and d) artificial brine conditions. Results in column 1 (a) and e)) are for untreated samples and column 2 (b), and d)) for sanded samples.

SEM - J55 steel provided by EWE GASSPEICHER GmbH

Only a selection of SEM images was presented in the main part of this work. In this subsection, one SEM images with 200X magnification for each specimen is shown for the sake of completeness. The differences in the surface of specimen exposed to hydrogen a nitrogen can be seen. While for the untreated specimen it is hard to differentiate as the surface is rough either way, for sanded specimen the worsening effect of hydrogen, explained in the main part, is more pronounced.

Untreated – Dry – H$_2$ — 3 days
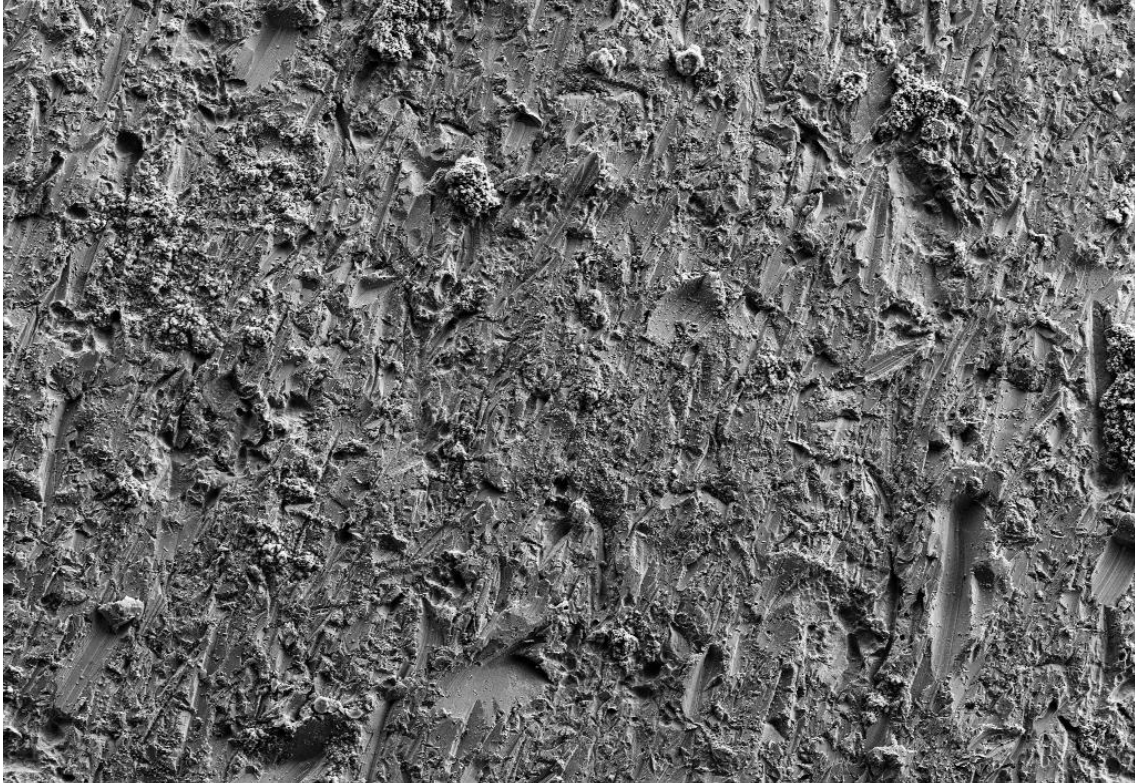
SEM Mag = 100 X Width = 1.173 mm WD = 5.0 mm Signal A = SE2 FIB Probe = 30KV:10 pA Stage at T = 0.0 °
100 µm Pixel Size = 1.146 µm EHT = 15.00 kV ESB Grid = 0 V FIB Milling Probe = 30KV:200 pA Tilt Corrn. = Off

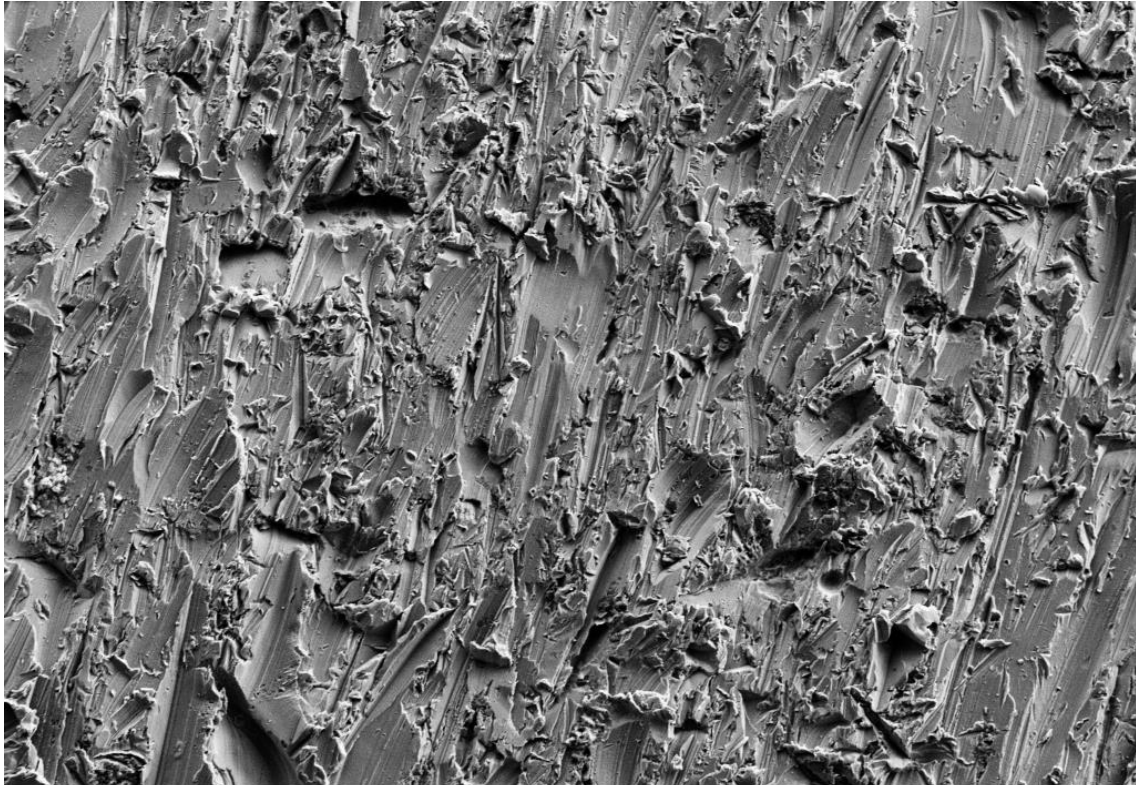Untreated – Dry – N$_2$ — 3 days

SEM Mag = 200 X Width = 586.7 µm WD = 4.0 mm Signal A = SE2 FIB Probe = 30KV:10 pA Stage at T = 0.0 °
20 µm Pixel Size = 572.9 nm EHT = 15.00 kV ESB Grid = 0 V FIB Milling Probe = 30KV:200 pA Tilt Corrn. = Off

SEM 20 µm | Mag = 200 X | Width = 586.7 µm | WD = 4.0 mm | Signal A = SE2 | FIB Probe = 30KV:10 pA | Stage at T = 0.0 °
Pixel Size = 572.9 nm | EHT = 15.00 kV | ESB Grid = 0 V | FIB Milling Probe = 30KV:200 pA | Tilt Corrn. = Off

SEM 20 µm | Mag = 200 X | Width = 586.7 µm | WD = 4.0 mm | Signal A = SE2 | FIB Probe = 30KV:10 pA | Stage at T = 0.0 °
Pixel Size = 572.9 nm | EHT = 15.00 kV | ESB Grid = 0 V | FIB Milling Probe = 30KV:200 pA | Tilt Corrn. = Off

Untreated – Brine – H$_2$ — **3 days**

SEM | Mag = 200 X | Width = 586.7 µm | WD = 4.0 mm | Signal A = SE2 | FIB Probe = 30KV:10 pA | Stage at T = 0.0 °
20 µm | | Pixel Size = 572.9 nm | EHT = 15.00 kV | ESB Grid = 0 V | FIB Milling Probe = 30KV:200 pA | Tilt Corrn. = Off
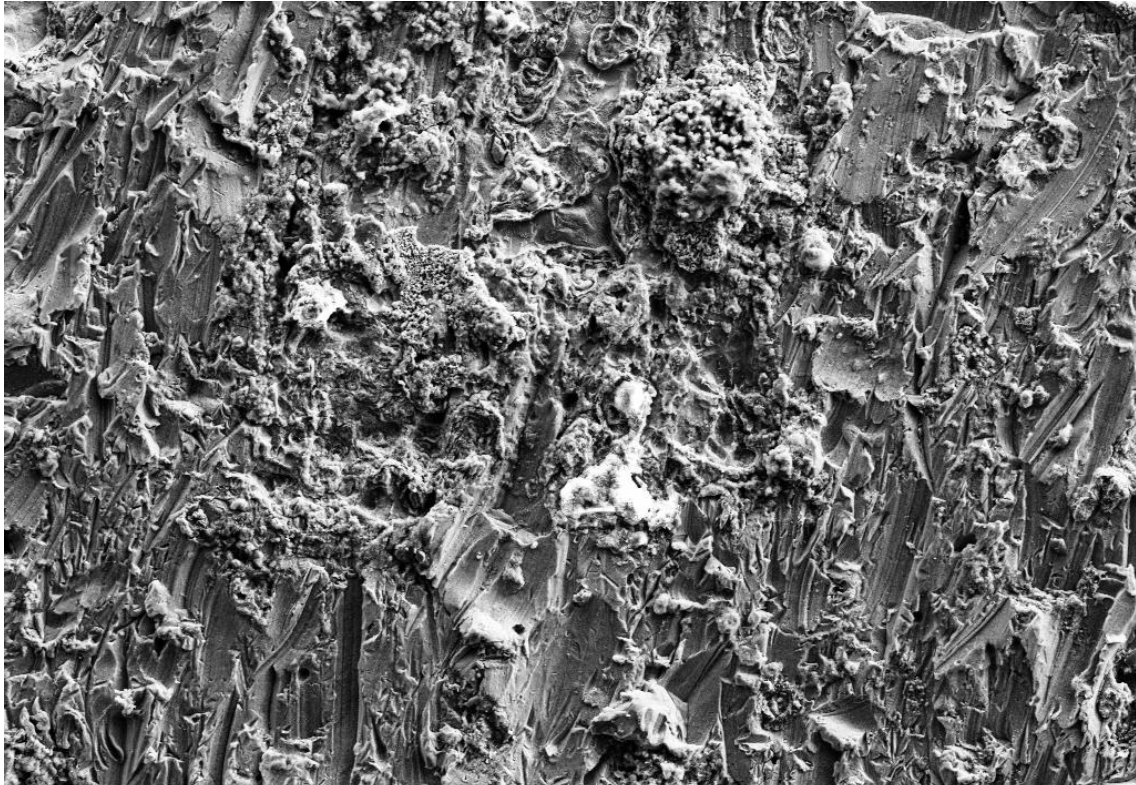

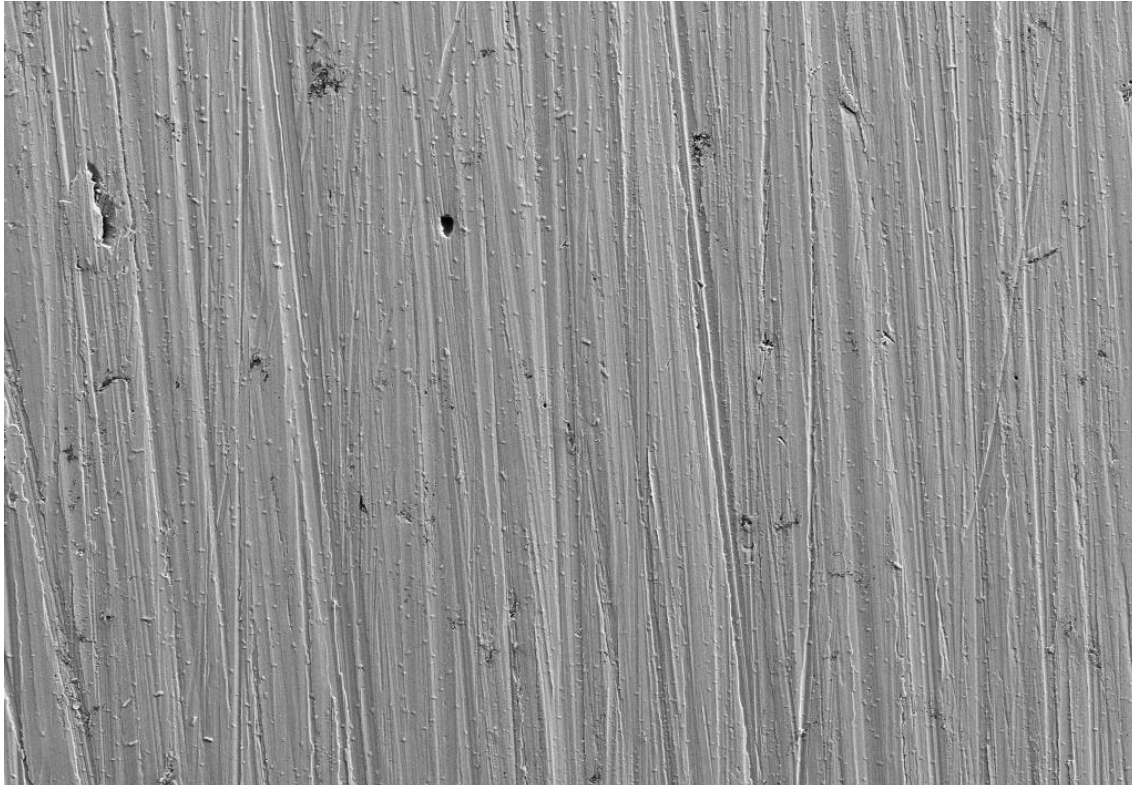**Untreated – Brine – N$_2$** — **3 days**

SEM | Mag = 200 X | Width = 586.7 µm | WD = 4.0 mm | Signal A = SE2 | FIB Probe = 30KV:10 pA | Stage at T = 0.0 °
20 µm | | Pixel Size = 572.9 nm | EHT = 15.00 kV | ESB Grid = 0 V | FIB Milling Probe = 30KV:200 pA | Tilt Corrn. = Off

Sanded – Dry – H$_2$ — **3 days**

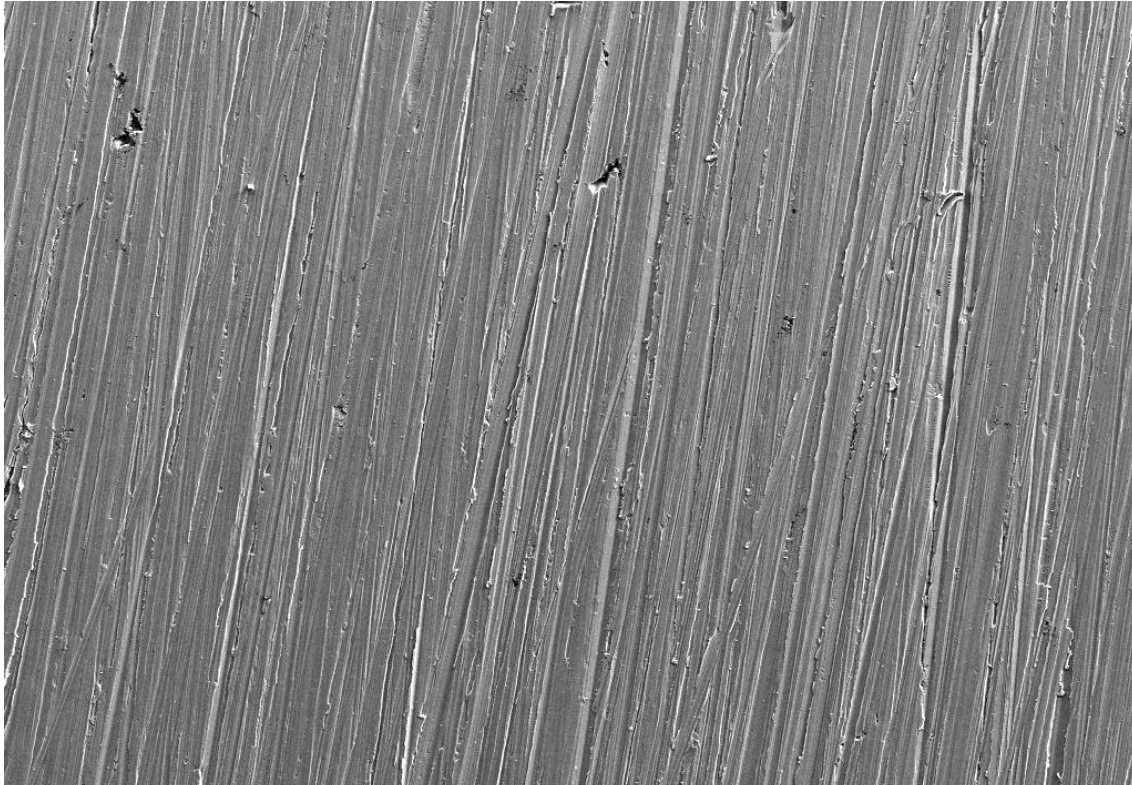SEM · 20 µm · Mag = 200 X · Width = 586.7 µm · WD = 4.0 mm · Signal A = SE2 · FIB Probe = 30KV:10 pA · Stage at T = 0.0 °
Pixel Size = 572.9 nm · EHT = 15.00 kV · ESB Grid = 0 V · FIB Milling Probe = 30KV:200 pA · Tilt Corrn. = Off

Sanded – Dry – N$_2$ — **3 days**

SEM · 20 µm · Mag = 200 X · Width = 586.7 µm · WD = 4.0 mm · Signal A = SE2 · FIB Probe = 30KV:10 pA · Stage at T = 0.0 °
Pixel Size = 572.9 nm · EHT = 15.00 kV · ESB Grid = 0 V · FIB Milling Probe = 30KV:200 pA · Tilt Corrn. = Off
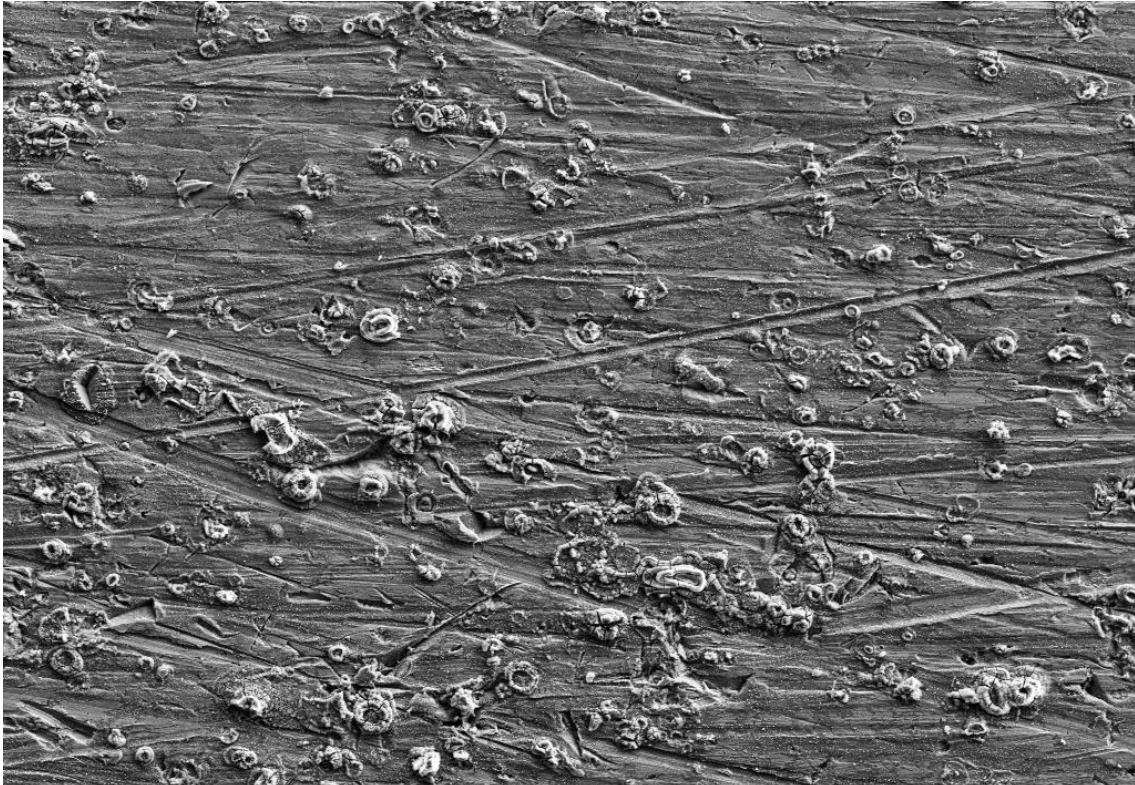
SEM
20 μm
| Mag = 200 X | Width = 586.7 μm | WD = 4.0 mm | Signal A = SE2 | FIB Probe = 30KV:10 pA | Stage at T = 0.0 ° |
| Pixel Size = 572.9 nm | EHT = 15.00 kV | ESB Grid = 0 V | FIB Milling Probe = 30KV:200 pA | Tilt Corrn. = Off |

SEM
20 μm
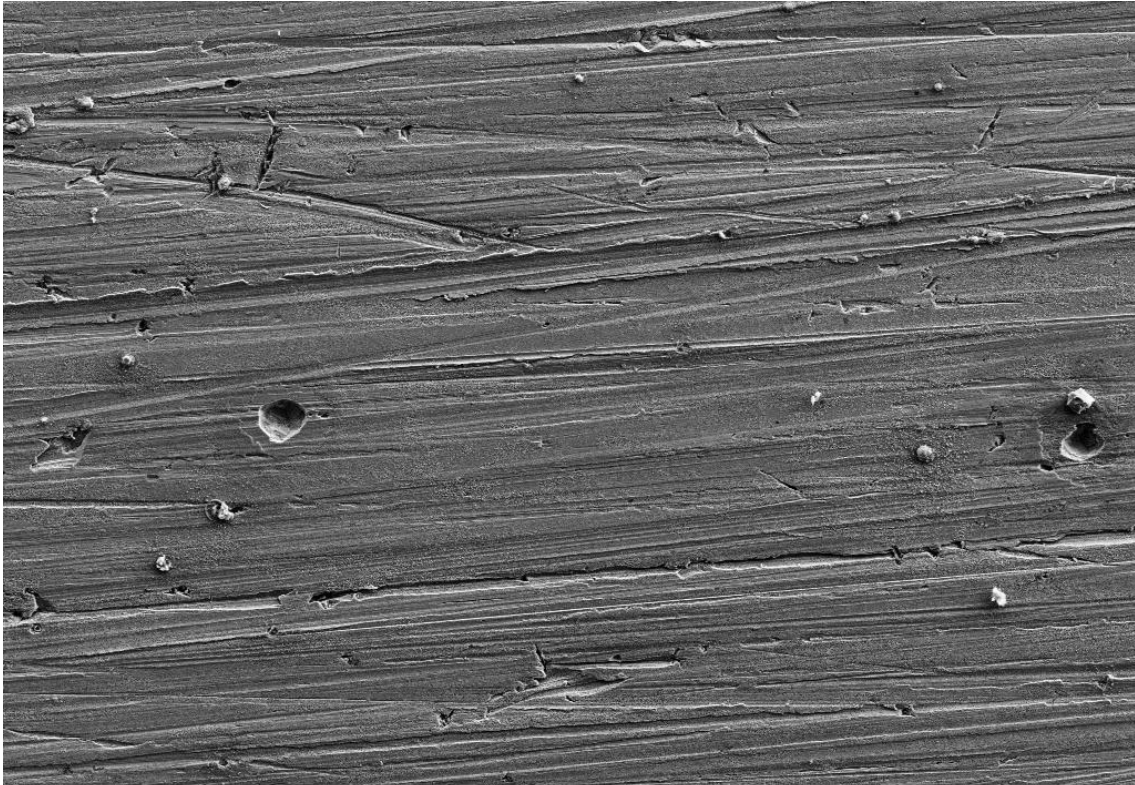| Mag = 200 X | Width = 586.7 μm | WD = 4.0 mm | Signal A = SE2 | FIB Probe = 30KV:10 pA | Stage at T = 0.0 ° |
| Pixel Size = 572.9 nm | EHT = 15.00 kV | ESB Grid = 0 V | FIB Milling Probe = 30KV:200 pA | Tilt Corrn. = Off |

Sanded – Brine – H$_2$ 3 days

| SEM | Mag = 200 X | Width = 586.7 μm | WD = 4.0 mm | Signal A = SE2 | FIB Probe = 30KV:10 pA | Stage at T = 0.0 ° |
| 20 μm | | Pixel Size = 572.9 nm | EHT = 15.00 kV | ESB Grid = 0 V | FIB Milling Probe = 30KV:200 pA | Tilt Corrn. = Off |

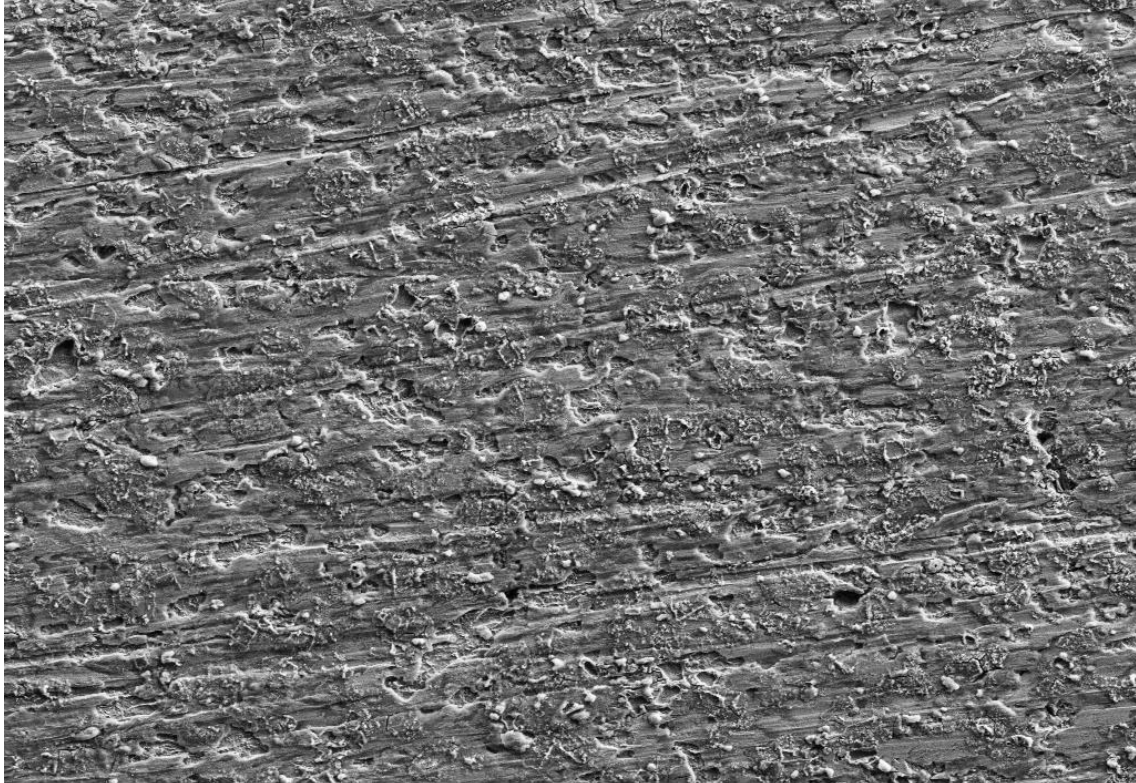**Sanded – Brine – N$_2$** 3 days

| SEM | Mag = 200 X | Width = 586.7 μm | WD = 4.0 mm | Signal A = SE2 | FIB Probe = 30KV:10 pA | Stage at T = 0.0 ° |
| 20 μm | | Pixel Size = 572.9 nm | EHT = 15.00 kV | ESB Grid = 0 V | FIB Milling Probe = 30KV:200 pA | Tilt Corrn. = Off |

| SEM | Mag = 200 X | Width = 586.7 µm | WD = 4.0 mm | Signal A = SE2 | FIB Probe = 30KV:10 pA | Stage at T = 0.0 ° |
| 20 µm | | Pixel Size = 572.9 nm | EHT = 15.00 kV | ESB Grid = 0 V | FIB Milling Probe = 30KV:200 pA | Tilt Corrn. = Off |

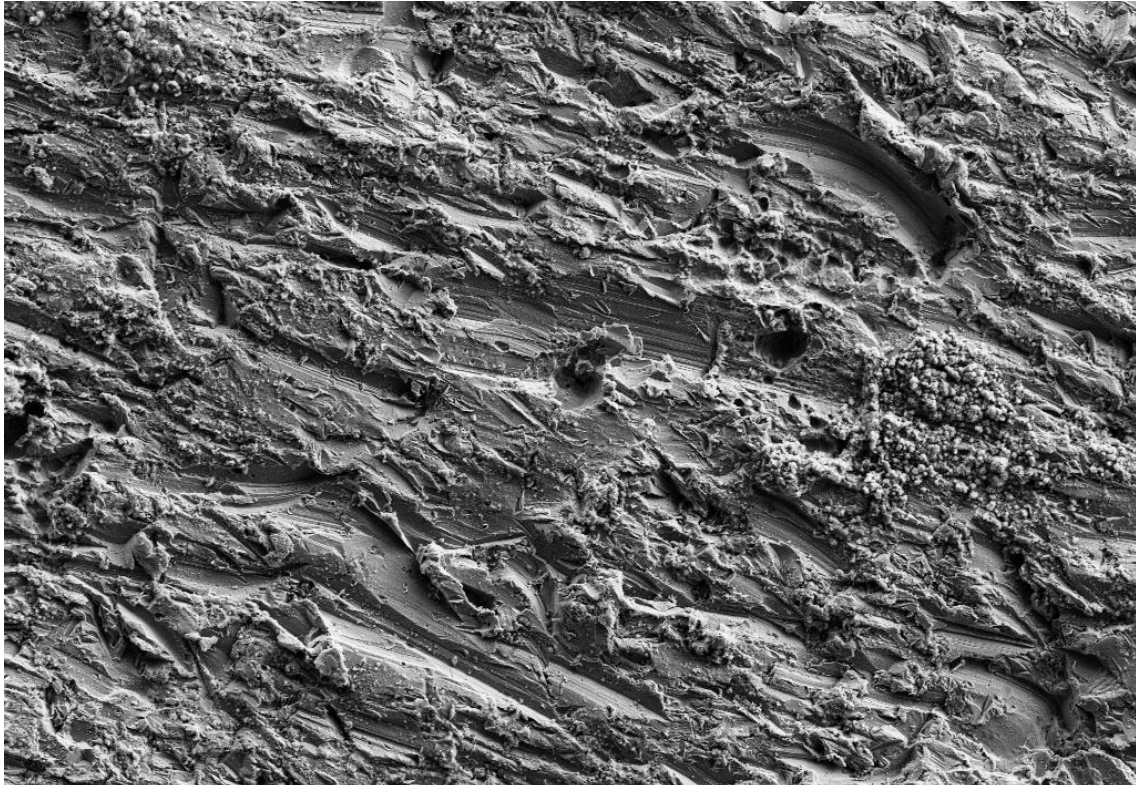| SEM | Mag = 200 X | Width = 586.7 µm | WD = 4.0 mm | Signal A = SE2 | FIB Probe = 30KV:10 pA | Stage at T = 0.0 ° |
| 20 µm | | Pixel Size = 572.9 nm | EHT = 15.00 kV | ESB Grid = 0 V | FIB Milling Probe = 30KV:200 pA | Tilt Corrn. = Off |

Sanded – Gas – H₂ — **14 days**

SEM | Mag = 200 X | Width = 586.7 µm | WD = 4.0 mm | Signal A = SE2 | FIB Probe = 30KV:10 pA | Stage at T = 0.0 °
20 µm | Pixel Size = 572.9 nm | EHT = 15.00 kV | ESB Grid = 0 V | FIB Milling Probe = 30KV:200 pA | Tilt Corrn. = Off
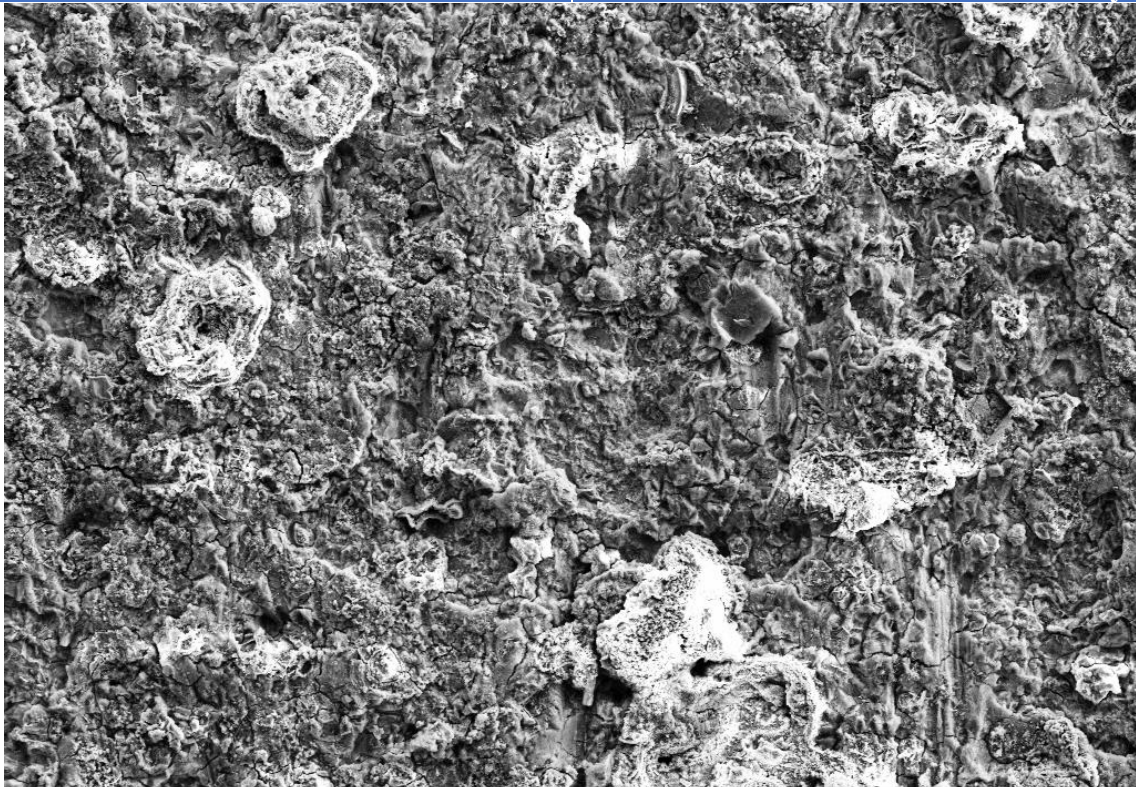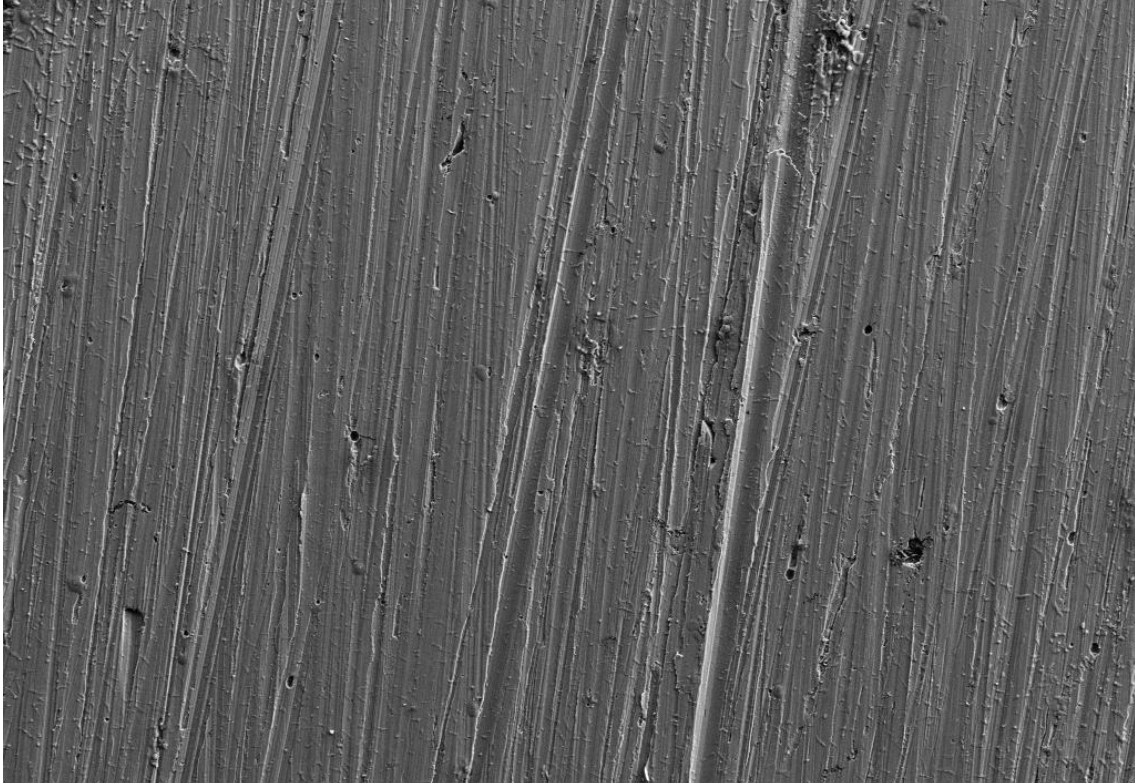

Sanded – Brine – H₂ — **14 days**

SEM | Mag = 200 X | Width = 586.7 µm | WD = 4.0 mm | Signal A = SE2 | FIB Probe = 30KV:10 pA | Stage at T = 0.0 °
20 µm | Pixel Size = 572.9 nm | EHT = 15.00 kV | ESB Grid = 0 V | FIB Milling Probe = 30KV:200 pA | Tilt Corrn. = Off

SEM - H₂-ready X56 steel provided by Mannesmann Line Pipe GmbH

SEM - H_2-ready X56 steel provided by Mannesmann Line Pipe GmbH

The SEM images of all X56 specimen with 200X magnification are presented in this subsection. In the main text it was explained that the EDX results and the frequency of cracking occurrences show no clear difference between the specimen exposed to hydrogen gas and nitrogen gas. Comparing the images for all conditions, it becomes clear that there might still be differences. The specimen exposed to brine and hydrogen show more salt formations on the surface after the washing process than the specimen exposed to nitrogen. This is in accordance with the EDX results. The reason has not been studied. However, as similar iron and oxide values were found, this is no indication for stronger degradation of the material due to hydrogen exposure. Nevertheless, there still might be a difference which should be studied. The recommended mechanical test would provide clarity.
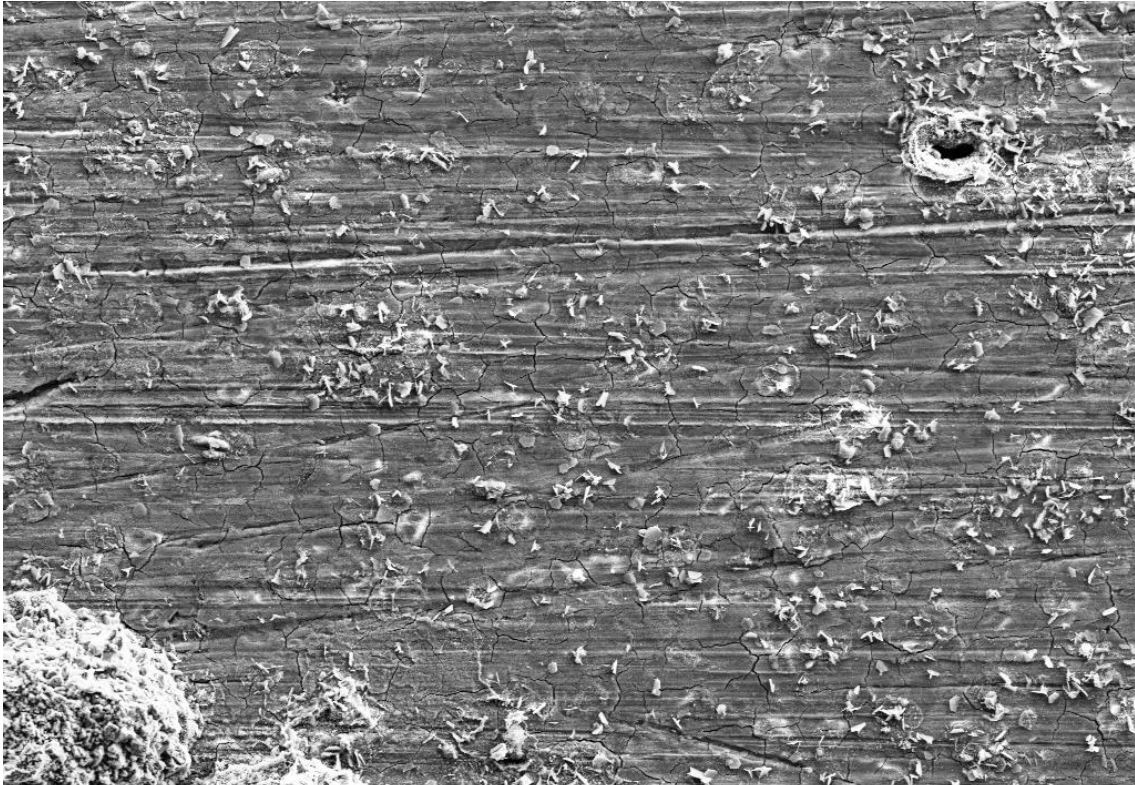
SEM | Mag = 200 X | Width = 586.7 μm | WD = 4.0 mm | Signal A = SE2 | FIB Probe = 30KV:10 pA | Stage at T = 0.0 °
20 μm | | Pixel Size = 572.9 nm | EHT = 15.00 kV | ESB Grid = 0 V | FIB Milling Probe = 30KV:200 pA | Tilt Corrn. = Off

SEM | Mag = 200 X | Width = 586.7 μm | WD = 4.0 mm | Signal A = SE2 | FIB Probe = 30KV:10 pA | Stage at T = 0.0 °
20 μm | | Pixel Size = 572.9 nm | EHT = 15.00 kV | ESB Grid = 0 V | FIB Milling Probe = 30KV:200 pA | Tilt Corrn. = Off

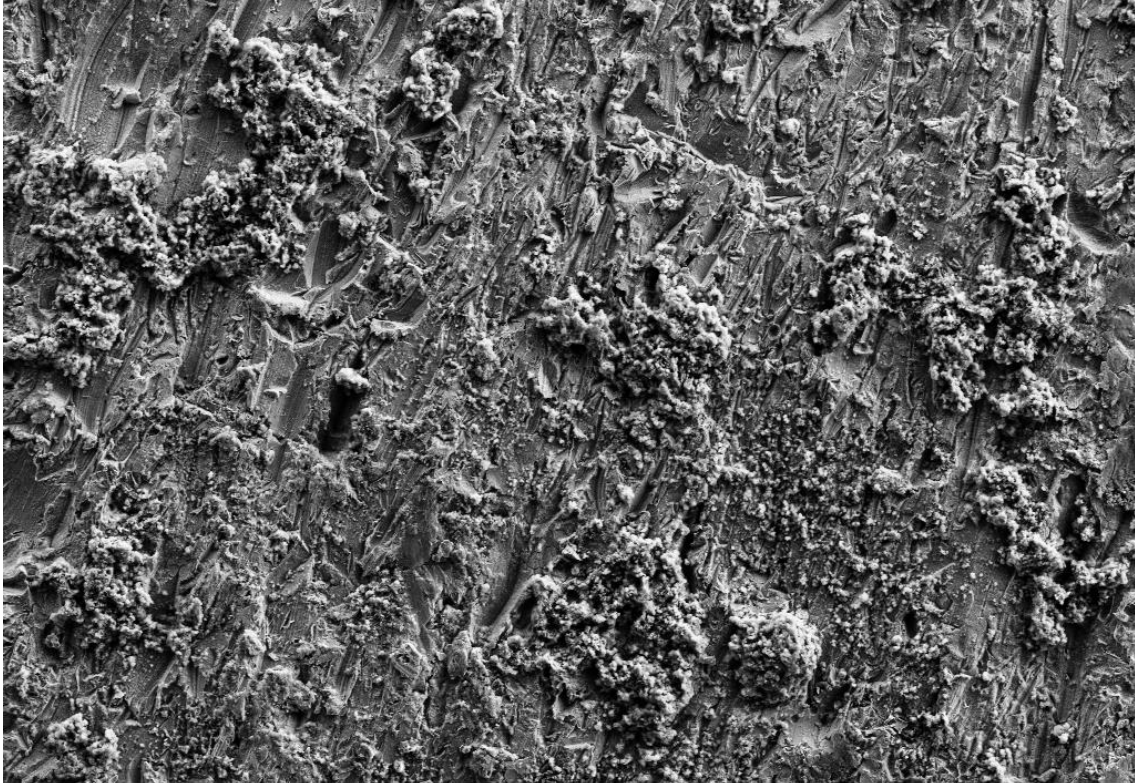SEM   Mag = 200 X   Width = 586.7 µm   WD = 4.0 mm   Signal A = SE2   FIB Probe = 30KV:10 pA   Stage at T = 0.0 °
20 µm   Pixel Size = 572.9 nm   EHT = 15.00 kV   ESB Grid = 0 V   FIB Milling Probe = 30KV:200 pA   Tilt Corrn. = Off

SEM   Mag = 200 X   Width = 586.7 µm   WD = 4.0 mm   Signal A = SE2   FIB Probe = 30KV:10 pA   Stage at T = 0.0 °
20 µm   Pixel Size = 572.9 nm   EHT = 15.00 kV   ESB Grid = 0 V   FIB Milling Probe = 30KV:200 pA   Tilt Corrn. = Off

Untreated – Brine – H$_2$ **3 days**

SEM | Mag = 200 X | Width = 589.6 μm | WD = 4.0 mm | Signal A = SE2 | FIB Probe = 30KV:10 pA | Stage at T = 0.0 °
20 μm | | Pixel Size = 575.8 nm | EHT = 15.00 kV | ESB Grid = 0 V | FIB Milling Probe = 30KV:200 pA | Tilt Corrn. = Off

Untreated – Brine – N$_2$ **3 days**

SEM | Mag = 200 X | Width = 586.7 μm | WD = 4.0 mm | Signal A = SE2 | FIB Probe = 30KV:10 pA | Stage at T = 0.0 °
20 μm | | Pixel Size = 572.9 nm | EHT = 15.00 kV | ESB Grid = 0 V | FIB Milling Probe = 30KV:200 pA | Tilt Corrn. = Off
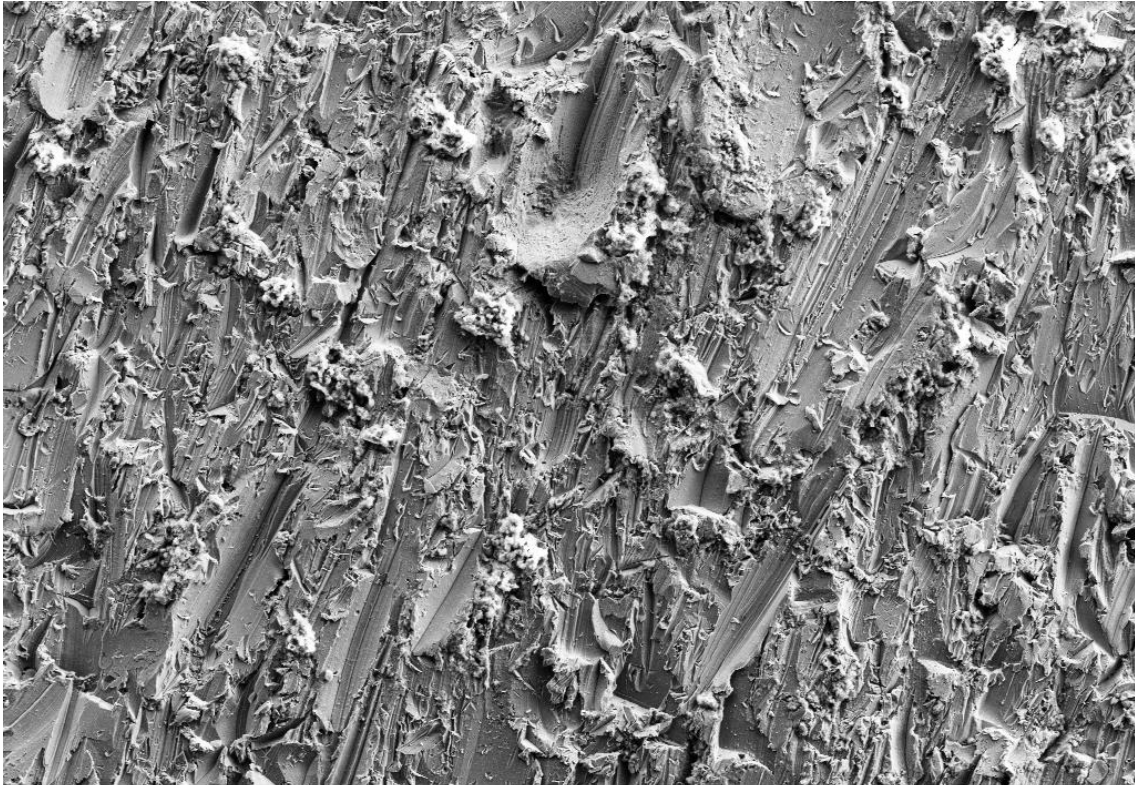
Sanded – Dry – H$_2$ **3 days**

SEM | Mag = 200 X | Width = 586.7 µm | WD = 4.0 mm | Signal A = SE2 | FIB Probe = 30KV:10 pA | Stage at T = 0.0 °
20 µm | | Pixel Size = 572.9 nm | EHT = 15.00 kV | ESB Grid = 0 V | FIB Milling Probe = 30KV:200 pA | Tilt Corrn. = Off
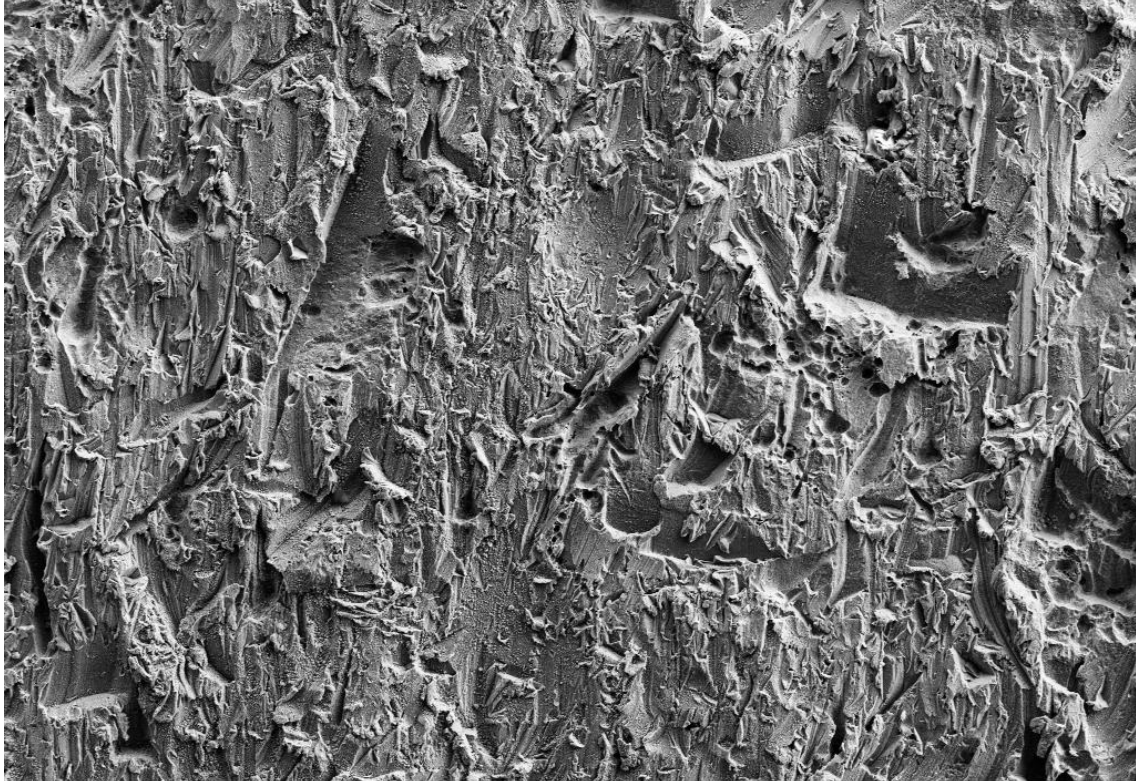

Sanded – Dry – N$_2$ **3 days**

SEM | Mag = 200 X | Width = 586.7 µm | WD = 4.0 mm | Signal A = SE2 | FIB Probe = 30KV:10 pA | Stage at T = 0.0 °
20 µm | | Pixel Size = 572.9 nm | EHT = 15.00 kV | ESB Grid = 0 V | FIB Milling Probe = 30KV:200 pA | Tilt Corrn. = Off

Sanded – Water – H$_2$ — **3 days**

SEM | Mag = 200 X | Width = 586.7 µm | WD = 4.0 mm | Signal A = SE2 | FIB Probe = 30KV:10 pA | Stage at T = 0.0 °
20 µm | | Pixel Size = 572.9 nm | EHT = 15.00 kV | ESB Grid = 0 V | FIB Milling Probe = 30KV:200 pA | Tilt Corrn. = Off

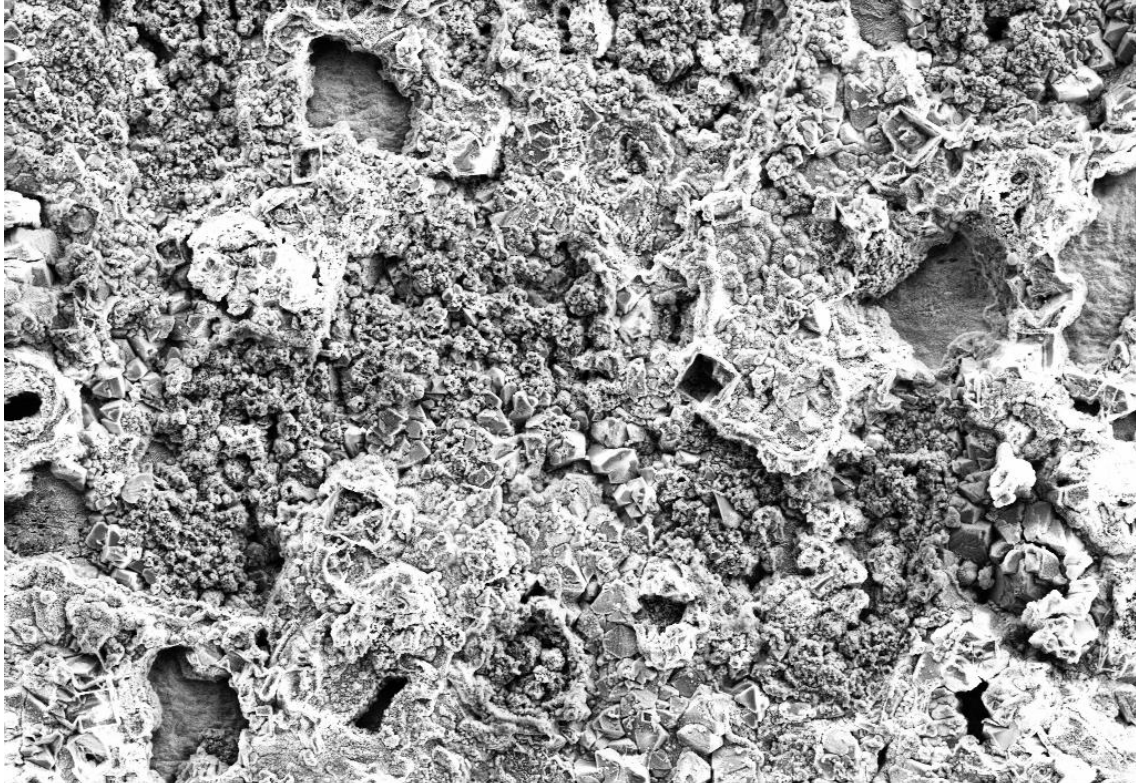**Sanded – Water – N$_2$** — **3 days**

SEM | Mag = 200 X | Width = 586.7 µm | WD = 4.0 mm | Signal A = SE2 | FIB Probe = 30KV:10 pA | Stage at T = 0.0 °
20 µm | | Pixel Size = 572.9 nm | EHT = 15.00 kV | ESB Grid = 0 V | FIB Milling Probe = 30KV:200 pA | Tilt Corrn. = Off

| SEM | Mag = 200 X | Width = 586.7 µm | WD = 4.0 mm | Signal A = SE2 | FIB Probe = 30KV:10 pA | Stage at T = 0.0 ° |
| 20 µm | Pixel Size = 572.9 nm | EHT = 15.00 kV | ESB Grid = 0 V | FIB Milling Probe = 30KV:200 pA | Tilt Corrn. = Off |

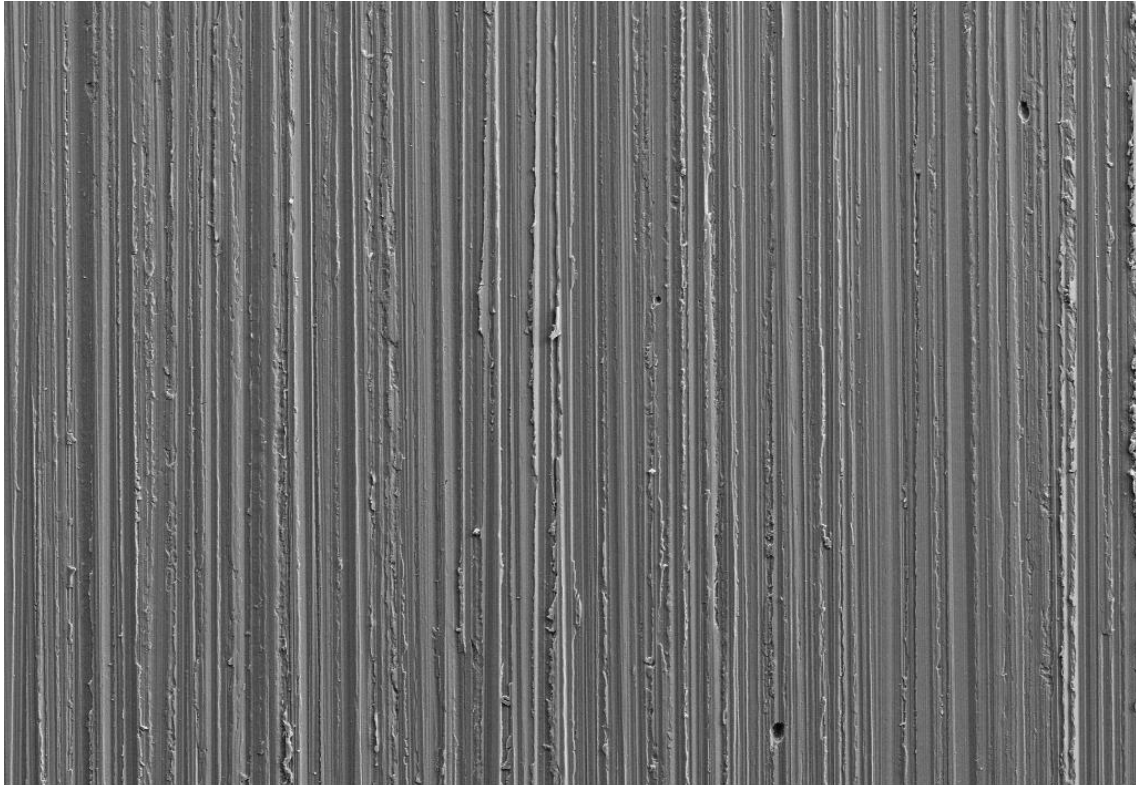| SEM | Mag = 200 X | Width = 586.7 µm | WD = 4.0 mm | Signal A = SE2 | FIB Probe = 30KV:10 pA | Stage at T = 0.0 ° |
| 20 µm | Pixel Size = 572.9 nm | EHT = 15.00 kV | ESB Grid = 0 V | FIB Milling Probe = 30KV:200 pA | Tilt Corrn. = Off |
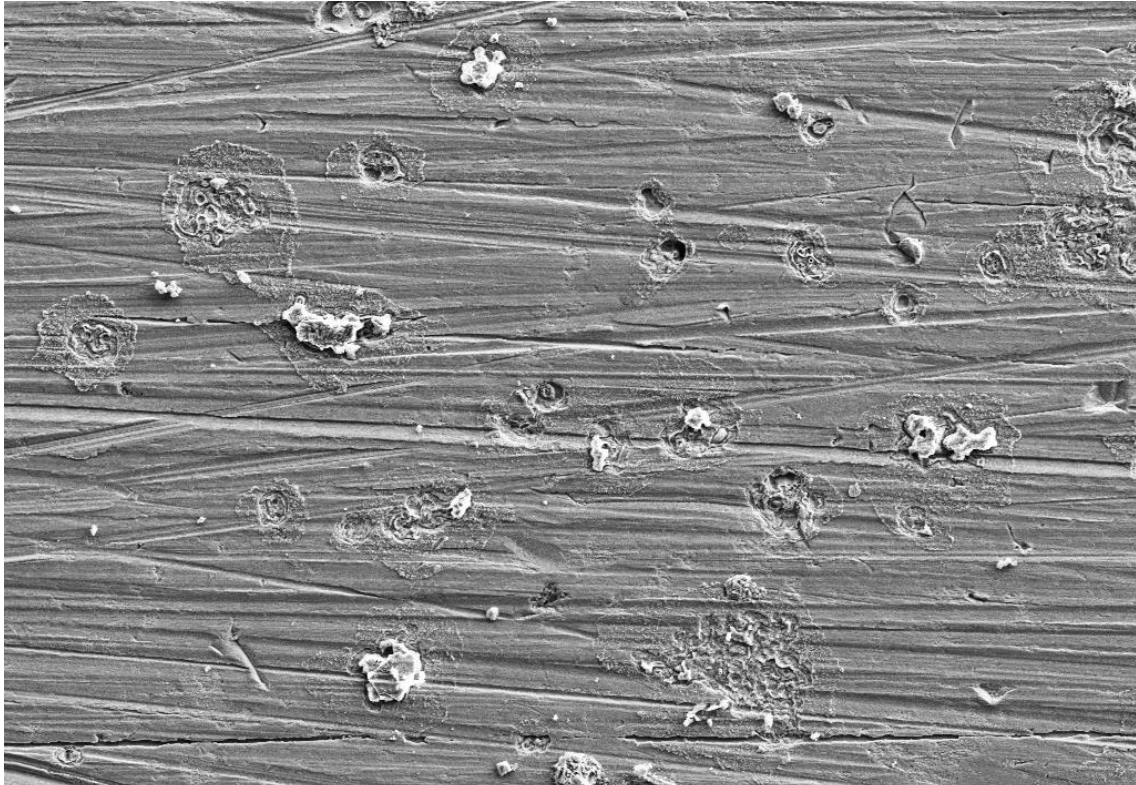
Untreated – Dry – H₂   **14 days**
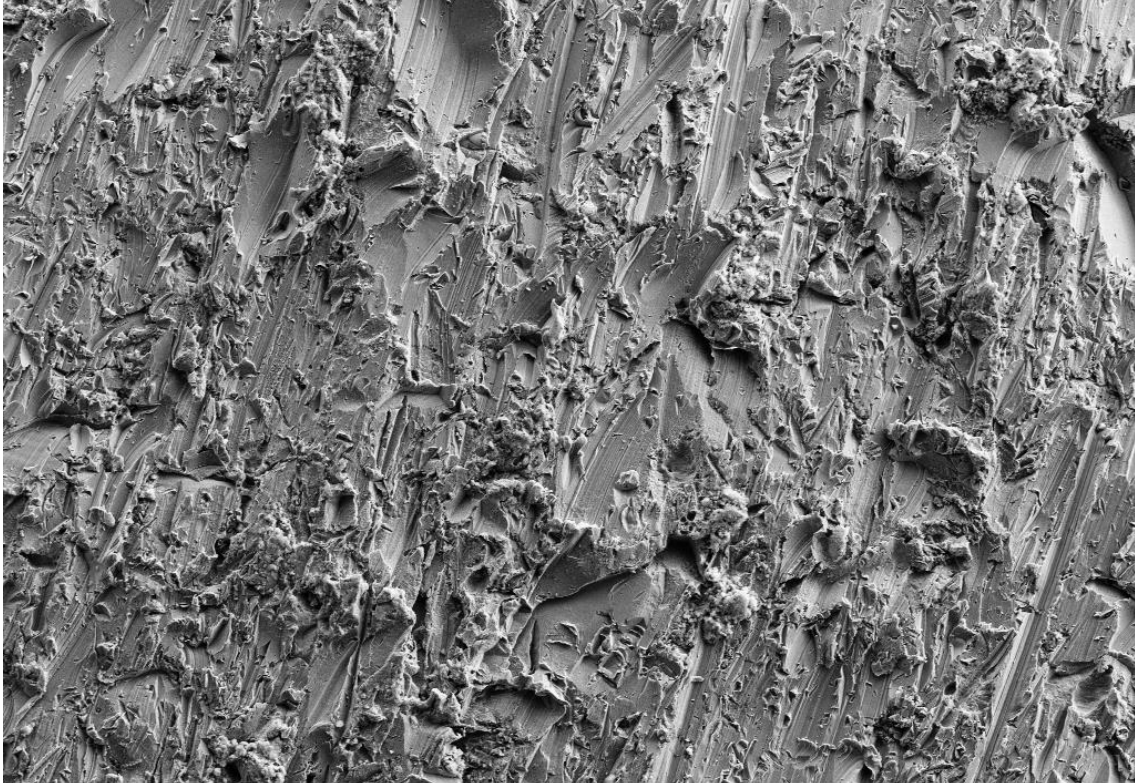
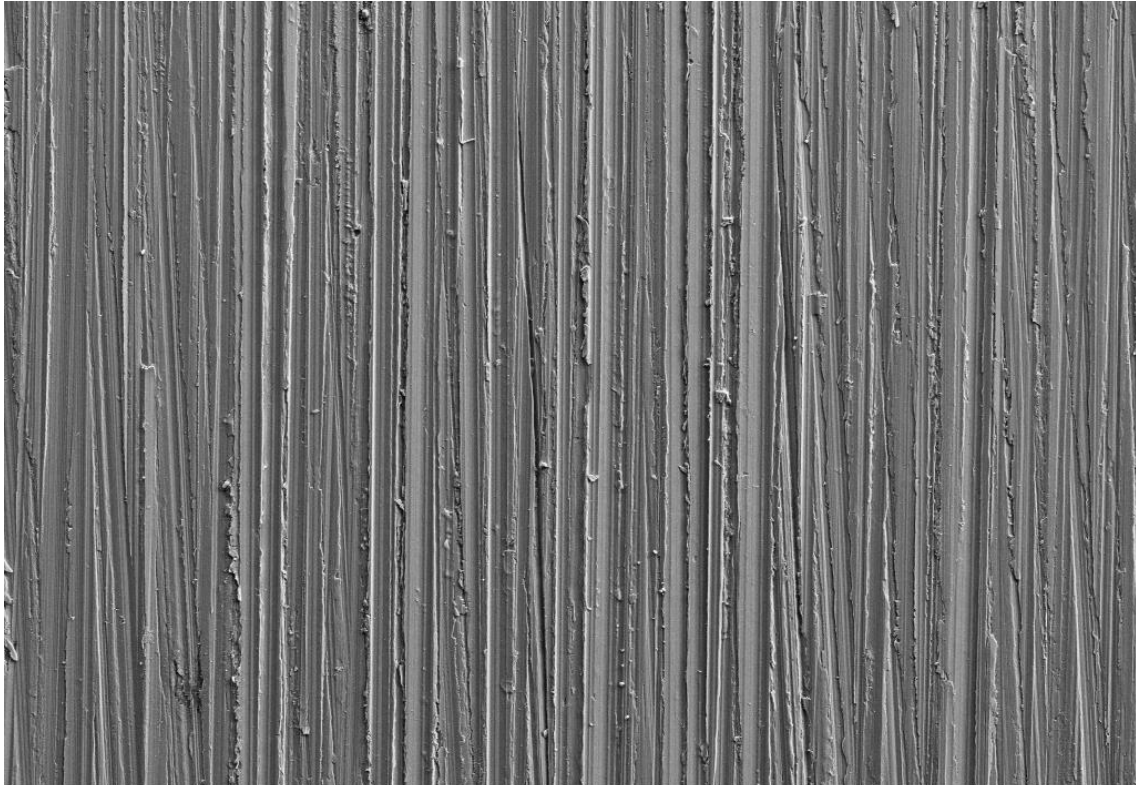| SEM | Mag = 200 X | Width = 586.7 µm | WD = 4.0 mm | Signal A = SE2 | FIB Probe = 30KV:10 pA | Stage at T = 0.0 ° |
| 20 µm | | Pixel Size = 572.9 nm | EHT = 15.00 kV | ESB Grid = 0 V | FIB Milling Probe = 30KV:200 pA | Tilt Corrn. = Off |

Untreated – Brine – H₂   **14 days**

| SEM | Mag = 200 X | Width = 586.7 µm | WD = 4.0 mm | Signal A = SE2 | FIB Probe = 30KV:10 pA | Stage at T = -0.0 ° |
| 20 µm | | Pixel Size = 572.9 nm | EHT = 15.00 kV | ESB Grid = 0 V | FIB Milling Probe = 30KV:200 pA | Tilt Corrn. = Off |

Sanded – Dry – H₂

14 days

SEM | Mag = 200 X | Width = 586.7 µm | WD = 4.0 mm | Signal A = SE2 | FIB Probe = 30KV:10 pA | Stage at T = 0.0 °
20 µm | | Pixel Size = 572.9 nm | EHT = 15.00 kV | ESB Grid = 0 V | FIB Milling Probe = 30KV:200 pA | Tilt Corrn. = Off
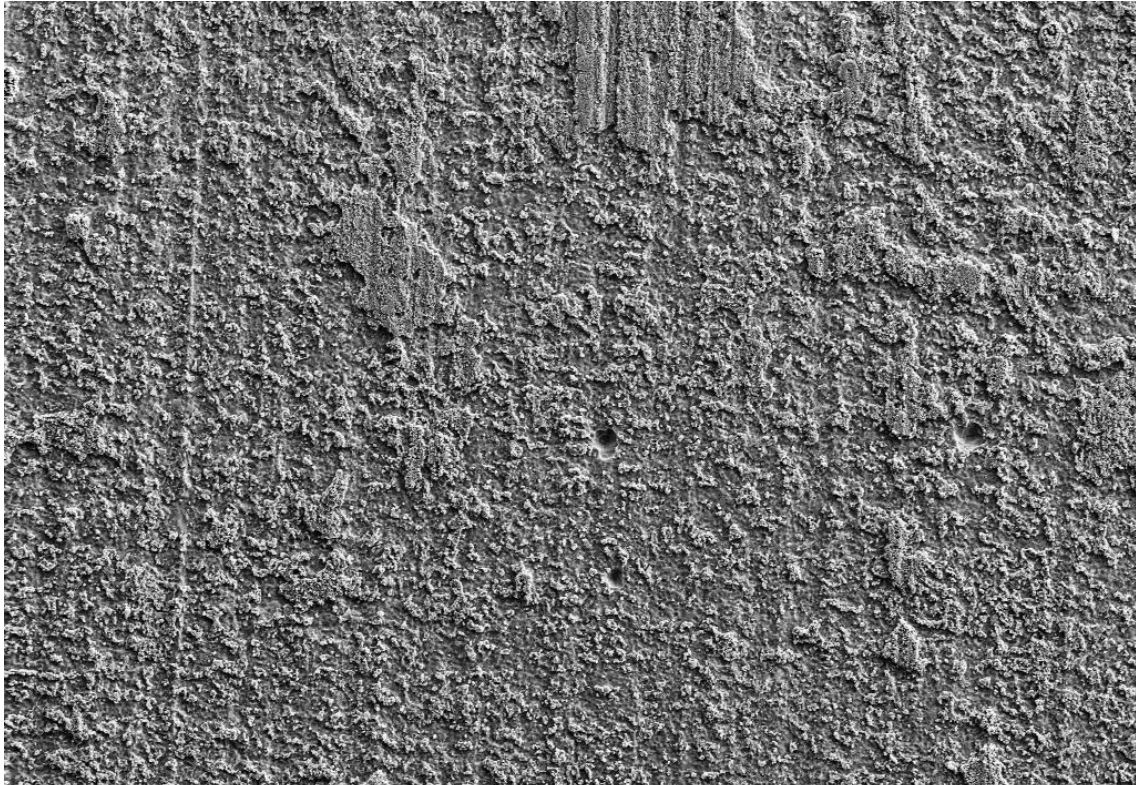
Sanded – Brine – H₂

14 days

SEM | Mag = 200 X | Width = 586.7 µm | WD = 4.0 mm | Signal A = SE2 | FIB Probe = 30KV:10 pA | Stage at T = 0.0 °
20 µm | | Pixel Size = 572.9 nm | EHT = 15.00 kV | ESB Grid = 0 V | FIB Milling Probe = 30KV:200 pA | Tilt Corrn. = Off
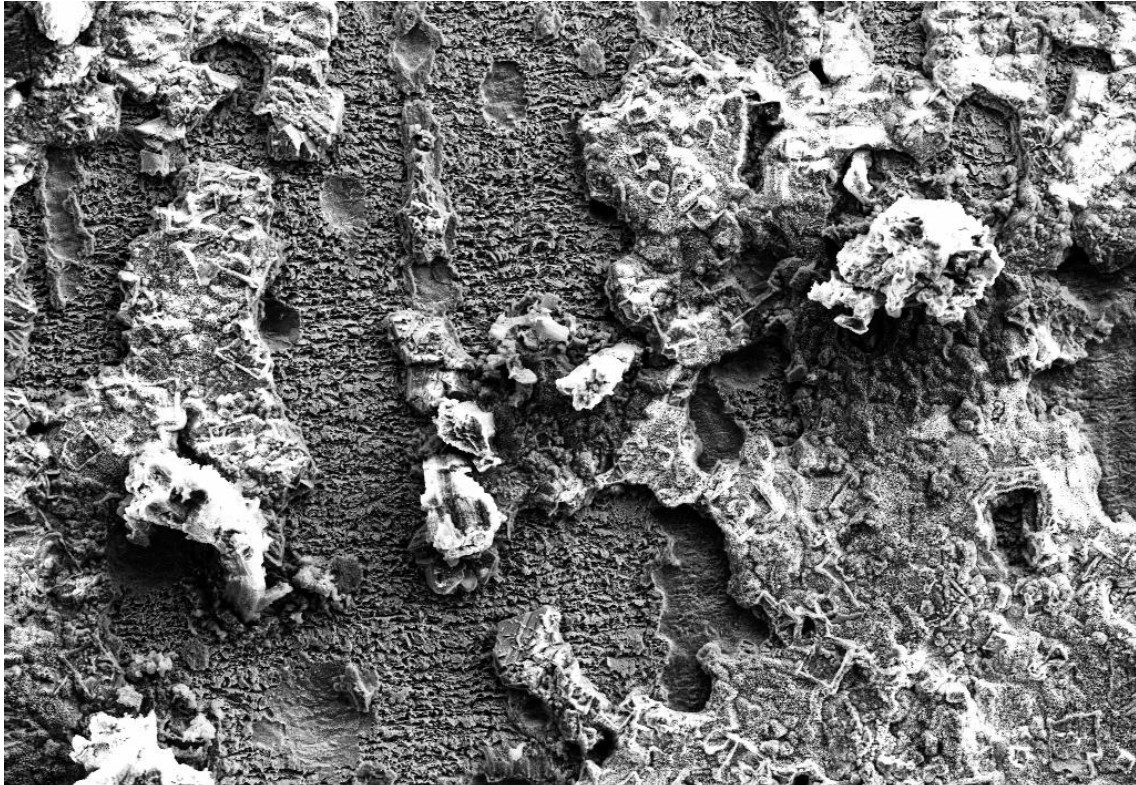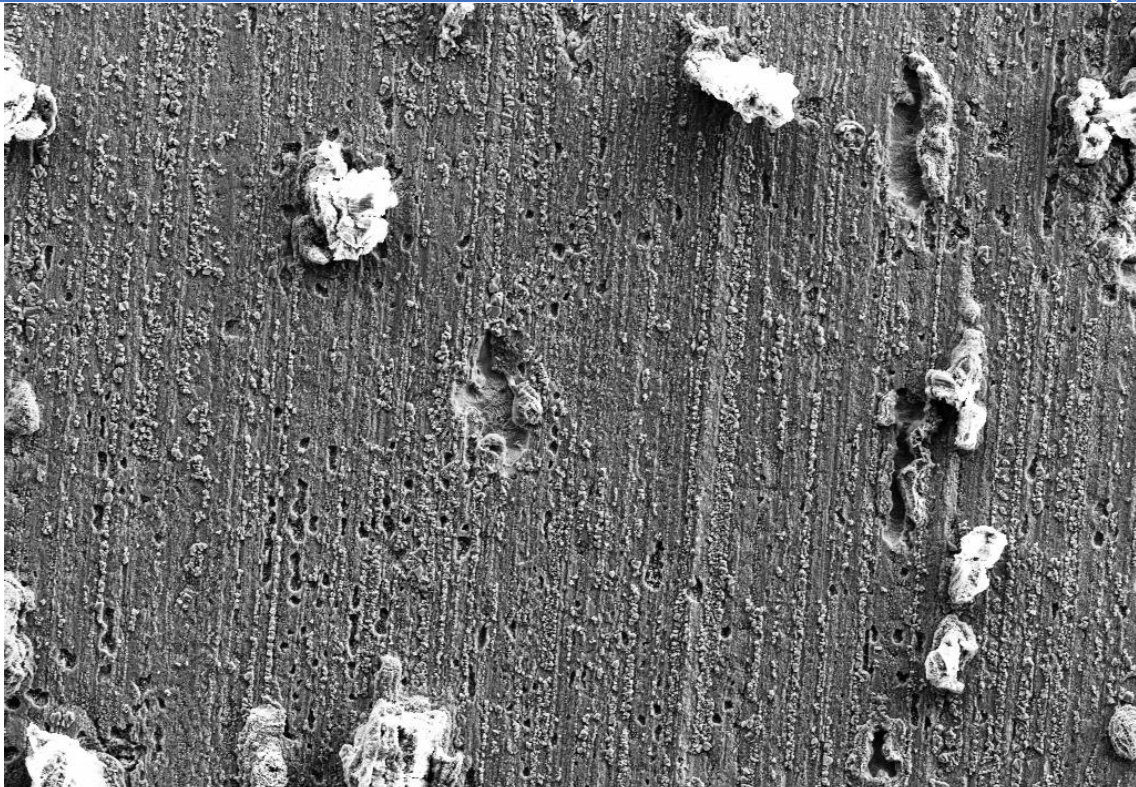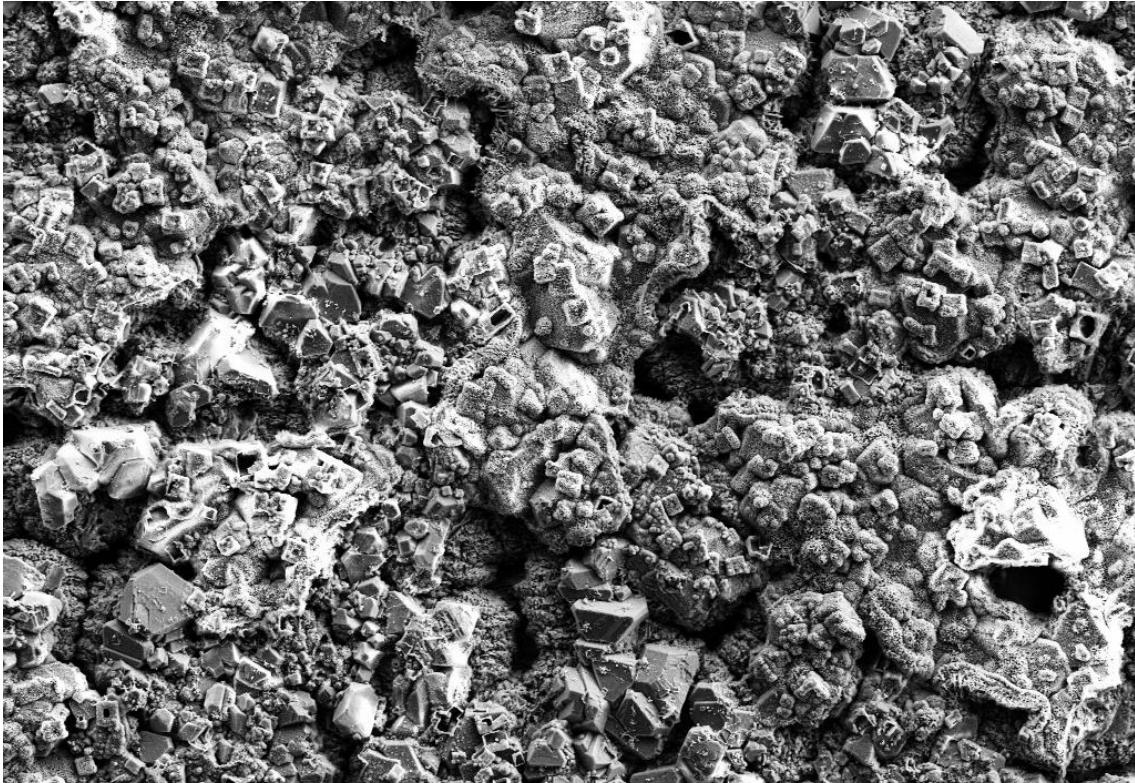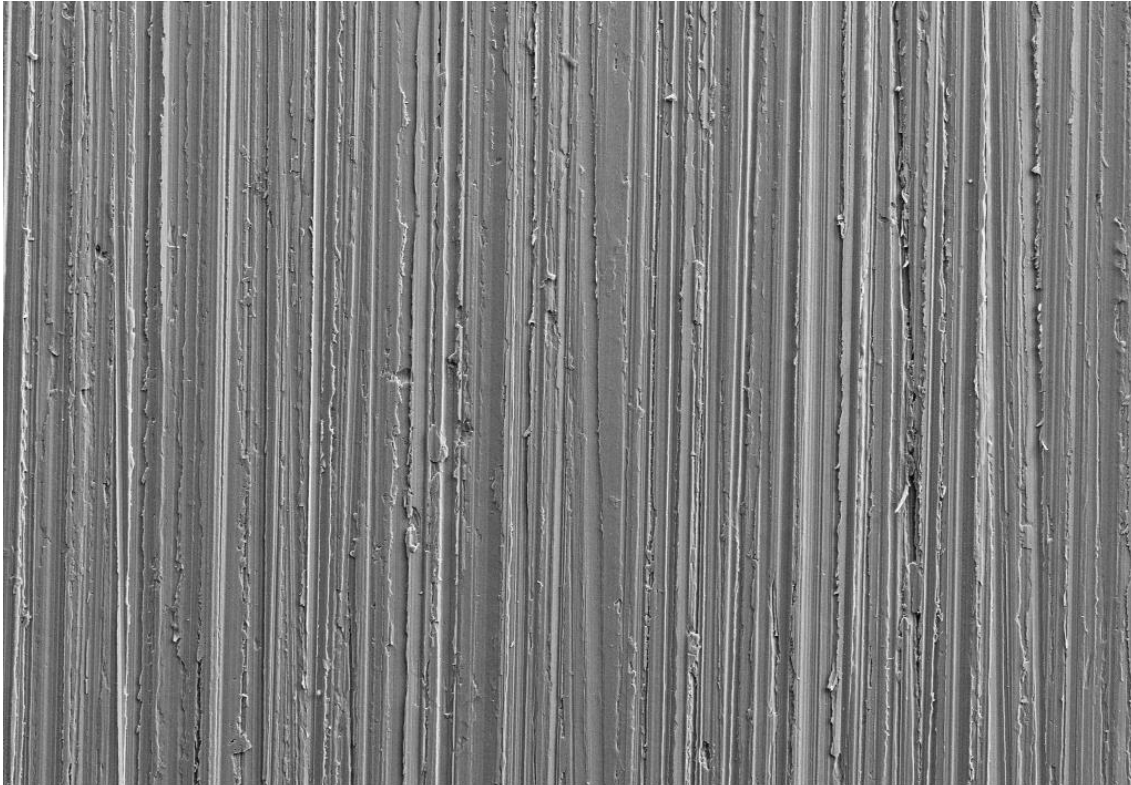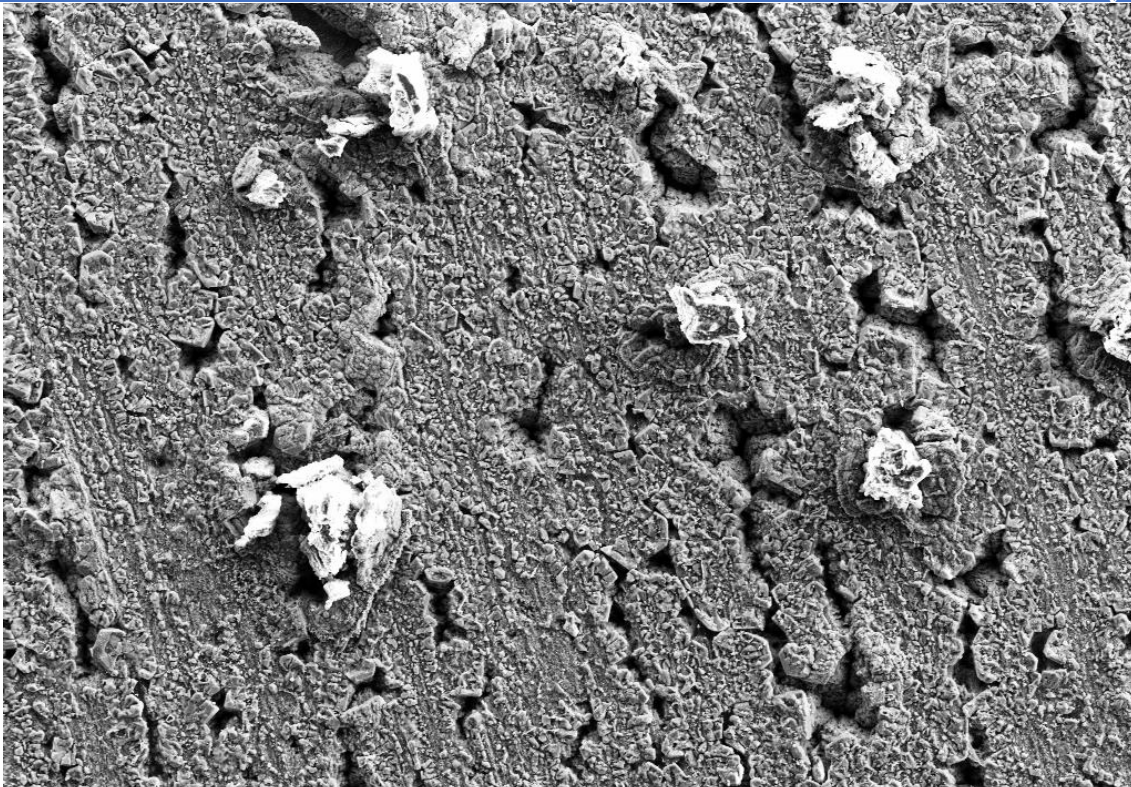
Appendix C – J55 coating

On top of the J55 exterior, a coating is applied. Since the coating potentially reacted in the experimental conditions, a characterisation is relevant. In the SEM two layers are visible. The inner layer is shown in Figure 43a and has a thickness of approximately 128 µm. The thickness was measured with the SEM software. The categorisation of the layer was conducted by comparison of the SEM images and EDX values with typical anti-corrosion coating. One coating, zinc-rich paint (ZRP), has been applied for over a century already [80]. Many different compositions exist which makes it difficult to assign an unknown ZRP to the specific paint. However, that kind of assignment is not relevant for this work and was not approached. By recording EDX data of the layer and comparison to literature values for one ZRP in Table 11, similarities were found indicating the coating to be a ZRP. The comparison of Figure 43a with Figure 44 further supports the categorisation but also clearly indicates differences in the ZRP, which originate from the different chemical composition.

The top layer is shown in Figure 43b and has a thickness of approximately 210 µm. The SEM image clearly shows charge effects indicating the top layer to be an insulator. EDX values were recorded and are listed in Table 12, suggesting the outer layer to be a carbon-based anti-corrosion coat. Carbon based coating are applied in technological applications since the 1990s as protection against corrosion, wear and tear effects [81]. Therefore, lots of experience was gained throughout the years and multiple coatings based on carbon were developed.
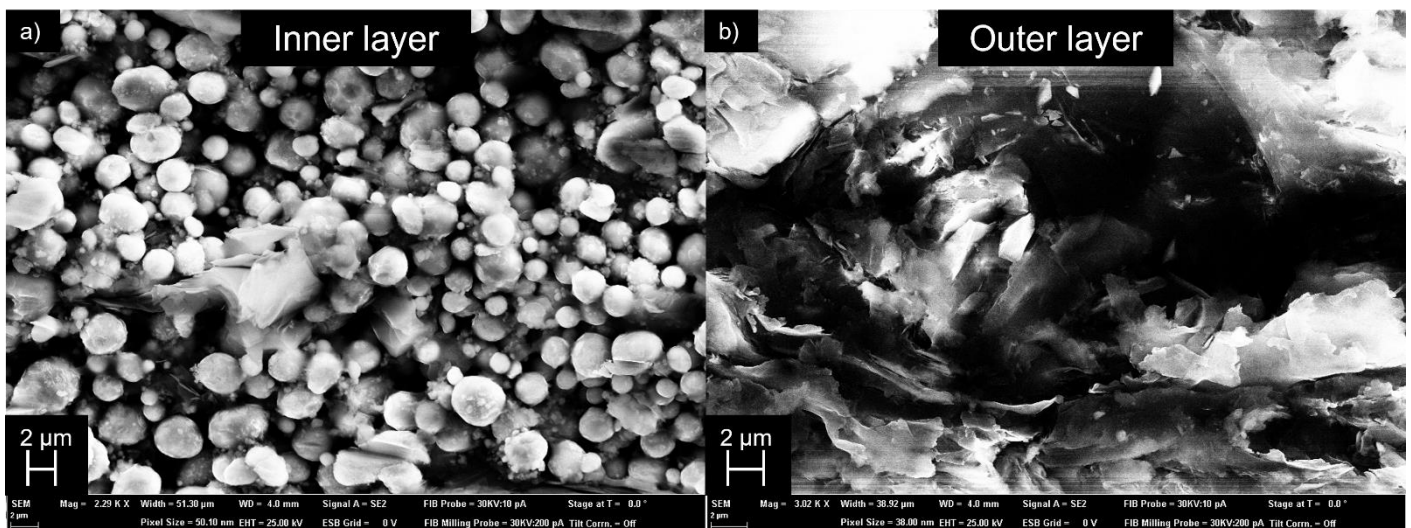
Figure 43: SEM images of two coating layers on exterior of J55 steel specimens. a) inner layer and b) outer layer.

Table 11: Measured EDX values for inner coating compared to EDX values for zinc-rich paint from literature in wt. %.

	Inner coating layer /wt. %	ZRP [82]/ wt. %
C	16.53	39.09
O	18.28	8.12
Mg	1.68	0.8
Si	4.09	1.71
Cr	3.75	-
Fe	0.93	-
Zn	54.73	49.86
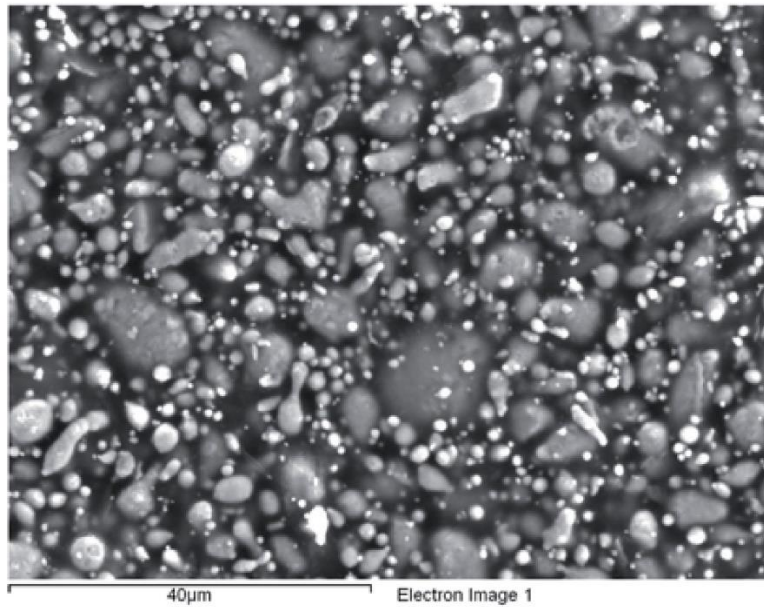
Figure 44: SEM image of ZRP from literature [82].

Table 12: EDX data of outer coating layer in wt. %.

	Outer coating layer / wt. %
C	53.73
O	28.11
Mg	3.35
Al	6.98
Si	4.41
K	0.21
Fe	3.20

Appendix D - Tables and Figures

API norms

Each type of steel has its own specific requirements which need to be fulfilled to qualify for the naming. In this work API 5L and API 5CT steels were investigated. In the following figures are the requirements on chemical composition and tensile properties for both steel categories shown. Particular focus is on J55 and X56, as the steels investigated fall in these requirements. It can be seen, the 5CT steels (Figure 45 and Figure 46) do not have strict rules for the chemical composition. Among similar steel types like for instance K55, no difference can be found. However, the differentiation is made by the tensile strength. For 5L steel more rules for the chemical composition exist, this said, within the 5L classification there are not to only small variations (Figure 47). The differentiation is made over the yield strength (Figure 48)

Grade	Type	C min	C max	Mn min	Mn max	Mo min	Mo max	Cr min	Cr max	Ni max	Cu max	P max	S max	Si max
1	2	3	4	5	6	7	8	9	10	11	12	13	14	15
H40	—	—	—	—	—	—	—	—	—	—	—	0.030	0.030	—
J55	—	—	—	—	—	—	—	—	—	—	—	0.030	0.030	—
K55	—	—	—	—	—	—	—	—	—	—	—	0.030	0.030	—
N80	1	—	—	—	—	—	—	—	—	—	—	0.030	0.030	—
N80	Q	—	—	—	—	—	—	—	—	—	—	0.030	0.030	—
R95	—	—	0.45 [c]	—	1.90	—	—	—	—	—	—	0.030	0.030	0.45
L80	1	—	0.43 [a]	—	1.90	—	—	—	—	0.25	0.35	0.030	0.030	0.45
L80	9Cr	—	0.15	0.30	0.60	0.90	1.10	8.00	10.0	0.50	0.25	0.020	0.010	1.00
L80	13Cr	0.15	0.22	0.25	1.00	—	—	12.0	14.0	0.50	0.25	0.020	0.010	1.00
C90	1	—	0.35	—	1.20	0.25 [b]	0.85	—	1.50	0.99	—	0.020	0.010	—
T95	1	—	0.35	—	1.20	0.25 [d]	0.85	0.40	1.50	0.99	—	0.020	0.010	—
C110	—	—	0.35	—	1.20	0.25	1.00	0.40	1.50	0.99	—	0.020	0.005	—
P110	[e]	—	—	—	—	—	—	—	—	—	—	0.030 [e]	0.030 [e]	—
Q125	1	—	0.35		1.35	—	0.85	—	1.50	—	—	0.020	0.010	—

NOTE   Elements shown shall be reported in product analysis.

[a]   The carbon content for L80 may be increased up to 0.50 % maximum if the product is oil-quenched or polymer-quenched.

[b]   The molybdenum content for Grade C90 Type 1 has no minimum tolerance if the wall thickness is less than 17.78 mm.

[c]   The carbon content for R95 may be increased up to 0.55 % maximum if the product is oil-quenched.

[d]   The molybdenum content for T95 Type 1 may be decreased to 0.15 % minimum if the wall thickness is less than 17.78 mm.

[e]   For EW Grade P110, the phosphorus content shall be 0.020 % maximum and the sulfur content 0.010 % maximum.

Figure 45: Requirements on chemical composition of API 5CT steels in mass fraction (%), taken from API 5CT standard [46].

Grade	Type	Total Elongation Under Load %	Yield Strength MPa		Tensile Strength min MPa	Hardness [a,c] max		Specified Wall Thickness	Allowable Hardness Variation [b]
			min	max		HRC	HBW	mm	HRC
1	2	3	4	5	6	7	8	9	10
H40	—	0.5	276	552	414	—	—	—	—
J55	—	0.5	379	552	517	—	—	—	—
K55	—	0.5	379	552	655	—	—	—	—
N80	1	0.5	552	758	689	—	—	—	—
N80	Q	0.5	552	758	689	—	—	—	—
R95	—	0.5	655	758	724	—	—	—	—
L80	1	0.5	552	655	655	23.0	241	—	—
L80	9Cr	0.5	552	655	655	23.0	241	—	—
L80	13Cr	0.5	552	655	655	23.0	241	—	—
C90	1	0.5	621	724	689	25.4	255	≤12.70	3.0
								12.71 to 19.04	4.0
								19.05 to 25.39	5.0
								≥ 25.40	6.0
T95	1	0.5	655	758	724	25.4	255	≤12.70	3.0
								12.71 to 19.04	4.0
								19.05 to 25.39	5.0
								≥ 25.40	6.0
C110	—	0.7	758	828	793	29.0	279	≤12.70	3.0
								12.71 to 19.04	4.0
								19.05 to 25.39	5.0
								≥ 25.40	6.0
P110	—	0.6	758	965	862	—	—	—	—
Q125	1	0.65	862	1034	931	b	—	≤12.70	3.0
								12.71 to 19.04	4.0
								≥19.05	5.0

a   In case of dispute, laboratory Rockwell C hardness testing shall be used as the referee method.

b   No hardness limits are specified, but the maximum variation is restricted as a manufacturing control in accordance with 7.8 and 7.9.

c   For through-wall hardness tests of Grades L80 (all types), C90, T95 and C110, the requirements stated in HRC scale are for maximum mean hardness number.

Figure 46: Requirements on tensile strength and hardness of API 5CT steels, taken from API 5CT standard [46].

Steel Grade (Steel Name)	Mass Fraction, Based on Heat and Product Analyses [a,g] %							
	C	Mn	P		S	V	Nb	Ti
	max [b]	max [b]	min	max	max	max	max	max
Seamless Pipe								
L175 or A25	0.21	0.60	—	0.030	0.030	—	—	—
L175P or A25P	0.21	0.60	0.045	0.080	0.030	—	—	—
L210 or A	0.22	0.90	—	0.030	0.030	—	—	—
L245 or B	0.28	1.20	—	0.030	0.030	[c,d]	[c,d]	[d]
L290 or X42	0.28	1.30	—	0.030	0.030	[d]	[d]	[d]
L320 or X46	0.28	1.40	—	0.030	0.030	[d]	[d]	[d]
L360 or X52	0.28	1.40	—	0.030	0.030	[d]	[d]	[d]
L390 or X56	0.28	1.40	—	0.030	0.030	[d]	[d]	[d]
L415 or X60	0.28 [e]	1.40 [e]	—	0.030	0.030	[f]	[f]	[f]
L450 or X65	0.28 [e]	1.40 [e]	—	0.030	0.030	[f]	[f]	[f]
L485 or X70	0.28 [e]	1.40 [e]	—	0.030	0.030	[f]	[f]	[f]
Welded Pipe								
L175 or A25	0.21	0.60	—	0.030	0.030	—	—	—
L175P or A25P	0.21	0.60	0.045	0.080	0.030	—	—	—
L210 or A	0.22	0.90	—	0.030	0.030	—	—	—
L245 or B	0.26	1.20	—	0.030	0.030	[c,d]	[c,d]	[d]
L290 or X42	0.26	1.30	—	0.030	0.030	[d]	[d]	[d]
L320 or X46	0.26	1.40	—	0.030	0.030	[d]	[d]	[d]
L360 or X52	0.26	1.40	—	0.030	0.030	[d]	[d]	[d]
L390 or X56	0.26	1.40	—	0.030	0.030	[d]	[d]	[d]
L415 or X60	0.26 [e]	1.40 [e]	—	0.030	0.030	[f]	[f]	[f]
L450 or X65	0.26 [e]	1.45 [e]	—	0.030	0.030	[f]	[f]	[f]
L485 or X70	0.26 [e]	1.65 [e]	—	0.030	0.030	[f]	[f]	[f]

[a] Cu ≤ 0.50 %; Ni ≤ 0.50 %; Cr ≤ 0.50 % and Mo ≤ 0.15 %.

[b] For each reduction of 0.01 % below the specified maximum concentration for carbon, an increase of 0.05 % above the specified maximum concentration for Mn is permissible, up to a maximum of 1.65 % for grades ≥ L245 or B, but ≤ L360 or X52; up to a maximum of 1.75 % for grades > L360 or X52, but < L485 or X70; and up to a maximum of 2.00 % for Grade L485 or X70.

[c] Unless otherwise agreed, Nb + V ≤ 0.06 %.

[d] Nb + V + Ti ≤ 0.15 %.

[e] Unless otherwise agreed.

[f] Unless otherwise agreed, Nb + V + Ti ≤ 0.15 %.

[g] No deliberate addition of B is permitted and the residual B ≤ 0.001 %.

Figure 47: Chemical composition requirements of API 5L steels for PSL 1 Pipe with t ≤25.0 mm, Figure taken from API 5L standard [43]

Pipe Grade	Pipe Body of Seamless and Welded Pipe			Weld Seam of EW, LW, SAW, and COW Pipe
	Yield Strength [a] $R_{t0.5}$ MPa (psi) min	Tensile Strength [a] R_m MPa (psi) min	Elongation (on 50 mm or 2 in.) A_f % min	Tensile Strength [b] R_m MPa (psi) min
L175 or A25	175 (25,400)	310 (45,000)	c	310 (45,000)
L175P or A25P	175 (25,400)	310 (45,000)	c	310 (45,000)
L210 or A	210 (30,500)	335 (48,600)	c	335 (48,600)
L245 or B	245 (35,500)	415 (60,200)	c	415 (60,200)
L290 or X42	290 (42,100)	415 (60,200)	c	415 (60,200)
L320 or X46	320 (46,400)	435 (63,100)	c	435 (63,100)
L360 or X52	360 (52,200)	460 (66,700)	c	460 (66,700)
L390 or X56	390 (56,600)	490 (71,100)	c	490 (71,100)
L415 or X60	415 (60,200)	520 (75,400)	c	520 (75,400)
L450 or X65	450 (65,300)	535 (77,600)	c	535 (77,600)
L485 or X70	485 (70,300)	570 (82,700)	c	570 (82,700)

[a] For intermediate grades, the difference between the specified minimum tensile strength and the specified minimum yield strength for the pipe body shall be as given in the table for the next higher grade.

[b] For intermediate grades, the specified minimum tensile strength for the weld seam shall be the same value as was determined for the pipe body using footnote a).

[c] The specified minimum elongation, A_f, expressed in percent and rounded to the nearest percent, shall be as determined using the following equation:

$$A_f = C \frac{A_{xc}^{0.2}}{U^{0.9}}$$

where

C is 1940 for calculations using SI units and 625,000 for calculations using USC units;

A_{xc} is the applicable tensile test piece cross-sectional area, expressed in square millimeters (square inches), as follows:

    1)   for circular cross-section test pieces, 130 mm² (0.20 in.²) for 12.7 mm (0.500 in.) and 8.9 mm (0.350 in.) diameter test pieces; 65 mm² (0.10 in.²) for 6.4 mm (0.250 in.) diameter test pieces;

    2)   for full-section test pieces, the lesser of a) 485 mm² (0.75 in.²) and b) the cross-sectional area of the test piece, derived using the specified outside diameter and the specified wall thickness of the pipe, rounded to the nearest 10 mm² (0.01 in.²);

    3)   for strip test pieces, the lesser of a) 485 mm² (0.75 in.²) and b) the cross-sectional area of the test piece, derived using the specified width of the test piece and the specified wall thickness of the pipe, rounded to the nearest 10 mm² (0.01 in.²);

U is the specified minimum tensile strength, expressed in megapascals (pounds per square inch).

Figure 48: Requirements for the results of tensile tests for API 5L steels for PSL 1 Pipes, taken from API 5L standard [43].